Re/Os cosmochronometer:
measurement of neutron cross sections

Zur Erlangung des akademischen Grades eines
DOKTORS DER NATURWISSENSCHAFTEN
von der Fakultät für Physik der Universität (TH)
Karlsruhe

genehmigte

DISSERTATION

von

Dipl. phys. Marita Mosconi
aus Turin (Italien)

Tag der mündlichen Prüfung: 21.12.2007

Referent:	Prof. Dr. Johannes Blümer, Institut für Experimentelle Kernphysik
Korreferent:	Prof. Dr. Thomas Müller, Institut für Experimentelle Kernphysik

Abstract

This experimental work is devoted to the improved assessment of the Re/Os cosmochronometer. The dating technique is based on the decay of ^{187}Re ($t_{1/2}$=41.2 Gyr) into ^{187}Os and determines the age of the universe by the time of onset of nucleosynthesis. The nucleosynthesis mechanisms, which are responsible for the ^{187}Re/^{187}Os pair, provide the possibility to identify the radiogenic fraction of ^{187}Os exclusively by nuclear physics considerations. Apart from its radiogenic component, ^{187}Os can be synthesized otherwise only by the *s* process, which means that this missing fraction can be reliably determined and subtracted by proper *s*-process modeling. On the other hand, ^{187}Re is almost completely produced by the *r* process. The only information needed for the interpretation as a cosmic clock is the production rate of ^{187}Re as a function of time. The accuracy of the *s*-process calculations that are needed to determine the nucleosynthetic abundance of ^{187}Os depends on the quality of the neutron capture cross sections averaged over the thermal neutron spectrum at the *s*-process sites. Laboratory measurements of these cross sections have to be corrected for the effect of nuclear levels, which can be significantly populated at the high stellar temperatures during the *s* process.

The neutron capture cross sections of ^{186}Os, ^{187}Os and ^{188}Os have been measured at the CERN n_TOF facility in the range between 0.7 eV and 1 MeV. From these data, Maxwellian averaged cross sections have been determined for thermal energies from 5 to 100 keV with an accuracy around 4%, 3%, and 5% for ^{186}Os, ^{187}Os, and ^{188}Os, respectively. Since, the first excited state in ^{187}Os occurs at 9.75 keV, the cross section of this isotope requires a substantial correction for thermal population of low lying nuclear levels. This effect has been evaluated on the basis of resonance data derived in the (n,γ) experiments and by an improved measurements of the inelastic scattering cross section for the first excited level of ^{187}Os. This additional measurement was performed at the 3.7 MV Van de Graaff of Forschungszentrum Karlsruhe using monoenergetic neutron beams from the ^{7}Li$(p,n)^{7}$Be reaction at threshold.

The improved experimental results were used for the evaluation of the true stellar cross section and for the evaluation of the consequences for the Re/Os clock. It is found that the nuclear input is no longer determining the uncertainty of the derived age. First analyses using a simplified schematic model of the galactic chemical evolution yields a cosmic age of 15.6 $\pm$ 1.4 Gyr, but needs to be complemented by a more realistic galactic evolution model.

Re/Os Kosmo-Chronometer: Messung der Neutronenquerschnitte von Osmium

Zusammenfassung

Die vorliegende Arbeit ist der Verbesserung des Re/Os Kosmo- Chronometers gewidmet. Diese Datierungsmethode beruht auf dem Zerfall von ^{187}Re ($t_{1/2}$ = 41,2 Gyr) und ermöglicht eine Altersbestimmung des Universums mit Hilfe der Zeitdauer der Elementsynthese. Der Synthesemechanismus für die Erzeugung der Re/Os Hufigkeiten kann zur Definition des radiogenen Anteils von ^{187}Os auf der Grundlage von kernphysikalischen Überlegungen verwendet werden. Zustzlich zum radiogenen Anteil wird ^{187}Os lediglich im s-Prozess gebildet. Dies bedeutet, dass dieser Anteil mit Hilfe der sehr zuverlssigen Modelle für den s-Prozess genau bestimmt werden kann. Andererseits wird ^{187}Re praktisch vollstndig im r-Prozess erzeugt. In diesem Zusammenhang stellt die Zeitabhngigkeit der Produktionsrate von ^{187}Re die einzige relevante Information dar. Die Genauigkeit der notwendigen s-Prozessrechnungen zur Festlegung des s-Anteils der ^{187}Os Häufigkeit hngt entscheidend von der Qualität der stellaren Neutroneneinfangquerschnitte der Os Isotope ab. Die experimentell gemessenen Querschnitte müssen jedoch bezüglich der stellaren Situation korrigiert werden, die durch die thermische Besetzung von Kernzustnden bei hohen Temperaturen bewirkt wird. Die Einfangquerschnitte von ^{186}Os, ^{187}Os und ^{188}Os wurden an der n_TOF Anlage am CERN im Energiebereich von 0.7 eV bis 1 MeV gemessen. Aus diesen Ergebnissen wurden Maxwell-Mittelwerte für thermische Energien von 5 bis 100 keV mit Genauigkeiten von 4, 3 und 5% für ^{186}Os, ^{187}Os und ^{188}Os ermittelt. Da der erste angeregte Zustand von ^{187}Os bei 9,75 keV liegt, erfordert der Querschnitt dieses Isotops wegen der starken thermischen Anregung eine signifikante Korrektur. Diese Korrektur wurde auf der Grundlage der aus den gemessenen Daten ermittelten Resonanzparameter und einer verbesserten Messung des inelastischen Querschnitts für den ersten angeregten Zustand von ^{187}Os bestimmt. Dieses zustzliche Experiment wurde am 3,7 MV Van de Graaff Beschleunigers des Forschungszentrums Karlsruhe durchgeführt, wobei monoenergetische Neutronen an der Schwelle der ^{7}Li(p, n)^{7}Be Reaktion erzeugt wurden.

Mit Hilfe der verbesserten experimentellen Ergebnisse konnten die wahren stellaren Querschnitte definiert und die entsprechenden Konsequenzen für die Re/Os-Uhr ausgearbeitet werden. Es zeigte sich, dass die Unsicherheit des abgeleiteten Alters nicht lnger durch die kernphysikalischen Aspekte dominiert wird. Erste Analysen mit einem einfachen schematischen Modell für die chemische Entwicklung des Universums führen auf ein Alter von 15,5 $\pm$ 1,4 Gyr. Dieses Ergebnis muss mit Hilfe realistischer Modelle erhrtet werden.

Contents

List of Tables

List of Figures

Part I

Nucleosynthesis and chronometry

Chapter 1

Introduction

The possibility to use the law of radioactive decay for dating purposes has been applied already since its discovery: Rutherford obtained the age of solidification of some rocks containing uranium in 1907 [1] and published an estimate for the age of the Earth in 1929 [2]. Nowadays, the age of the solar system, t_{ss}=4.559 ± 0.004 Gyr, is precisely assessed by nuclear dating [3, 4]. Whenever a system is not open to further contaminations and the initial conditions are known (for example, in Rutherford' s application, helium, the daughter of the uranium decay, was not included in the rocks during the solidification process) the age determination is straight forward.

1.1 Dating the cosmos via radioactivity

The quest for the age of the universe is hampered by the fact that the cosmos is not a closed system. The nuclear species were not synthesized at once and at the same time, but the observable isotopic abundances are the result of a complex history of syntheses (from the Big Bang to the diverse processes in stars), remixing and diffusion in the interstellar medium, further modification in later generations of stars until this mix condensed into the solar system. Except for a few specific cases, it is therefore extremely difficult to reconstruct the creation and decay history of a mother/daughter relation.

The most promising among the nuclear cosmic clocks are the pairs ^{238}U/^{232}Th and ^{187}Re/^{187}Os, which are affected by different systematic uncertainties. For the first pair, it is possible to avoid the complication of chemical evolution, but the involved nucleosynthesis mechanisms must be fully understood, while for the second the formation processes can be accurately described, but the dependence of the ^{187}Re production with time has to be obtained by modeling the chemical evolution of the Galaxy.

Uranium (^{238}U, half-life $t_{1/2}$ = 4.468 Gyr) and thorium (^{232}Th, $t_{1/2}$ = 14.05 Gyr) can be observed directly in the atmosphere of very old stars, which formed so early in the galactic history that they do not show other

heavy elements than those produced by supernova explosions of first generation stars. Extremely metal poor stars are found in the Galactic halo and their spectroscopic features are so faint that their surface composition could be analyzed only during the last decade [5]. These stars have obviously seen only one nucleosynthesis event related to the rapid neutron capture process (r process, see section 2.2.2). Ever since, the surface abundance was never changed, so that these stars can be considered as a closed system. In order to use the presently observed U/Th abundances for determining the age, the original r-process production of these elements must be inferred by astrophysical models. This part of the analysis is strongly model dependent and correspondingly uncertain [6, 7]. The current estimate by this approach yields a Galactic age of $\mathbf{14.1 \pm 2.5\ Gyr}$ [6]. This value was challenged by the recent discovery of a metal poor star strongly enriched in r-process elements, which allowed to compare the r-process predictions for the U/Eu, U/Os, U/Ir, U/Th, Th/Eu, Th/Os, and Th/Ir pairs with the abundances measured in this star [5]. The range of production ratios obtained in previous r-process models [6, 8, 9, 10, 11, 12] yields a lower average age of $\mathbf{13.2 \pm 2.7\ Gyr}$, where astronomical observation and the parameterization of the stellar atmosphere contribute 1.5 Gyr to the quoted uncertainty. If the analysis is restricted to the U/Eu, U/Os, U/Ir, and U/Th pairs this uncertainty reduces to 0.9 Gyr and the final average age becomes $\mathbf{13.4 \pm 1.8\ Gyr}$.

A different approach to this cosmochronometer has been proposed recently by combining the astronomical observations of uranium and thorium in low metallicity stars and their abundances in carbonaceous chondrites (CC) [12]. These data have been used to constrain the primordial U/Th production ratio and the age of the Galaxy. A Galactic chemical evolution model was invoked to infer from the metallicity of G-dwarfs [13] the CC U/Th ratio. Combined with the U/Th ratio observed in low metallicity stars, this approach yields an age of $\mathbf{14.5^{+2.8}_{-2.2}\ Gyr}$ [12].

The Re/Os pair requires a different approach: Since ^{187}Re ($t_{1/2}$= 41.2 Gyr [14]) and ^{187}Os are not the only isotopes of these elements, their abundances can not be determined by astronomical observation as this technique is only sensitive to elemental abundances. Therefore, the solar system ratio of ^{187}Os/^{187}Re has to be used for this clock. On the other hand, knowledge of the effective r-process yield of ^{187}Re is not necessary, because the decay of ^{187}Re can be obtained by the radiogenic fraction of ^{187}Os. Accordingly, the history of the r-process production of ^{187}Re represents the main difficulty in this case, which needs to apply a model of Galactic chemical evolution (GCE). The radiogenic fraction of ^{187}Os can be obtained by subtraction of the s-process component from the solar abundance. The s-process part can be accurately obtained by systematics provided that the neutron capture cross sections are precisely known (see section 2.2.1) [15, 16, 17]. A recent estimate for the age of the universe with this methods yields $\mathbf{15 \pm 2}$ Gyr

[18]. This value includes the time between the Big Bang and the formation of the galaxies, which is presently estimated to be smaller than 750 Myr [19].

1.2 Other techniques

The age of the universe can be obtained also by means of different dating techniques. The astronomical and cosmological approaches are extracting the age by fitting particular observables with theoretical models.

1.2.1 Astronomical dating

It is possible to constrain the Galactic age by the astronomical observation of the evolution of globular clusters. These are stellar populations consisting of stars of the same age, which were formed very early in the Galaxy. Since then they evolve together with a life cycle that depends only on stellar mass. In the Hertzsprung-Russell diagram (plot of the surface temperature of stars versus luminosity) these stars populate the main sequence up to a certain point, when the heavier stars evolve off the main sequence because they are becoming red giants. Thus, their Hertzsprung-Russell diagram shows the stadium of evolution of stars of different mass, which are born at the same time. The cooling sequence of the white dwarfs [20] and the turn-off point [21] can be used for dating the clusters. Both techniques are based on best fits of the Hertzsprung-Russell diagram in the white dwarf region or at the link between the main sequence and the red giant branch. Reliable astronomical distances and accurate observations (long exposure times are needed especially for white drafts) are required. Additionally, the theoretical description of the cluster isochrone function demands reliable inputs for the nuclear reactions involved in H-burning, and the description of the cooling sequence of the white dwarfs requires their composition and the size of their carbon-oxygen core. From these studies a lower limit for the age of the universe is obtained because the formation time of globular clusters is somewhat uncertain. Current analyses of the turn-off point yield a lower limit of $\geq$ **11.2 Gyr**[21], while the white dwarf cooling sequence yields $\geq$ **12.1 Gyr** [20].

1.2.2 Cosmological dating

In this approach, the age is obtained via the observed expansion of the cosmos. The age based on the Hubble constant is an example of this type. Beside the measurement of the redshift of distant stars [22], the anisotropy of the cosmic microwave background (CMB) [23] has also been used for this purpose. The improved Hubble constant determined by the Hubble Space

Telescope project, which used mainly Cepheid observations for distance calibrations, yields an age of the universe of **13 ± 1 Gyr** [22] considering a flat universe with 70% dark energy and 30% matter. This value has been updated to **13.6 ± 1.5 Gyr** by a different group [24].

The WMAP experiment measured the anisotropies of the CMB and plotted them into a temperature angular power spectrum [25]. The slight temperature differences in the CMB between neighbouring sky zones [23] (of the order of 10^{-5} K) are the signature of acoustic oscillations of the photon-baryon fluid at the age of decoupling between matter and radiation. Under the assumption of a flat universe, the age of the cosmos can be expressed by the position of the first acoustic peak as a function of the matter density [26, 27] and of the Hubble constant. The age estimated in this way is **13.7 ± 0.2 Gyr** [23, 27]. Recently, the sensitivity of the result to deviations from the standard cosmological model, in particular to changes in the relativistic energy density and consequently in the cold dark matter density [28] leads to the conclusion that the systematic uncertainty could be larger by an order of magnitude. It has been shown that if the relativistic energy density is left as a free parameter the age of the universe becomes $\mathbf{13.8^{+2.3}_{-3.2}}$ **Gyr** [28]. Constraining the relativistic energy density by the Hubble constant, reduces the estimated the age of the universe slightly to $\mathbf{13.1^{+0.96}_{-0.87}}$ **Gyr** [28].

1.3 Need of additional data

All the different dating techniques for the age of the universe are using some theoretical parameterization that can affect the results. Up to approximately a decade ago, the different techniques for dating the cosmos were in severe disagreement, and changes in the input data were leading to differences much larger than the claimed uncertainties. The situation is considerably improved. In particular, the agreement between different methods is an essential progress for obtaining a reliable age of the universe. In this perspective, the solution of the persisting ambiguity in the Re/Os cosmochronometer is an important aspect for completing the picture.

Chapter 2

The Re/Os cosmochronometer

D. D. Clayton was the first to propose the β-decay of ^{187}Re to ^{187}Os for dating the universe [29]. The nucleosynthesis concept behind this chronometric pair is sketched in figure 2.1. The mother ^{187}Re is shielding the daughter ^{187}Os from contributions by the r process. Consequently, ^{187}Os is synthesized only by s process (apart from the radiogenic production). Since the s-process yields in this mass region can be very well determined by the stellar neutron capture cross sections, the radiogenic component of ^{187}Os can be defined by subtraction of the s-process component from the solar abundance [30, 31, 32], thus yielding the mother/daughter ratio independently of the initial r-process yields. However, in this case the production of ^{187}Re over the period of Galactic history has to be considered. Hence the Re/Os clock complements the U/Th cosmochronometer. This aspect is outlined in the following overview of the relevant nucleosynthetic processes and of the characteristics of the Re/Os cosmochronometer.

2.1 Nucleosynthesis by fusion reactions

Shortly after the Big Bang the universe consisted of hydrogen and helium, except for some small amounts of lithium, due to the instability gaps A= 5 and 8. All other nuclear species were created later in stars by nuclear reactions (apart of the minor elements lithium, beryllium and boron formed by cosmic ray spallation) during the history of the universe. The increasing nuclear binding energy from hydrogen to iron provides the efficient energy source of stars, which is used in different evolutionary stages, starting from hydrogen burning at relatively moderate temperatures. Depending on the initial mass, stars between 0.013 solar masses ($M_\odot$) and 0.08 $M_\odot$ are developing core temperatures of a few Million K, where only protons and deuterons can merge into ^{3}He (brown dwarfs). From masses larger than 0.08 $M_\odot$ on,

the fusion of protons into helium can start at temperature of 8 Million K [33] in the so called proton-proton chain. This is the first H burning process that can ignite in a star, and the only H burning process possible with the ashes of the Big Bang. In second generation stars hydrogen burning can be operating via the CNO cycle, where carbon, nitrogen and oxygen isotopes act as catalysts to form helium in the $^{15}\mathrm{N}(p,\alpha)^{12}\mathrm{C}$ reaction after a series of proton capture reactions. The CNO cycle requires somewhat higher temperatures because of the higher Coulomb barriers of the involved reactions, and is therefore only dominant in stars heavier than 1.5 $\mathrm{M}_{\odot}$.

As long as the energy produced by hydrogen burning balances the gravitational contraction, the star evolves in hydrostatic equilibrium. After the hydrogen is consumed, the core contracts and heats up until helium fusion to carbon and oxygen is ignited. Depending on the initial stellar mass, further fusions reactions can be ignited at increasingly higher temperatures.

The time a star can spend in a particular burning phase is a function of mass. Temperature and density in the core are growing with stellar mass, giving rise to increasing reaction rates, which lead to faster fuel exhaustion. The evolutionary sequence starting with core H burning leads to hydrogen burning in a shell around the exhausted core. If the stellar mass exceeds 0.4 $\mathrm{M}_{\odot}$, core temperatures around 100-200 Millions K are reached by gravitational contraction, sufficient for helium burning to start. Otherwise, the star will be stabilized by electron degeneracy, ending as a He white dwarf. When also He is exhausted in the core, the star will contract again, and energy production is shifted into shells of H and He. Due to the higher temperature in the core the envelope is expanding dramatically, leading to very strong stellar winds so that the entire envelope can be lost. This mechanism is remixing freshly synthesized material into the interstellar medium, thus contributing to the chemical evolution of the Galaxy. If the stellar mass is large enough, other fusion reactions can be triggered during this period, i.e. silicon is produced after C, O, and Ne burning episodes. At this point, the Coulomb barrier for the fusion of ^{28}Si is so high and the temperature rises to such high values that ^{28}Si is partially destroyed by photodisintegration and the nuclei up to ^{56}Fe are synthesized by reactions between ^{28}Si and the protons and α particles generated by the photodisintegration. All these advanced burning stages are exothermic and create an equilibrium between the radiation pressure and the gravitational energy that contracts the star. After this stage no further possibilities for energy generation are left to withstand the gravitational contraction of the core. If the core mass exceeds the Chandrasekhar limit of $\mathrm{M} \lesssim 1.44\ \mathrm{M}_{\odot}$, the star will explode as a supernova with a neutron star or a black hole as the remnant. Supernovae are returning the entire envelope to the interstellar medium and are also considered to be the most promising r-process sites (section 2.2.2).

2.2 Nucleosynthesis beyond iron

Nuclei heavier than iron can not be produced by exothermic reactions of charged particles because of the decreasing nuclear binding. These species have to be generated in different scenarios and with different mechanisms. In fact the nuclei beyond iron are produced by a sequence of neutron capture reactions and subsequent β-decays [34]. If the neutron flux is weak, unstable nuclei can decay before they have the possibility to capture another neutron, and neutron capture chain follows the valley of β-stability. This slow neutron capture process (or s process for short) contributes to the abundance of the most stable nuclei and ends at ^{209}Bi. Further neutron capture reactions are leading to the α-unstable isotopes ^{210}Bi, ^{211}Bi and ^{210}Po, which decay back into ^{206}Pb and ^{207}Pb.

The existence of uranium and thorium invokes a second neutron capture process with sufficiently high neutron density to override the short lived α-emitters between bismuth and the actinides. This rapid (r) process is also required to explain the origin of neutron rich isotopes that can not be reached by the s process because of very short lived β-unstable neighbours. Because of the very intense neutron flux, the r-process path is located about 10 - 20 mass units away from the stability valley, close to the neutron drip line. After the r process, the unstable products decay to the stability valley [35]. The s and the r process contribute about equal amounts of the observed abundances between iron and bismuth. A few proton rich nuclei with very low abundances can not be synthesized neither by the s nor by the r process. These nuclei are produced in the so called p process, most likely the result of (γ, n), (γ, p), and (γ, α) reactions at very high temperatures [36].

2.2.1 *s* process

The principal mechanisms and sites of the s process are well understood. The observation of the absorption lines of the unstable element technetium ($t_{1/2}$=4.2 10^6 yr) in the atmosphere of red giants in 1952 [37] provided the first clear evidence that the s process occurs during the He burning stage of stellar evolution. Further astronomical observations have confirmed the s process in low mass ($1\ M_\odot \leq M \leq 3\ M_\odot$) asymptotic giant branch (AGB) stars, and evolutionary models are currently reproducing the isotopic abundances from Zr to Bi (the so called main s-process component) [38]. The structure of these stars exhibit an inert C/O core surrounded by a He shell and a fully convective envelope. Energy is produced by hydrogen burning at the bottom of the envelope until the He shell reaches the critical temperature to ignite He burning. The high temperature dependence of the He-burning reactions leads to a He shell flash, which quickly consumes the helium in the shell. At this point quiescent hydrogen burning takes over again until the He shell is replenished for the next shell flash. During the AGB phase

about 20 -30 such flashes can take place.

This scenario is characterized by two neutron sources. During He-burning, the temperatures are high enough that the ^{22}Ne$(\alpha, n)^{25}$Mg reaction is partially activated. The dominant neutron exposure is provided, however, by the ^{13}C$(\alpha, n)^{16}$O reaction, which takes place during H-burning. The ^{13}C is produced by proton capture on ^{12}C at the border of the He shell and the envelope.

The two sources in AGB stars are characterized by different temperatures, neutron densities, and total exposures. The ^{22}Ne$(\alpha, n)^{25}$Mg reaction in the He shell flashes works at 2.5 10^8 K (kT= 23 keV), the peak neutron density reaches 10^{10} cm^{-3} and contributes about 5% to the total neutron exposure. The ^{13}C$(\alpha, n)^{16}$O reaction during H burning operates at 9 10^7 K (kT= 8 keV), the neutron density is 10^7 cm^{-3}, and the contribution to the total neutron exposure is 95%.

The nuclei from Fe to Zr originate from massive stars (M $\geq$ 8 M$_\odot$), either from core He-burning or shell C burning (weak s-process component) [39, 40]. The only neutron source in massive stars is the ^{22}Ne$(\alpha, n)^{25}$Mg reaction.

Already before stellar models had been worked out in detail, the s-process mechanism was sketched empirically, thus allowing to describe the s-process abundances [41, 42]. This approach (referred to as the "classical s process") uses the hypothesis of a low neutron density to simplify the differential equations of production and destruction of isotope A by a chain of neutron capture reactions:

$$\frac{dN_A(t)}{dt} = n_n(t)N_{(A-1)}(t) < \sigma v >_{(A-1)} - n_n(t)N_A(t) < \sigma v >_A - \lambda_\beta(t)N_A(t) \tag{2.1}$$

where $N_{(A-1)}(t)$ is the abundance as a function of time of the precursor nuclide, $< \sigma v >$ is the Maxwellian averaged capture cross section (MACS) obtained by folding the energy dependent capture neutron cross section with the thermal velocity distribution of the neutrons, λ_β is the β-decay constant for nucleus A, and $n_n(t)$ is the neutron density.

In the calculations of a MACS it is not sufficient to use the experimentally measured cross sections, because the high temperatures at the s-process site imply that low lying excited states can be populated by the intense, energetic thermal photon bath. Neutron capture on these excited states requires a correction for the stellar enhancement factor (SEF), which has to be evaluated theoretically (see section 2.4). By the assumption that β-decay is much faster than neutron capture and by defining the MACS as

$$\sigma_A = \frac{< \sigma v >_A}{v_T} = \frac{\int \sigma(E)\Phi(E)dE}{\int \Phi(E)dE}, \tag{2.2}$$

where $\Phi(E)$ is the neutron flux and v_T the thermal velocity, equation 2.1

can be simplified

$$\frac{dN_A(t)}{dt} = v_T n_n(t)(\sigma_{A-1}N_{A-1} - \sigma_A N_A) \tag{2.3}$$

Replacing the neutron flux, $v_T n_n(t)$, by the exposure $\tau = v_T \int_0^t n_n(t)dt$ and assuming constant temperature, one obtains

$$\frac{dN_A}{d\tau} = \sigma_{A-1}N_{A-1} - \sigma_A N_A. \tag{2.4}$$

If flow equilibrium in the reaction chain is reached, one gets the expression

$$\sigma_{A-1}N_{A-1} = \sigma_A N_A = \text{constant}, \tag{2.5}$$

which is called *local approximation*. It holds between neighbouring nuclei, provided that these neutron capture cross sections are sufficiently large. Exception from this rule are nuclei with neutron magic numbers. They exhibit very small neutron capture cross sections and act as bottle necks in the reaction flow, causing the discontinuities in the plot of the product $\sigma_A N_A$ versus A [43]. In the main region of the main component, between Zr and Bi, this product can be fitted reasonably well by the classical approach. However, this approximation fails in describing the branchings in the reaction flow that occur at unstable isotopes with sufficiently long half-lives where neutron capture can compete with β-decay. It fails also in reproducing the s-abundances from Fe to Zr, which are mainly produced by the weak s process.

With respect to the Re/Os clock, the local approximation is valid because of the large (n, γ) cross sections in this mass region.

2.2.2 *r* process

The r-process site is still under debate, the most probable scenario being supernova (SN II) explosions [35]. Also neutron star mergers are discussed as a possible alternative [44, 45]. The mechanism of the neutron source is probably related to the intense neutrino winds from the core collapse, which are considered to heat the material of the shock front above and to produce an enormous density of free nucleons. The physical conditions (temperatures, density, neutron exposures), in which the r process acts, are extremely difficult to define by theory and are presently constrained by the r-abundance pattern, which is obtained by subtraction of the s-abundances from the solar distribution [46]. Also the nuclear physics data involved, and in particular the half-lives of the nuclei in the actual r-process region, are uncertain because they have to be obtained by theory, and only very few experimental information is available for the very neutron rich isotopes far from stability. Due to the high temperature and neutron density conditions,

current r-process simulations are considering that the neutron capture path is close to the neutron drip line and that the abundances are determined by the waiting point concept. At the end of an isotopic chain the equilibrium condition between neutron capture and (γ, n) reactions is described by the Saha equation for the reactions rates $\lambda_{\gamma n}$ and $\lambda_{n\gamma}$:

$$\frac{\lambda_{\gamma n}}{\lambda_{n\gamma}} \propto \frac{T^{\frac{3}{2}}}{n_n} exp\left(-\frac{Q_n}{kT}\right) \tag{2.6}$$

where n_n is the neutron density and Q_n is the neutron separation energy. This relation defines the location of the r-process path in the chart of nuclides once the nuclear masses are determined. The β-half life of these r-process nuclei determine, how long the reaction flow has to wait before β-decay drives it to higher atomic numbers. During this waiting time the abundance accumulates to the final r-abundances.

2.3 Nucleosynthesis in the Re/Os region

The s-process path in the mass region around A=187 is shown in figure 2.1. The isotopes ^{186}Os and ^{187}Os are shielded from the r process by their

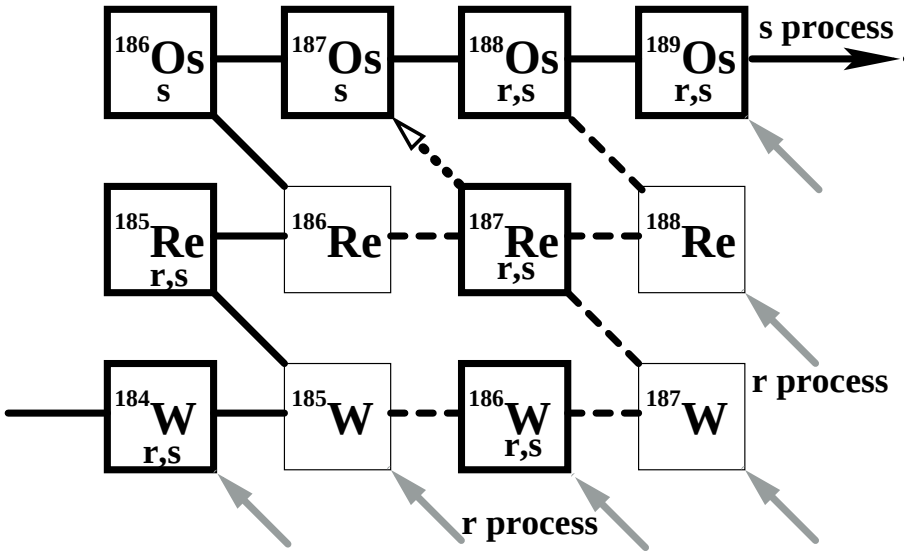

Figure 2.1: The s-process reaction flow (black line) and r-process paths (gray arrows) in the mass region around $A = 187$. The weak s-process branchings at ^{185}W and ^{186}Re are indicated by dashed lines. Stable or long lived nuclei are plotted as bold boxes. The ^{187}Re β-decay is marked by a dotted arrow.

stable isobars ^{186}W and ^{187}Re and are, therefore, synthesized only by the s process, except for the radiogenic contribution from ^{187}Re. All possible

s-process branchings (dashed lines in figure 2.1) have been investigated previously [47]. The branching at ^{185}W was analysed on the basis of a new evaluation of the $^{185}\mathrm{W}(n,\gamma)$ cross section obtained by the measurement of the inverse reaction at S-DALINAC [48]. The effect of this branching as well as that at ^{186}Re [49] on the clock was found to be negligible.

2.4 The neutron capture rate of ^{187}Os

The MACS of ^{187}Os is sensitive to the population of nuclear levels by the hot thermal photon bath, because of the low excitation energy of its low-lying states. In fact, the first excited level lies at 9.75 keV and the next two around 75 keV. For a thermal energy of 30 keV, the first excited level is populated by 47% while the ground state is only populated to 33% [50]. Correspondingly, a significant SEF is to be expected and must be determined by consistent calculations of the neutron capture cross sections for the excited states. The SEF is simply defined by the relation

$$\langle\sigma\rangle^{\star} = \mathrm{SEF}\cdot\langle\sigma\rangle^{lab},$$

where $\star$ and lab indicate the MACS determined under stellar and under laboratory conditions, respectively. The stellar MACS needs to be determined by calculating the capture cross sections from the ground state as well as from excited target states, weighted by their respective thermal population probability given by

$$p_x = \frac{(2I^x+1)e^{-\frac{E_x(I^x)}{kT}}}{\sum_x (2I^x+1)e^{-\frac{-E_x(I^x)}{kT}}} \tag{2.7}$$

where $E_x(I^x)$ is the excitation energy of the target state with total angular momentum I^x. The neutron capture cross section, performed on the basis of the Hauser-Feshbach statistical model [51], can be written as

$$\sigma_{n,\gamma}(E_n) = \frac{\pi\lambda\!\!\!^{-2}_n}{2(2I^x+1)}\sum_{J,\pi}(2J+1)\frac{T^x_n(J^\pi)T_\gamma(J^\pi)}{\sum_{m,\nu}T^\nu_m(J^\pi)}W_\gamma(J^\pi) \tag{2.8}$$

where

$\pi\lambda\!\!\!^{-2}_n$ is the geometrical cross section according to quantum mechanics with $\lambda\!\!\!^{-}_n$ the neutron wavelength divided by 2π,

I^x the total angular momentum of the target state x,

J^π the spin of the compound nucleus excited to a level of parity π,

T_n^x the transmission function for the compound nuclear state to be formed by the excited level plus a neutron, defined as the ratio between the averaged neutron width and the averaged level spacings,

T_γ the total photon transmission function (considers all permitted gamma-transitions to lower lying states in the compound nucleus), also obtained as the ratio between the averaged gamma widths and the averaged level spacings $T_\gamma = \frac{<\Gamma_\gamma>}{<D_l>}$,

$\sum_{m,\nu} T_m^\nu(J^\pi)$ the sum over all transmission functions for all possible decays (for ^{187}Os only T_n and T_γ are to be considered so m={n, γ}) starting from all permitted levels in ^{188}Os (index ν),

$W_\gamma(J^\pi)$ is the width fluctuation correction factor which takes into account the different statistical fluctuation properties of the neutron and γ reaction channels [52].

The first four quantities defined above refer to the formation of the compound nucleus, while the following two describe the probability that the compound system decays into the radiative channel. Measurements of the averaged widths and level spacings by resonance analyses can assess the transmission functions for the capture on the ground state. The other transmission functions are evaluated from an optical nuclear potential. The parameters of this potential can be constrained by experimental information on elastic and inelastic cross sections. The inelastic cross section for the first excited level can also be used to parameterize the so-called super-(in)elastic scattering channel, where neutrons scatter on excited states and gain in energy by de-excitation of the nucleus to a lower level.

2.5 ^{187}Re abundance and half life

The ^{187}Re half life and its temperature dependence represents a key quantity of the Re/Os clock. The half life for an atom of ^{187}Re has been measured to be 41.2 ± 0.2(stat) ± 1.1(syst) Gyr [14], while the half-life of a completely bare nucleus has been measured as 33 ± 2 yr [53]. The dramatic acceleration of the decay of bare nuclei is due to bound β-decay, where electrons are emitted into unoccupied atomic orbits. While the Q value for β-decay of a neutral ^{187}Re atom is 2.66 keV, it is increased by the electron binding energy in a bare nucleus. Hence, the Q-value for an electron captured in the K shell of an ^{187}Os atom is 72.97 keV.

The accelerated decay at high temperatures has the consequence that ^{187}Re can be destroyed in later stellar generations. This “astration” effect has been investigated with respect to the Re/Os clock and was found to result in a comparably small correction [54].

Ultimately, this effect should be studied in the framework of a full model for the Galactic chemical evolution (GCE), that should also be invoked to describe the formation of ^{187}Re as a function of time until the solidification of the solar system.

Up to now the production of the ^{187}Re with time was described in most cases by the assumption that the supernova rate decreased exponentially from the first generation stars. Extreme models like a sudden or uniform creation are included in this picture as the limits of a very small or very large parameter in the exponent. Other approaches are based on astronomical observations of the metallicity of white dwarfs [13] or of the metallicity of stars with emphasis on their r-process abundances [55]. From meteoritic observations one may infer that an r-process event could have occurred just before the solar system formed. In this case, the solar abundances are dominated by the sudden contribution and the astration corrections become less important. A plausible model has been suggested by Fowler to combine an exponential model with a sudden contribution at times near the solar system formation [43].

2.6 Required input for the Re/Os clock

In summary, the quantities and models that needed are for an evaluation of the Re/Os clock are:

1. The solar abundances of ^{186}Os, ^{187}Os, and ^{187}Re.

2. The neutron capture cross sections of ^{186}Os and ^{187}Os from 100 eV to 300 keV to calculate the MACS from laboratory measurements.

3. The resonance parameters for improved the Hauser Feshbach calculations of the SEF.

4. The inelastic scattering cross section for the first excited level to obtain the transmission coefficients for all competing inelastic scattering channels.

5. The calculation of the SEF correction at the s-process temperatures.

6. A model of GCE including the astration effects to take proper account of the decay of ^{187}Re before the condensation of the solar system.

The solar abundances of rhenium and osmium were measured in carbonaceous chondrites with an uncertainty of 11% [31]. Recently, new data have been extracted from a set of iron meteorites with an improved uncertainty of 3% [32].

The SEF-corrected MACS are used to obtain the radiogenic fraction of ^{187}Os by means of the s abundance via the local approximation.

$$N^{rad}_{^{187}\mathrm{Os}} = N^{\odot}_{^{187}\mathrm{Os}} - N^{s}_{^{187}\mathrm{Os}} = N^{\odot}_{^{187}\mathrm{Os}} - \frac{\sigma^{\star}(^{186}\mathrm{Os})}{\sigma^{\star}(^{187}\mathrm{Os})} N^{s}_{^{186}\mathrm{Os}}. \tag{2.9}$$

In terms of the abundance ratios, this can be written as

$$\frac{N^{rad}_{^{187}\mathrm{Os}}}{N^{\odot}_{^{187}\mathrm{Re}}} = \frac{\dfrac{N^{\odot}_{^{187}\mathrm{Os}}}{N^{\odot}\mathrm{Os}} - \dfrac{\sigma^{\star}(^{186}\mathrm{Os})}{\sigma^{\star}(^{187}\mathrm{Os})} \dfrac{N^{\odot}_{^{186}\mathrm{Os}}}{N^{\odot}_{\mathrm{Os}}}}{\dfrac{N^{\odot}_{^{187}\mathrm{Re}}}{N^{\odot}_{\mathrm{Re}}}} \dfrac{N^{\odot}_{\mathrm{Os}}}{N^{\odot}_{\mathrm{Re}}}. \tag{2.10}$$

If one assumes the simplest case, i.e. an exponential decrease of the supernova rate without any astration, the time t_0 between the onset of r-process nucleosynthesis and the formation of the solar system can be constrained by the mother/daughter ratio

$$\frac{N^{rad}_{^{187}\mathrm{Os}}}{N^{\odot}_{^{187}\mathrm{Re}}} = \frac{\Lambda - \lambda_{187}}{\Lambda} \frac{1 - e^{-\Lambda t_0}}{e^{-\lambda_{187} t_0} - e^{-\Lambda t_0}} - 1, \tag{2.11}$$

where λ_{187} denotes the decay constant of ^{187}Re (0.0164 Gyr^{-1}) and Λ the time constant of the supernova rate (for instance, $\Lambda = (0.43t)^{-1}$ Gyr^{-1} is the exponential rate of the "Fowler model"). In figure 2.2 the ^{187}Os

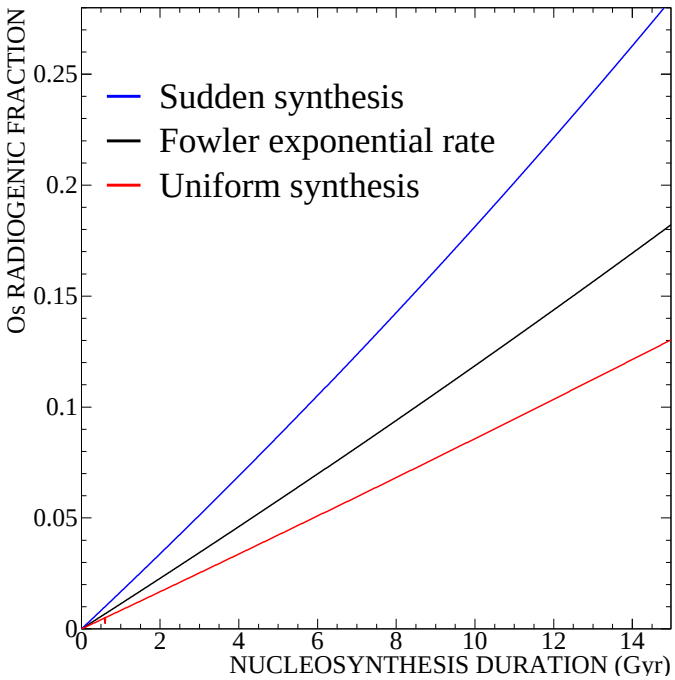

Figure 2.2: ^{187}Os radiogenic fraction as a function of time for three different schematic GCE models.

radiogenic fraction $\frac{N^{rad}_{^{187}\mathrm{Os}}}{N^{\odot}_{^{187}\mathrm{Re}}}$ is plotted as function of time according to the Fowler model and the extreme cases of only one nucleosynthetic event at t=0 (sudden nucleosynthesis) and an uniform ^{187}Re formation. After the formation of the solar system, there is only free decay of ^{187}Re. The age of the universe can then be obtained by the sum of t_0, the age of the solar system, and the time from the Big Bang until the formation of the first generation of stars. The value of the age of the solar system is precisely measured by radioactive dating of meteorites [3, 4] as 4.559 ± 0.004 Gyr while the formation of the Galaxy occurred less than 1 Gyr after the Big Bang. This is confirmed by the deep space survey [19], where galaxies would be observed at times of 1 Gyr after the the Big Bang [19].

2.7 Previous works and the n_TOF proposal

Measurements of the neutron capture cross sections of ^{186}Os and ^{187}Os were performed twice [15, 16] and also the inelastic cross section was repeatedly measured [17, 56, 57, 58]. Improved neutron cross sections are of vital importance because of gaps in the existing information and discrepancies between previous results.

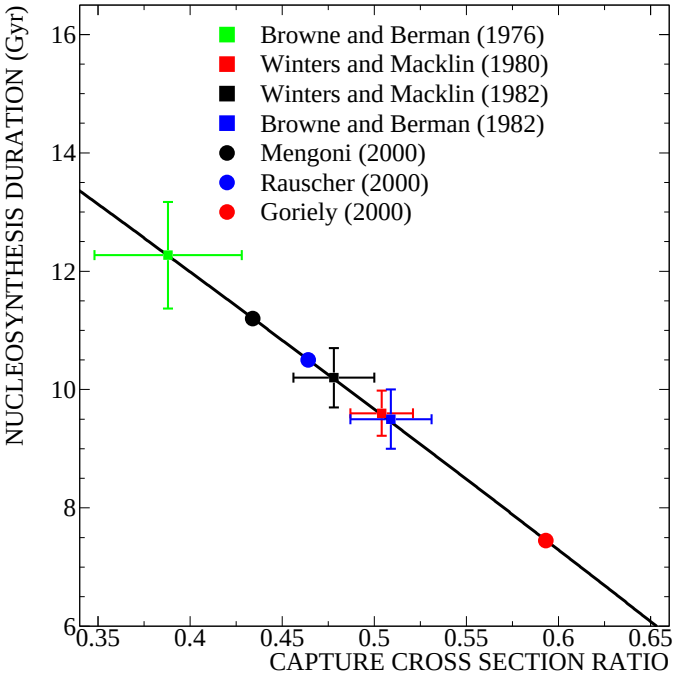

Figure 2.3: Duration of nucleosynthesis deduced from the stellar neutron capture cross sections of ^{186}Os and ^{187}Os reported by different authors. Experimental results are plotted as squares with errors bars. Note that the original publication [59], [60] have been later corrected in [15], [16].

The corresponding uncertainty in the Galactic age due to the nuclear input alone is 2.3 Gyr [61, 62], for the schematic exponential model, too large to compete with other age determinations. The discrepancies obtained

are illustrated by the various results plotted in figure 2.3.

Since theoretical cross sections [63, 64, 65] are also in large disagreement (see figure 2.3), an improved experimental determination of the parameters used in the model calculations is essential for a reliable interpretation of the Re/Os clock.

In view of this demand, the n_TOF collaboration proposed to measure the neutron capture cross sections of ^{186}Os and ^{187}Os at the CERN n_TOF facility in the energy range from 0.7 eV to 1 MeV. In this way, the MACS from a few keV to 100 keV can be calculated with an expected uncertainty of a few percent. Moreover, the high resolution in neutron energy could be used to resolve individual neutron resonances and to perform an improved analysis of the radiative widths and level densities. Those data are essential for improving the theoretical determination of the SEFs. With the same aim, an additional measurement of the inelastic scattering cross section was scheduled at the 3.7 MV Van de Graaff of Forschungszentrum Karlsruhe.

Part II

Radiative neutron capture measurements

Chapter 3

Experimental techniques

The neutron-nucleus interactions at energies below the pion production threshold can be classified in direct or compound nucleus reactions. A direct reaction is taking place when the colliding particle interacts only with few nucleons and the time scale of the process is comparable to the time the projectile spends to cross the nucleus. Instead, a compound nucleus reaction requires that the particle is absorbed, creating a collective system of all the nucleons of the target nucleus. The interactions of neutrons with energies below a few MeV are easily forming compound systems. The excitation energy available for the system is equal to the addition of the kinetic energy plus the neutron separation energy of the compound nucleus (equivalent to the Q value of the reaction). The neutron separation energies (S_n) are typically from 5-8 MeV for heavy nuclei and 10 MeV or more for light nuclei [66].

The compound system can de-excite in different ways according to its mass and energy by γ-rays or particle emission and by fission. The radiative neutron cross section measures the probability of de-excitation by γ-ray emission. The elastic scattering channel is usually dominating and also the inelastic scattering channels (that are open when the kinetic energy of the system exceeds the energy of the first excited level of the nucleus) have a much larger cross section than radiative capture. The de-excitation of the compound nucleus via pure γ-ray emission has usually a variety of allowed possible γ-ray cascades, every one characterized by a different energy distribution and multiplicity (see also figure 3.1). The energy of the γ-rays can vary from few keV to the whole energy of the cascade, if the transition occurs directly to the ground state. Usually, the most common energy for a single photon from a de-excitation cascade is 1-2 MeV.

Neutron capture cross sections can be measured by two different techniques: activation or Time-of-Flight (TOF). The first method can be applied only to reactions producing an unstable nucleus. The generated radioactivity can then be used to derive the cross section. The sample under analysis

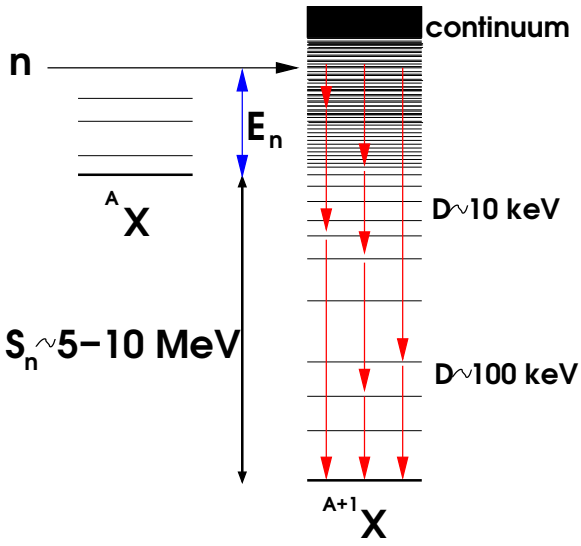

Figure 3.1: Sketch of neutron capture in a nucleus ^{A}X. The sum of the neutron separation energy and the kinetic energy of the neutron gives the level of excitation of the compound nucleus $^{A+1}$X. The decay to the ground state occurs via a multitude of possible γ-ray cascades (red lines).

must be irradiated by a neutron beam to obtain enough activity for deducing the cross section with the desired accuracy. With this technique it is only possible to measure an averaged cross section over the energy distribution of the neutron beam. The main advantages of this technique are the selectivity provided by the γ-ray spectroscopy with germanium detectors, and by the high sensitivity that can be achieved by the production of large neutron intensities [67].

On the other hand, the TOF technique can be applied to every nucleus and the cross section is measured by the direct detection of the prompt γ-rays generated by the capture events. Every γ-ray detection carries a twofold information: the time of the interaction provides the neutron time of flight and the energy deposition is related to the multiplicity. In this way, it is possible to extract the cross section versus neutron energies according to the achievable energy resolution, which depends on flight path, width of the neutron producing particle beam, and on a possible moderation. The TOF method requires isotopically enriched samples. This is usually a certain drawback, but it is necessary because the true signals from the investigated reaction are difficult to distinguish from events due to isotopic impurities. There are two different experimental approaches for the neutron capture TOF measurements:

1. All γ-rays generated by capture events are detected. The measurement of the total energy deposited by the γ-rays is a clear signature of the reaction as each (n, γ) event has a well defined cascade energy. This technique requires 4π detectors with an efficiency close to 100 % and it is usually referred as "calorimeter mode". It is applied when the competition between capture and scattering is favorable, as a very efficient detector is necessarily massive and, therefore, likely sensitive

to scattered neutrons.

2. At most one γ-ray of the cascade is detected. Detectors with low sensitivity have to be used in this case, which can turn into an advantage for the reduction of the background from scattered neutrons. However, the γ-ray efficiency of the detector turns out to be a delicate issue. A way to overcome this problem is by constructing a γ-detector with an efficiency proportional to the energy of the detected photon (Moxon-Rae detectors) or to achieve this condition by an a posteriori manipulation of the γ-response (Pulse Height Weighting Technique, PHWT see section 3.1).

The low-efficiency detection method has been employed in the present work, since the scattering cross sections are comparably large in case of the osmium isotopes.

3.1 Pulse Height Weighting Technique

The conditions of small efficiency (only one γ-ray detected per capture event) and proportionality to the energy of a detected γ-ray lead to *equal efficiency* for cascades of different multiplicity emitted by the compound nucleus. The detection efficiency of a capture event is:

$$\varepsilon_{\text{capt}} = 1 - \prod_{i=1}^{m}(1 - \varepsilon(E_{\gamma_i})) \tag{3.1}$$

where $\varepsilon(E_\gamma)$ is the detection efficiency for a γ-ray of energy E_γ, which is part of a cascade of multiplicity m. The conditions of small efficiency

$$\varepsilon(E_{\gamma_i}) \ll 1 \tag{3.2}$$

and an efficiency proportional to the energy of the photon

$$\varepsilon(E_{\gamma_i}) = kE_\gamma \tag{3.3}$$

leads to the approximation

$$\varepsilon_{\text{capt}} \approx \sum_{i=1}^{m} \varepsilon(E_{\gamma_i}) = k \sum_{i=1}^{m} E_{\gamma i} = kE_{\text{casc}}. \tag{3.4}$$

In this case, the probability to detect a capture event is proportional to the well defined energy of the cascade, $E_{\text{casc}} = S_n + E_n$.

The PHWT consists in applying a weight to every detected event to fulfill the condition 3.3. The constant of proportionality depends on the features of the detector used, but it is usually chosen to be equal to 1. The dependence

of the weighting factor on γ-ray energy is called weighting function (WF) [68].

It has been shown [69] that the best way to obtain the WFs is by Monte Carlo simulation of the detector response. In this way the influence of the sample under study and of the full detector geometry can be considered properly. Other processes such as the internal conversion can be also taken into account. In order to obtain accurate WFs one needs to include in the Monte Carlo calculation the material surrounding the sample and detectors. The realistic modeling of the sample itself (in terms of geometry and composition) is of relevance as it has been shown in reference [70].

For the PWHT, the identification of background is quite fundamental, as no direct information on the nature of the detected γ-rays is obtained. Consequently, a detailed analysis of the background has to be performed. A standard technique to identify the background is the "sample changer technique": the sample under investigation is mounted on a sample changer together with a set of samples, which are suitable to study the different background components. The exact background level for each sample can be evaluated experimentally by means of neutron filters. Neutron filters consist of materials with strong resonances, which are placed in the neutron beam. The thickness of the filters must be sufficient to remove from the beam all neutrons with the resonance energies, so that only background events are observed at the TOF intervals corresponding to the peak of the resonances. An alternative way to deduce the level of the background is by simulations. Both techniques can be coupled to increase the reliability of the evaluation.

3.2 Standards

The absolute neutron flux impinging on the sample is usually evaluated relative to some standard cross section. Correspondingly, a reference sample is mounted on the sample changer. Of course, the dependence of the neutron flux with the neutron energy must be known with good accuracy (see section 4.2).

The usual standard for (n,γ) cross section measurements relevant in nuclear astrophysics is the cross section of ^{197}Au. The most accurate ^{197}Au(n,γ) measurement (uncertainty of 1.5%) was performed via activation [71]. This cross section is commonly used as reference for activation measurements whenever the 25 keV quasi-thermal spectrum from the ^{7}Li$(p,n)^{7}$Be reaction is employed. This accurate value can also be used to normalize the differential (n,γ) cross section from an evaluated nuclear data library by folding with the known experimental spectrum from the ^{7}Li$(p,n)^{7}$Be reaction used in the measurement of reference [71]. The evaluated ^{197}Au(n,γ) cross section from the ENDF/B-VI library [72] has been also adopted for this purpose.

$MACS_{exp}$ (25 keV)	(mbarn)
Ratynski [71]	586 ± 8
ENDF [72]	622

Table 3.1: Comparison between the experimental value of MACS at 25 keV measured with the quasi-Maxwellian neutron spectrum from the $^7Li(p,n)^7Be$ and the averaged cross section obtained by folding the experimental energy spectrum and the ENDF/B-VI cross section [72].

The ENDF cross section has been folded with the quasi-Maxwellian 25 keV neutron spectrum from reference [71] resulting in a correction factor of 5.8% as shown in table 3.1.

Another way of determining the neutron flux is by the saturated resonance technique [73]. In this case, the gold sample has to be chosen thick enough that all neutrons at the resonance of 4.9 eV are captured. This fix the yield of the reaction to a value close to 1 (see section 5.8), which allows an accurate determination of the absolute neutron flux at 4.9 eV.

3.3 MACS

The cross section measured as a function of neutron energy via the TOF technique is suitable to calculate the MACSs for the ground state at different temperatures. The Maxwell-Boltzmann distribution for a certain temperature T is

$$f(v) = 4\pi \left(\frac{m}{2\pi kT}\right)^{\frac{3}{2}} v^2 e^{-\frac{mv^2}{2K_B T}}, \tag{3.5}$$

where m is the mass of the particle, v is velocity and k the Boltzmann constant. The averaged velocity is

$$< v >= \frac{2}{\sqrt{\pi}}\sqrt{\frac{2kT}{m}}, \tag{3.6}$$

while the most probable velocity (thermal velocity) is

$$< v_T >= \sqrt{\frac{2kT}{m}} = \frac{\sqrt{\pi}}{2} < v > . \tag{3.7}$$

The MACS is defined as

$$< \sigma >_{kT} = \frac{< \sigma v >}{< v_T >} = \frac{2}{\pi}\frac{< \sigma v >}{< v >}. \tag{3.8}$$

Integrated over energy instead of velocity, one obtains

$$< \sigma >_{kT} = \frac{2}{\sqrt{\pi}} \frac{\int_0^\infty \sigma(E_n) E_n e^{-\frac{E_n}{kT}} dE_n}{\int_0^\infty E_n e^{-\frac{E_n}{kT}} dE_n}. \tag{3.9}$$

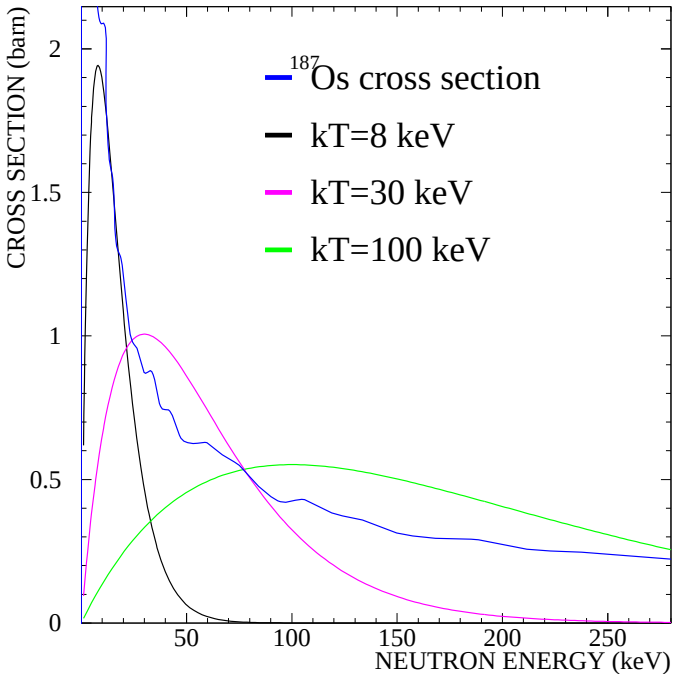

Figure 3.2: Maxwell Boltzmann distributions at different thermal energies (arbitrarily scaled) are shown together with the ^{187}Os cross section (see chapter 5). The MACS at different temperatures are determined by different energy intervals of the cross sections.

The MACSs at different temperatures are sensitive to different neutron energy ranges, as it is shown in figure 3.2, where one of the cross sections measured in this work is shown together with different Maxwell-Boltzmann distributions.

Chapter 4

Capture cross sections of ^{186}Os, ^{187}Os, and ^{188}Os

The (n,γ) cross sections of ^{186}Os and ^{187}Os are the relevant neutron capture data for the Re/Os cosmochronometer. Both can be measured only via the TOF technique. The investigated energy range must be wide enough to allow the reliable determination of the MACS for the temperature regime of the *s* process in thermally pulsed low mass AGB stars, from about 8 keV to 25 keV. This means that the cross sections must be measured from 0.1 keV to 300 keV to extract all the relevant astrophysical information. Isotopically enriched osmium samples have been loaned from Oak Ridge National Laboratory. ^{188}Os is the largest contaminant, thus, its cross section has been measured as well, using the very pure sample listed in table 4.1.

It has been already discussed that the stellar rate of ^{187}Os needs a theoretical correction due to the effect of thermally populated low lying excited states (section 2.4). The corresponding corrections are obtained by Hauser Feshbach calculations, which need reliable input parameters based on experimental data, i.e. averaged level densities and gamma strength functions. This information can be determined by the analysis of the resolved resonance region between thermal energies and some keV.

The CERN spallation neutron source n_TOF (see section 4.2) is particularly suitable for these measurements because it covers a wide neutron energy spectrum from 0.025 eV to 250 MeV with excellent TOF resolution.

4.1 Previous measurements

Previous (n,γ) cross sections for ^{186,187}Os were reported in limited energy ranges only, from 2.75 keV to 2.65 MeV [60] and from 1 keV to 135 keV [15]. Moreover, experimental information below 1 keV is rather incomplete [74], leading to large uncertainties in the calculation of Maxwellian Averaged Cross Sections (MACS) at the low thermal energies typical of the interpulse

phases of AGB stars [38]. Both measurements used neutron beams from (γ, n) reactions on heavy nuclei induced by bremsstrahlung photons and applied the PHWT to extract the cross section. It seems that in both cases a rather simple approach was used to determined the WF. At present, sophisticated Monte Carlo codes can be used to model in detail the experimental setup and to describe the electromagnetic interactions more reliably. In this way, realistic detector responses and correspondingly accurate WFs can be determined [69]. These data were in good agreement for ^{187}Os and ^{188}Os

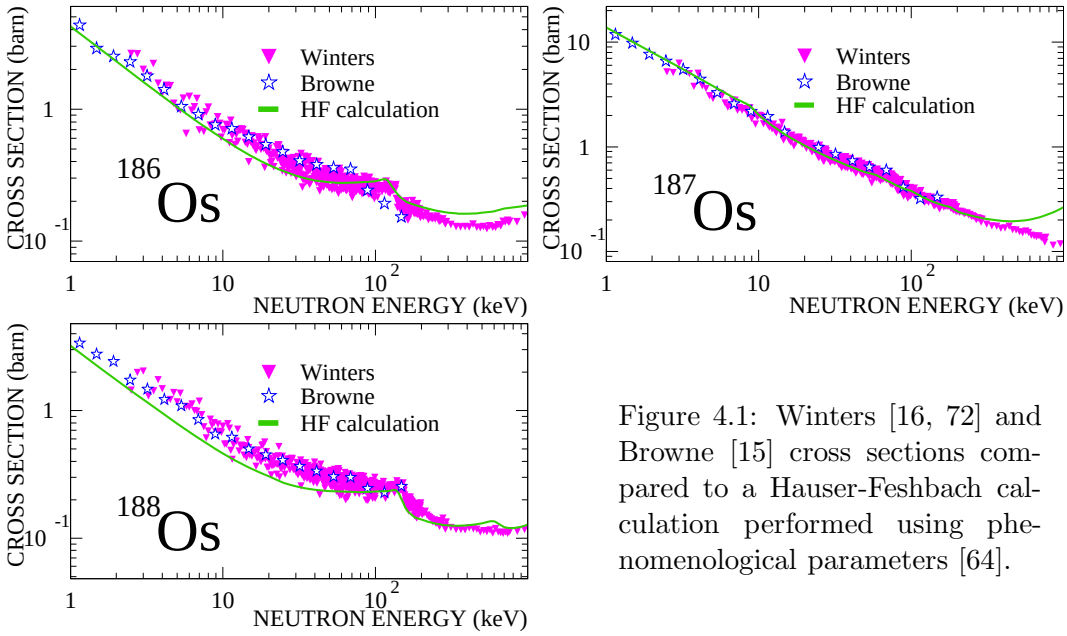

Figure 4.1: Winters [16, 72] and Browne [15] cross sections compared to a Hauser-Feshbach calculation performed using phenomenological parameters [64].

but showed discrepancies for ^{186}Os, especially around the energy of the first excited level at 137 keV. A theoretical calculation based on the available total cross sections [72], level densities, and strength functions [75] deviates for the even isotopes ^{186}Os and ^{188}Os, especially for the latter case, as shown in figure 4.1. Other Hauser Feshbach calculations [63, 65] based on global parameters are even more discrepant.

New more accurate neutron capture measurements are clearly called for to improve the present uncertainties and to extend the neutron energy range at least down to 0.1 keV.

4.2 n_TOF facility

Neutrons are produced at n_TOF by spallation of 20 GeV/c protons on an 80×80×60 cm^3 lead target. The beam is delivered by the CERN proton synchrotron (PS) accelerator complex in bunches of 4 to 7 $\times$ 10^{12} protons with a pulse width of 6 ns and typical repetition rate of 0.4 Hz. The

integrated number of protons is measured with an accuracy of 1% by a pick up monitor, which is placed close to the lead target. Every proton produces in average about 300 neutrons with a large momentum in the direction of the proton beam. The initial angular distribution is homogenized by scattering in the lead target, which also contributes to soften the neutron spectrum. Finally, neutrons leaving the lead target are moderated in a 5.7 cm thick layer of coolant water surrounding the target. Starting at the surface of this water moderator, the neutrons enter an evacuated flight path that is built at an angle of 10 deg with respect to the proton beam direction.

The neutron beam line has an entrance window of structured aluminum 1.6 mm in effective thickness. The spatial distribution of the neutron beam is determined by two collimators, placed at 135.54 m and 175.35 m from the lead target. At the experimental area 185.5 m from the spallation target, the beam profile is nearly Gaussian with a 2 cm FWHM. The conversion

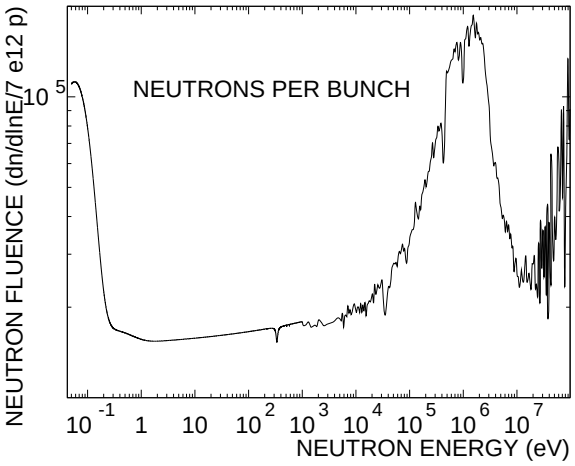

Figure 4.2: Isolethargic n_TOF flux at the experimental area.

from TOF to neutron energy must take the time for moderation inside the target assembly into account. This is done by considering the real flight path L as the sum of the geometrical flight path L_0 between the outer face of the moderator and the sample and an energy dependent distance $\Delta L(E_n)$ representing the averaged path length in the lead target and the moderator,

$$L(E_n) = L_0 + \Delta L(E_n). \tag{4.1}$$

The "moderation distance" $\Delta L(E_n)$ can be determined by simulations and checked experimentally by measuring well known narrow resonances [76]. The moderation distance at n_TOF shows an energy dependence,

$$\Delta L(E_n) = -\frac{\sqrt{E_n}}{72.2977} t_0, \tag{4.2}$$

with $t_0 = (-68 \pm 13)$ ns as determined experimentally [76]. Substitution of

equation 4.2 into the classical kinetic energy expression

$$E_n = \frac{1}{2} m_n v^2 \tag{4.3}$$

leads to the TOF-energy relation

$$E_n = \left(\frac{72.2977 L_0}{t + t_0} \right)^2 , \tag{4.4}$$

where, the moderation is taken into account as a fixed time offset. In the energy range of relevance for astrophysics, which is studied in this work, relativistic corrections can still be neglected.

With the long n_TOF flight path an energy resolution of 3×10^{-4} at 1 eV, 5.5×10^{-4} at 1 keV, 1.1×10^{-3} at 30 keV, and 4.2×10^{-3} at 1 MeV is achieved [77]. The isolethargic flux per bunch of 7×10^{12} protons [78, 79, 80] is shown in figure 4.2. The employed data acquisition system (DAQ) based on Flash Analog to Digital Converters (FADC) with 8 Mbyte buffer memory allows to cover a time window of 16 ms. This TOF interval corresponds to a lower limit for the neutron energy of ~ 0.7 eV, sufficient also for investigating the resolved resonance region. The neutron flux per energy decade and per proton bunch is of the order of 4.5×10^4 neutrons between 1 and 10 eV, 7.1×10^4 between 10 and 100 keV, and 2×10^5 neutrons between 0.1 and 1 MeV [77].

Together with the neutrons many other particles are generated in the lead target as well and act as a potential source of background. This background is suppressed by massive concrete shieldings and by a 3.5 m thick iron wall. Photons and highly relativistic particles generated directly by the proton interactions and traveling along the beam pipe are separated from the neutrons by TOF and are actually used to mark the time zero point (also called γ-*flash*) in the TOF spectrum. Slower charged particles are removed from the beam by a 2 m long dipole magnet placed in the beam line at 145 m from the lead target.

Most problematic are the photons from neutron capture in the material surrounding the target and especially in the hydrogen of the cooling water. These photons are mainly produced in an interval from 1 μs to a few 100 μs after the proton pulse and arrive in the experimental area together with neutrons in the keV range. The background produced by Compton scattering of the photons in the sample is crucial and requires careful subtraction. The photon energy distribution is mostly determined by the 2.2 MeV line from neutron capture in hydrogen, which is too high to be simply discriminated by increasing the pulse height threshold in the gamma detectors. A set of removable neutron filters at 135 m from the target are used for measuring this background.

4.3 Experimental setup

The n_TOF setup consists of two C_6D_6 liquid scintillators with minimized neutron sensitivity. This is an essential advantage, since γ-background from neutrons scattered in the sample and captured in the detectors or in the immediate proximity is indistinguishable from true capture events in the sample under study. Thus, the detectors consisted only of the photomultiplier tube (EMI 9823QKA without quartz window), the liquid scintillator (1 l for each detector), and the scintillator cell held in position by light fabric (see figure 4.3). The scintillator cell and the sample changer were built from carbon fiber because of the very small neutron capture cross section of carbon [81]. The detectors were placed perpendicular to the neutron beam line, at a distance of 3 cm from the beam axis. A sketch of the setup is

Figure 4.3: Scintillation counters with minimized neutron sensitivity employed at n_TOF.

shown in figure 4.4.

The samples are mounted on a sample ladder made from a carbon fiber strip and operated by a stepping motor. The neutron beam pipes, which consisted of very thin stainless steel tubes, were closed before and behind the samples by thin Mylar windows. The detectors were mounted 9.8 cm upstream of the samples to reduce the background due to in-beam γ-rays.

A neutron monitor consisting of a thin ^{6}Li foil (200 μg/cm^2 evaporated onto a 1.5 μm Mylar foil) has been used for additional flux measurements [79]. The ^{6}Li foil, which is placed in the beam line at 183.5 m in a separated carbon fiber chamber, was surrounded by four silicon crystals completely outside the neutron beam for detecting the products of the $^6\mathrm{Li}(n,\alpha)^3\mathrm{H}$ reaction.

4.4 Samples

The isotopic composition of the enriched sample material is given in table 4.1. The metallic osmium powder was encapsulated in 0.1 mm thick

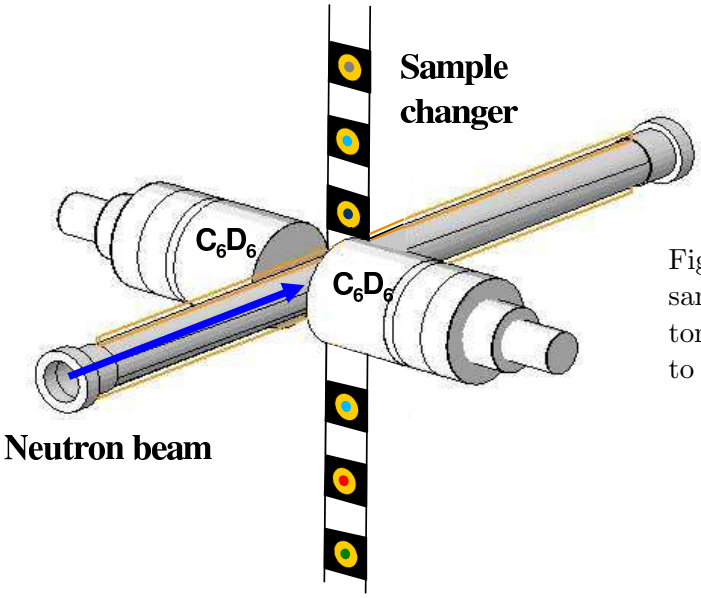

Figure 4.4: Sketch of sample changer, detectors and beam line close to the samples.

aluminum cans 15 mm in diameter (a picture of one of these sample is shown in figure 7.3 as part of the setup used for the inelastic scattering experiment).

	Isotopic composition (%)					
Sample	186	187	188	189	190	192
^{186}Os	78.48	0.91	4.88	4.29	5.09	5.32
^{187}Os	1.06	70.43	12.73	5.13	5.42	5.21
^{188}Os	0.11	0.12	94.99	2.55	1.27	0.97

Table 4.1: Isotopic composition of the osmium samples. Other contaminants were present only at the ppm level.

During the measurements, the following samples (all 15 mm in diameter) have been mounted on the sample ladder:

^{186}Os, ^{187}Os; the isotopes under study,

^{188}Os as the main isotopic impurity,

^{197}Au for flux normalization,

^{nat}C to measure the effect of scattered neutrons,

^{nat}Pb for monitoring the background from in-beam γ-rays,

an empty sample container to correct for the capture events in the aluminum can, and an

empty position for measuring the ambient background.

The sample characteristics are summarized in table 4.2. The alignment of the samples was performed by means of a camera that could be fixed to the beam line. This procedure, together with the equal diameter of all samples, is fundamental for obtaining the correct information from the sample changer technique. The lead sample was best suited to measure the in-beam γ-background because of the large Z and the small (n, γ) cross section of all lead isotopes. The effect of neutrons scattered by the sample was studied by a carbon sample made of pressed graphite. Carbon was used for its very small (n, γ) cross section and its low Z, which makes it practically transparent to in-beam γ-rays.

Table 4.2: Characteristics of the samples

Sample	Form	Mass (g)	Thickness (10^{-3} atoms/b)
^{186}Os	metal powder	1.9999	3.714
^{187}Os	metal powder	1.9212	3.549
^{188}Os	metal powder	1.9967	3.669
^{197}Au	metal	1.299	2.241
^{nat}Pb	metal	2.027	3.171
^{nat}C	pressed graphite	0.479	13.48

4.5 Data taking

The runs with the osmium samples have been defined such that statistical errors were significantly smaller than systematic uncertainties. The

Sample	Number of protons/run (in units of 10^{16})	
	full beam	with filters
^{186}Os	49.9	8.71
^{187}Os	28.9	6.73
^{188}Os	51.7	8.31
^{197}Au	19.7	14.1
^{nat}Pb	14.4	16.4
^{nat}C	1.11	
empty can	7.1	
empty	1.95	

Table 4.3: Number of protons on the lead target for each combination of sample and filters.

reliability of background subtraction has been improved by specific measurements with neutron filters in the beam. This was not only made for the osmium samples, but also in the gold and lead runs. For gold it was important, because the employed standard (section 3.2) is defined in the keV region [71], where the background generated by in-beam γ-rays is largest. In order to define this background from the spectra taken with the lead sample, runs with filters were necessary to correct for the photon absorption in the filters properly. The number of protons employed in each of the runs is listed in table 4.5. Perfect proportionality between number of protons and counts in the neutron monitor has been always confirmed.

Chapter 5

Analysis and results

The detector signals have been recorded with fast digitizers. The flash amplitude to digital converters (FADC) had a resolution of 8 bit per channel, a buffer memory of 8 MByte, and a sampling rate from 100 to 500 MHz. This data acquisition system (DAQ) is virtually dead time free since the entire detector output is stored for a period of 16 ms with a typical resolution of 2 ns/channel. These 16 ms correspond to a minimum neutron energy of 0.7 eV. In capture measurements with C_6D_6 detectors the upper energy limit of 1 MeV results from the opening of inelastic channels. The trigger for the DAQ comes from the pick-up signal of the accelerator. For each proton bunch, the time zero point in the TOF spectrum was derived from the γ-flash, by an off-line analysis routine. For each event following the γ-flash the TOF, pulse height, and integrated charge were determined by off-line analysis.

5.1 Steps of the analysis

The analysis of the data has been divided into two energy regions: resolved resonance region and continuum. The separation between these two energy ranges is usually determined by the resolution in neutron energy. The present resonance analysis was challenged by the fact that many resonances in the isotopic impurities of the samples are still unknown or missing in the databases [74]. The resonance parameters of resolved resonances have been obtained up to neutron energy of 3.3 keV, 2.0 keV, 5.0 keV for ^{186}Os, ^{187}Os, and ^{188}Os, respectively. The determination of the average capture cross section of the continuum was extended to lower neutron energies of 3 keV and 2 keV for the even isotopes and for ^{187}Os, respectively. In this way, the neutron energy range where both resolved resonance region and unresolved resonance region overlap, allowed to check the consistency of these two independent analysis. These limits have been chosen as lower as possible on the basis of the reliability of the correction for self shielding and

neutron multiple scattering for the continuum. This correction has been indeed calculated using a theoretical model considered to be reliable only beyond 5 keV (see section 5.10 for details). However, also at lower energies, a good agreement was found between the averaged capture cross sections and the corresponding averaged cross section calculated from the parameters obtained in the analysis of the resolved resonance region. The final cross sections are evaluated by joining the continuum and resolved resonance region at these energy limits. In summary, the raw capture data was analysed according to the following steps:

1. Energy calibration of the scintillators.
2. Renormalization of the different runs.
3. Check of the stability of the gain of the detectors and of the setup.
4. Determination of the proper threshold for the energy deposition.
5. Rejection of coincidences in the two detectors to correct for double counting since the PHWT assumes detection of only one γ-ray per capture event.
6. Application of the PHWT.
7. Evaluation and subtraction of the sample dependent background.
8. Absolute normalization by evaluation of the neutron flux.
9. Resonance analysis.
10. Correction for multiple scattering and self shielding effects in the continuum.
11. Isotopic correction.
12. Calculation of the MACS.

5.2 Energy calibration

The light output of the C_6D_6 scintillators was periodically controlled by means of the monoenergetic γ-ray sources listed in table 5.1. The amplitude as well as the integrated area of the anode signals can be used for calibration. Area and amplitude are correlated because the routine for calculating the pulse characteristics derives both parameters by a fit with a standard pulse shape. It has been verified that the used detectors show a linear relation between deposited γ-ray energy and area (or amplitude) of the pulses. The detector responses have been fitted with a simulated energy deposition spectrum generated by monochromatic γ-rays with the energy of the sources, as

γ-source	γ-lines
^{137}Cs	662 keV
^{60}Co	1.173 MeV
	1.332 MeV
^{13}C$(\alpha, n)^{16}$O	6.13 MeV

Table 5.1: The γ-sources used for energy calibration of the C_6D_6 detectors.

shown in figure 5.1. The six calibrations performed during the experiment confirmed the gain stability of the detectors. The largest gain drifts of the two detectors were 2% and 5% for 1 MeV γ-rays, respectively. The energy of the detected γ-rays is fundamental for the application of the PHWT, but the effect of these small gain drifts is negligible due to the smooth behaviour of the weighting functions (see section 5.6).

5.3 Relative run normalization

The data taking has been organized in different runs. For each of these runs the flux normalization (independent of the absolute flux normalization that will be discussed in section 5.8) is needed to relate the count rates of the different samples. The number of protons on the spallation target and the counts in the ^{6}Li neutron monitor can be used for this purpose. Normalizing to the number of protons has the advantage that the proton current can be measured to better than 1%, but does not account for variations in the neutron beam due to re-arrangements of the collimators. Therefore, normalizing to the number of counts in the ^{6}Li neutron monitor is preferred, but requires a careful check of the stability of the four silicons detectors. During the present experiment the proton beam pick-up and the silicon detectors of the ^{6}Li monitor were stable and in agreement. Hence, both normalizations were completely equivalent.

In runs with neutron filters, however, only the neutron monitor can show the flux reduction.

5.4 Pulse height threshold

A zero suppression algorithm is used to record data only when the signal is larger than a certain threshold set in the FADC. This allows to reduce between a factor of 10 and 100 the amount of data to be transferred and stored into the DAQ-PCs. An additional off-line threshold is rendering the data insensitive to fluctuations in the base line level. In the n_TOF measurements with C_6D_6 detectors, this threshold was defined after the energy calibration. Large parts of the background are dominated by low energy signals. Hence, the threshold affects mostly the background level and any

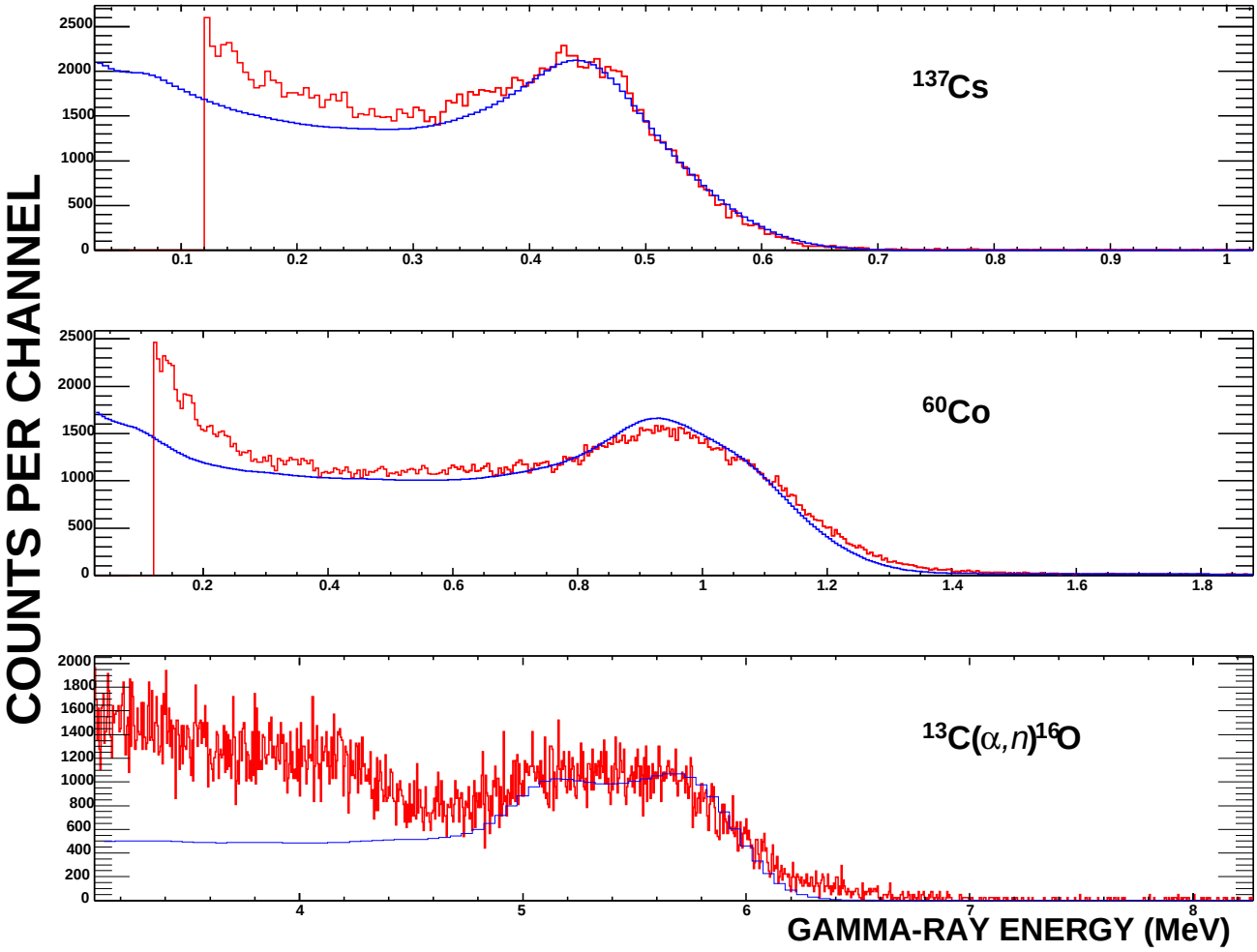

Figure 5.1: Energy calibration of the C_6D_6 detectors using the γ-sources of table 5.1. The measured pulse height spectra (red histogram) were fitted with the simulated energy deposition (blue). In this way also the energy resolution of the C_6D_6 detectors was calibrated. It is worth to note the absence of the photoelectric peak, because the energy deposition is dominated by the Compton effect. The differences between the measured spectra and the fit is due to the ambient background which was neglected in the simulations. The spectrum taken with the $^{13}C(\alpha, n)^{16}O$ reaction is also effected by neutron-induced background.

change of the threshold requires a new background evaluation. The threshold for the present measurement has been fixed at a level corresponding to a deposited energy of 200 keV.

5.5 Coincidence rejection

The PHWT assumes the detection of only one γ-ray per cascade. Coincidences between the two scintillators must be corrected to avoid the problem of double counting the same event. In case of coincidences in the two detectors one of the signals is rejected from further analysis. Coincidences have been defined as events detected in a time window of 20 ns [82, 83]. This window has been tested to be optimal also for the high count rate in the large first resonance of gold even at the high flux conditions during this measurement. The coincidence probability, which depends on the γ-cascade and differs for the various samples, averaged over the entire neutron energy range is small in all cases (see table 5.2), indicating that the uncertainty of the related correction is negligible.

Sample	Coincidence probability (%)
^{186}Os	2.7
^{187}Os	3.2
^{188}Os	2.5
^{197}Au	2.5
^{nat}Pb	0.99
^{nat}C	1.1
empty	0.72

Table 5.2: Coincidence probability for each sample. The samples used for background determination (Pb, empty and C) are showing small probabilities due to the lack of capture cascades.

5.6 PHWT

The PHWT has been introduced in chapter 3.1. The basic assumption that the γ-ray detection efficiency must be proportional to the energy of the registered γ-ray can be written as

$$\varepsilon_\gamma = \sum_{i=1}^{n} W_i R_i^\gamma = kE_\gamma, \tag{5.1}$$

where R_i^γ is the detector response function for a γ-ray of energy E_γ, (the index i refers to the energy bins of the measured or simulated spectrum of energy deposition), and W_i is the weight that must be applied to the i-th bin of the deposited energy spectrum. The proportionality coefficient k is usually chosen equal to 1 in the calculation of the weighting functions. However, the absolute efficiency is always difficult to determine only from a Monte Carlo simulation. Therefore, the proportionality constant k, together with the an absolute flux normalization constant, is determined experimentally, from the measurement of a reference cross section (see section 5.8).

nucleus	S_n (MeV)
^{186}Os	6.2900
^{187}Os	7.98956
^{188}Os	5.9203
^{197}Au	6.51234
^{189}Os	7.7915
^{190}Os	5.75866
^{192}Os	5.5851

Table 5.3: Neutron separation energies for the nuclei under study.

The weight factors W_i can be parameterized as a polynomial of order q for the deposited energy E_i

$$W_i = \sum_{j=0}^{q} a_j E_i^j \tag{5.2}$$

The factors a_j are determined by a least square fit of a set of simulated response functions R_i^l, where l represents different energy of the simulated γ-rays. It was found that a polynomial of order 4 was enough to fulfill the proportionality condition 5.1 with the required accuracy. The detection efficiency of a capture event is obtained from summing the γ-ray cascade with multiplicity m (see equation 5.1).

$$\varepsilon_{\text{capt}} \approx \sum_{j=1}^{m} \left(\sum_{i=1}^{n} W_i R_i^{\gamma} \right)_j = k \sum_{j=1}^{m} E_{\gamma j} = k E_{casc}. \tag{5.3}$$

With the use of the weighting function, the efficiency is independent of the details of the cascade. Every detected event is consequently counted as $\frac{W_i}{E_{casc}}$ to have a constant efficiency among cascades of different energies or multiplicity. Capture events in the impurities are not properly weighted and this has to be taken into account in the isotopic correction (see appendix A).

The weighting functions for the osmium and gold samples have been determined independently by CEA (Saclay) [84] and INFN (Bari) [85] using MCNP and GEANT3.21 simulation tools, respectively. The different functions are shown in figure 5.2. In spite of the differences at higher energies, they are leading to quite similar capture yields, because a considerable part of the γ-rays have energies around 1 MeV, where the functions are in better agreement. The systematic uncertainty resulting from the determination of the weighting functions was estimated by comparison of the count rates obtained with the weighting functions from MCNP and GEANT3.21. This results in differences of 1%, 0.4%, and 0.4% for ^{186}Os, ^{187}Os, and ^{188}Os, respectively. These differences have been adopted as the systematic uncertainties due to the uncertainty of the weighting functions.

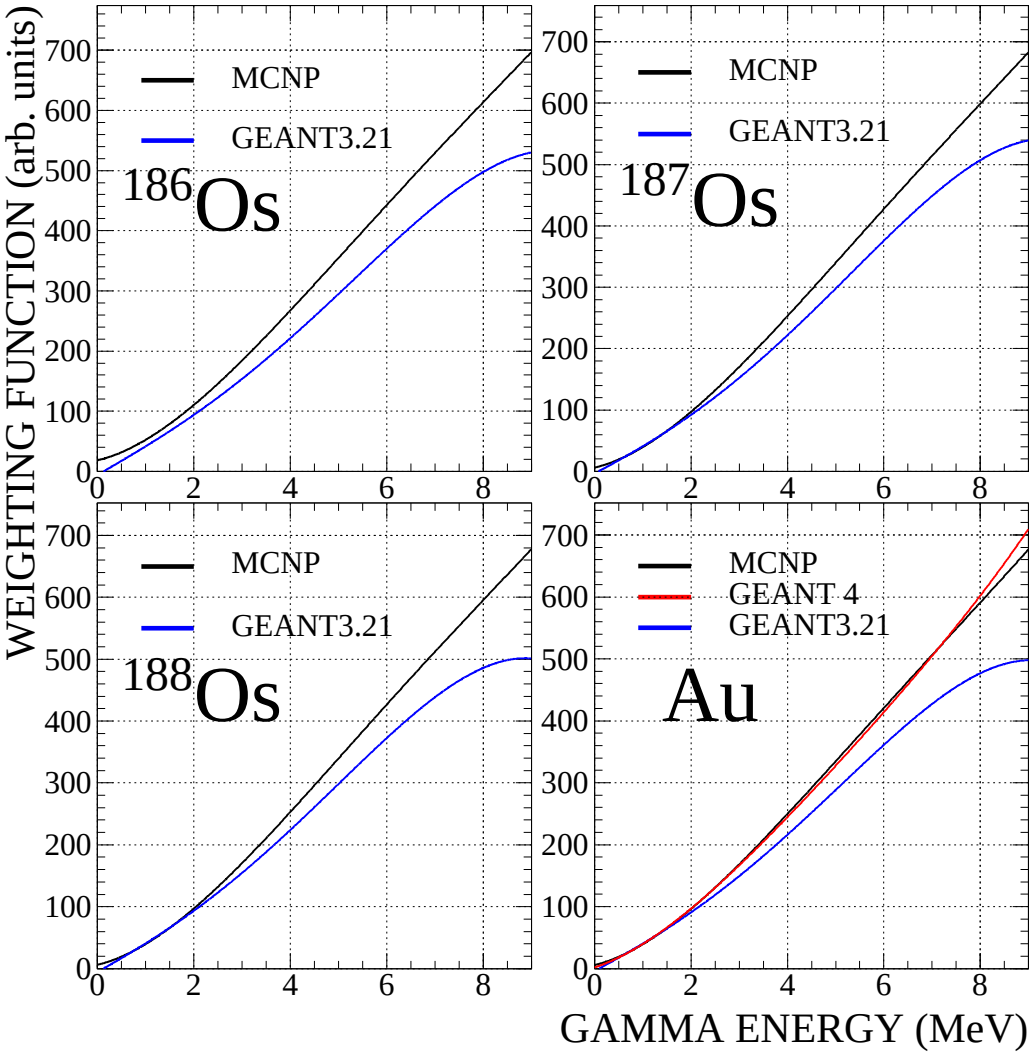

Figure 5.2: Weighting functions for the measured isotopes and for gold.

For gold, an additional weighting function was calculated at IFIC Valencia [86] using GEANT4. This additional calculation yields a WF which is very similar to the MCNP weighting function. Again, the different gold WFs produce relative differences in the capture yield of $\leq 1\%$. The uncertainty on the capture yield due to the PHWT itself has been determined at n_TOF from dedicated measurements [77]. The latter uncertainty includes experimental sources of systematic uncertainty like corrections for multiple scattering and self shieldings.

5.7 Background subtraction

A large part of the n_TOF backgrounds can be identified by means of the sample changer technique (see section 4.3), in particular the ambient background (measured directly by the count rate of an empty frame), the background due to scattering of in-beam γ-rays (obtained by the count rate of the lead sample), and the background due to capture of sample scattered neutrons in or near the scintillators (determined via the carbon sample). In the analysis of the osmium and gold spectra, all backgrounds are treated by the PHWT as they were true capture events. Therefore, the events of the lead and carbon samples must be weighted using the same weighting function and neutron separation energy than events from the capture sample under analysis.

In figure 5.3, background spectra are shown together with the count rate of ^{186}Os, all treated with the same weighting function. The spectra of the empty position and the empty can as well as of the lead and carbon samples are almost perfectly representing the energy and time dependence of the background. Only a few narrow capture resonances in the lead spectrum had to be excluded in the fit of the smooth energy dependence. Instead, the aluminum resonance at 34 keV in the spectrum of the empty can had to be included in the background subtraction. The spectrum on the empty position differs from the spectrum of the empty can only for the presence of this resonance, as the contribution form the neutron capture in aluminum is elsewhere negligible.

The total background level is determined by combining the contributions of the empty position and of the lead and carbon samples with background runs made with black neutron filters and with detailed simulations of the scattering of in-beam γ-rays by the samples. The measurements with the filters can not be used independently, even if these are the only direct measurements of the background, since only a few energy points are available and not all with suitable transmission and statistics. Because the statistics at the bottom of the "black resonances" is in general poor, Monte Carlo simulations using neutron elastic scattering cross sections from the databases are used to complement these measurements. This technique has been found to be successful also in other n_TOF measurements [87, 88].

The systematic uncertainty in the background evaluation was estimated by comparing a pure experimental approach based only on the measurements with the filters (section 5.7.2) with the complementary approach based on Monte Carlo calculations (section 5.7.3).

An additional background is due to the detection of γ-rays from $(n, n'\gamma)$ events and from deuteron recoils. Inelastic scattering channels are opening at different energies for each isotope, while deuteron recoils are present only at very high neutron energies, because they require neutron energies in excess of several hundred keV. Both events produce only small signals in the C_6D_6

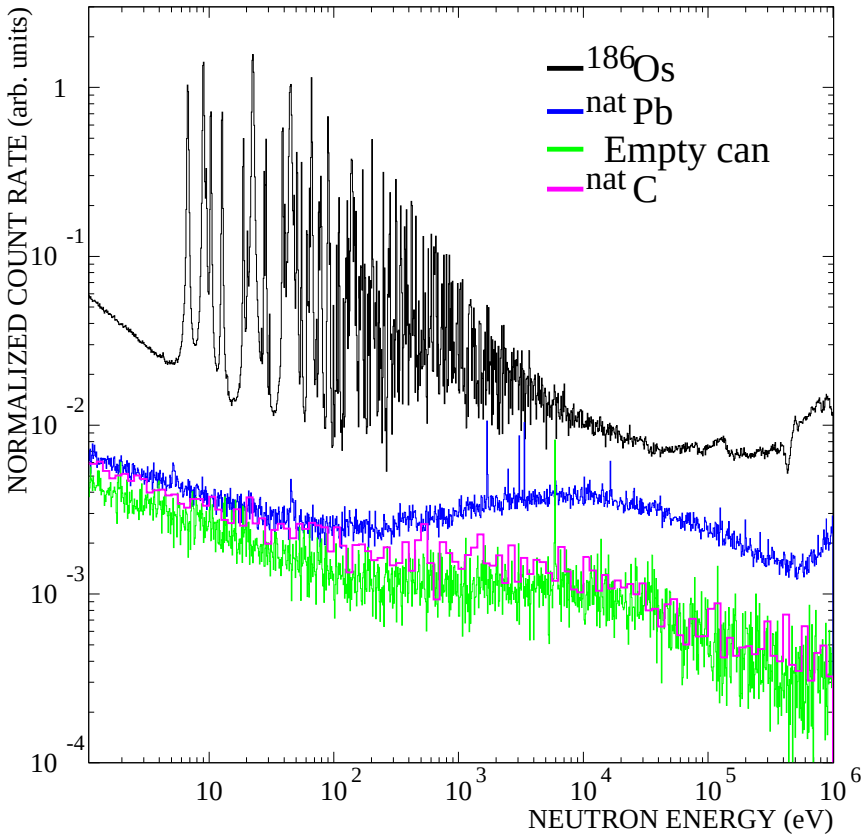

Figure 5.3: TOF spectra obtained with the different samples. The count rate from ^{186}Os shows resolved resonances at low energy and the signature increasing of the neutron flux around 300 keV (see figure 4.2). The count rate obtained with the empty can shows the ambient background that is exceeded by is an additional background in the keV region due to the scattering of in-beam γ-rays. The small extra background at low energy is due to neutron scattering measured with the carbon sample.

scintillators, and can be cut off by increasing the energy threshold. Because a higher threshold is affecting the cross section and because this background starts only after 500 keV, it was decided to change the threshold only in this energy region. The analysis was repeated using different thresholds and these results were renormalized to the cross section determined with the common 200 keV threshold.

5.7.1 Background level as function of neutron energy

The different components of the background have a different TOF dependence (see figure 5.3). The ambient background is measured directly by the empty position and does not need any rescaling or manipulation besides

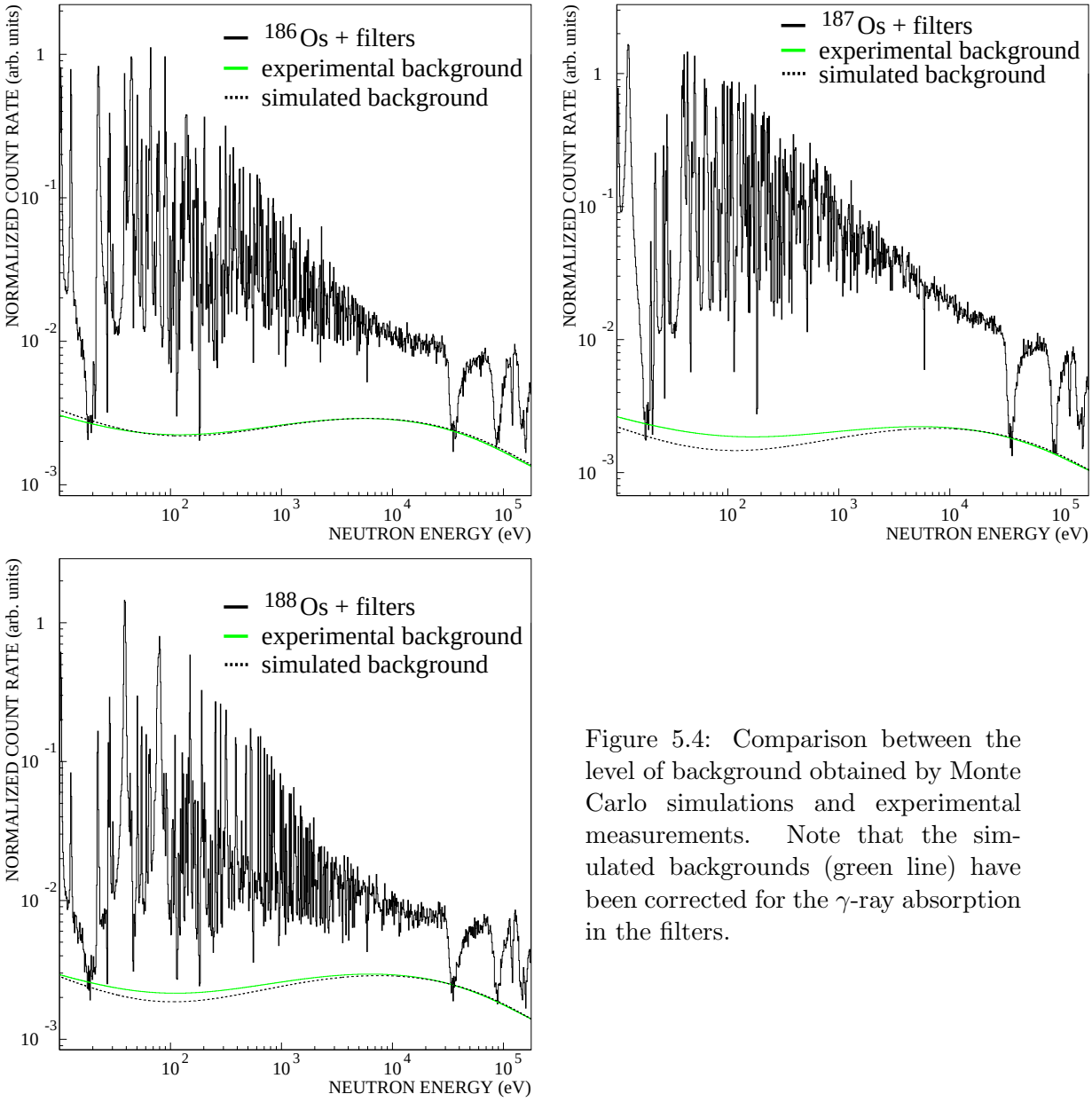

Figure 5.4: Comparison between the level of background obtained by Monte Carlo simulations and experimental measurements. Note that the simulated backgrounds (green line) have been corrected for the γ-ray absorption in the filters.

application of the proper PHWT. The spectrum of the empty position has been subtracted from the spectra of the other samples after normalization to the number of counts in the silicon monitor and application of the PHWT. The empty can was instead subtracted to the osmium sample, as it is showing only the ambient background apart for one aluminum resonance. The energy dependence of the in-beam gamma background is obtained by the lead spectrum minus the ambient background. Correspondingly, the neu-

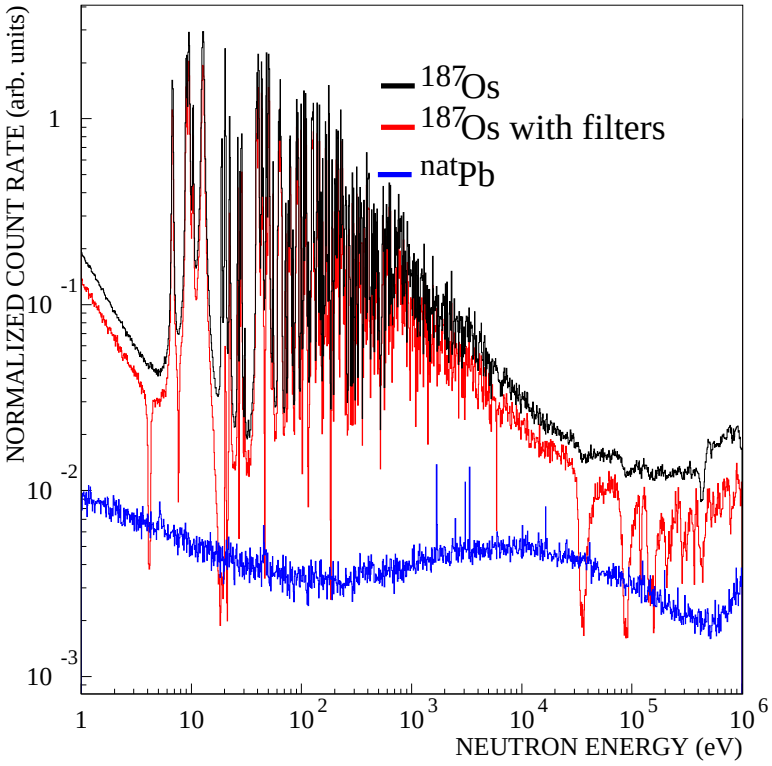

Figure 5.5: Spectrum of the ^{187}Os sample with and without filters normalized to the number of protons impinging on the spallation target. The spectrum of the lead sample without filters in beam is shown for comparison but without correction for γ-ray absorption in the filters.

tron scattering background is determined by the spectrum of the carbon sample.

A polynomial fit has been used to describe these smooth backgrounds in order to avoid statistical fluctuations. These background components must be properly normalized in order to get the actual background level in the spectra of ^{186}Os,^{187}Os, ^{188}Os, and ^{197}Au. On one hand, the normalization factors can be determined by means of the measurements with filters. This procedure is described in section 5.7.2. On the other hand the background normalization factors can be also calculated on the basis of Monte Carlo calculations, as described in section 5.7.3. In the present work, the information obtained from these two approaches was combined in order to determine the final background level with improved accuracy.

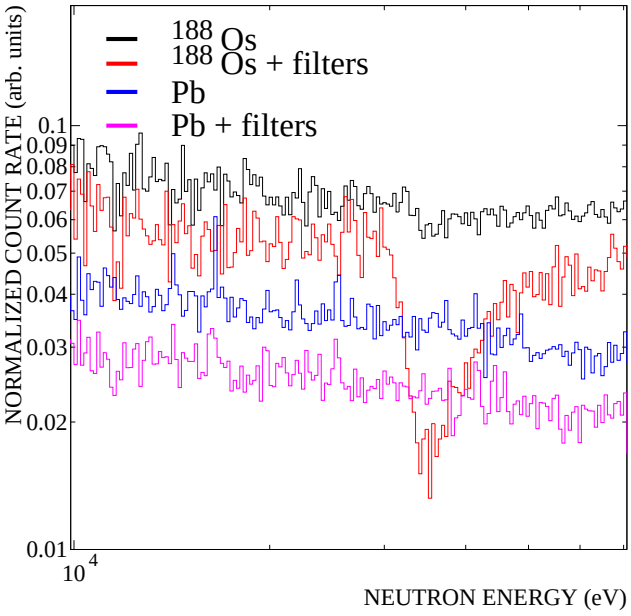

Figure 5.6: Effect of the filters at the 34 keV black resonance for ^{188}Os and lead. The spectra are normalized to the number of protons impinging on the spallation target, and the ^{188}Os weighting function is used in all cases shown. Only the ^{188}Os spectrum shows the effect of the filter, whereas the lead spectrum (which is not sensitive to neutrons because (n,γ)-reactions in lead are negligible) shows only a general reduction due to γ-ray attenuating in the filter.

5.7.2 Experimental determination of the background

The sum of all background components has to match the background level measured with the filters, considering the proper correction for γ-ray absorption in the filters. The background level can be obtained by scaling to the bottom of the 34 keV resonance of aluminum as shown in figure 5.4.

The filter resonances at 18 eV in tungsten and at 90 keV in aluminium are almost but not completely black and require small corrections. Nevertheless, the resonance at 18 eV was used as black in first approximation to obtain the background level also at low neutron energies. It has to be noted that the filters are attenuating not only the neutrons at the energies of the black resonances but also the in-beam γ-rays (see figure 5.5). This absorption has been determined by measuring the spectra of the lead sample with and without filters. The level of the background that can be obtained at the bottom of the black resonances must be corrected for this attenuation factor, resulting in the green lines of figure 5.4.

5.7.3 Monte Carlo approach and validation

The absorption resonance at 18 eV represents only an upper limits for the total background level because it is not completely black. A more precise determination of the background level in the eV region can be performed via Monte Carlo simulations of the neutron and γ-ray induced backgrounds. The neutron scattering background is calculated by comparing the neutron elastic cross section of the nucleus under analysis. The spectrum of in-

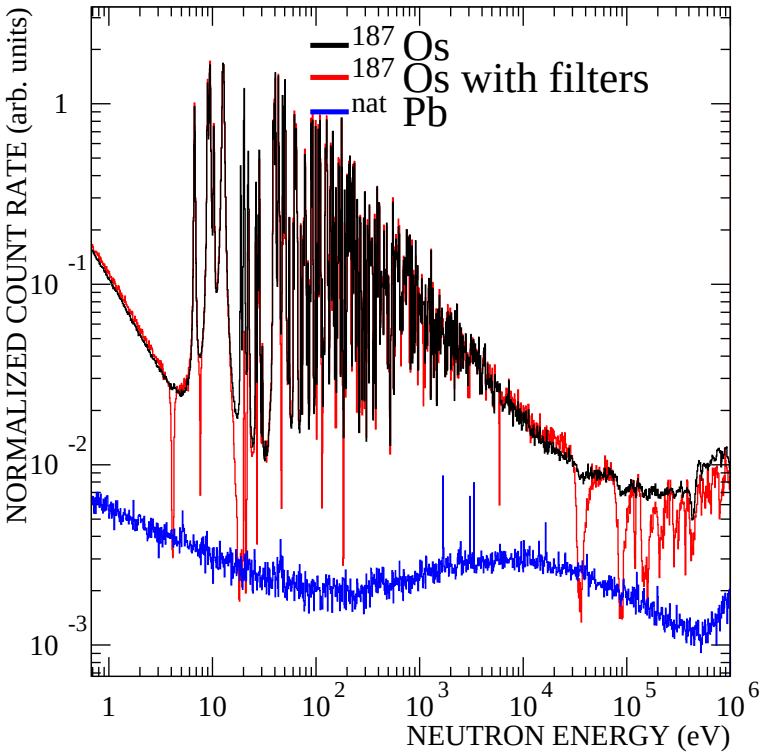

Figure 5.7: Spectra of ^{187}Os with and without filters normalized to the counts in the silicon monitor. The spectrum of the lead sample without filters in beam is shown for comparison. The corrected spectrum obtained with the filters appears to exceed the one without filters, if the γ-absorption in the filter is not corrected properly.

beam γ-rays produced near the spallation target [89] and the corresponding interaction with the samples (osmium, gold, carbon, and lead) is simulated using GEANT3.21.

The comparison between the simulated effect of γ-rays scattered by the lead sample related to the other samples allows one to normalize the in-beam γ-ray background measured with the lead sample.

The result of this evaluation is given by the dotted line in figure 5.4 (the background for gold will be shown and discussed later). Considering the statistical uncertainties on the filter measurements, the so obtained background level is in very good agreement with the experimental measurement, both for the black resonance at 34 keV and for the upper background level given by the bottom of the filter resonance at 18 eV.

Due to the different signal to background ratios in the spectra of the three osmium isotopes, the cross sections are differently sensitive to changes of the background level. The two levels of background shown in figure 5.4

are affecting the MACS at 30 keV by 2%, 1%, and 3% for ^{186}Os, ^{187}Os, and ^{188}Os, respectively.

The spectra for ^{188}Os and lead measured with and without filters are shown in figure 5.6 for the energy region around 34 keV. The attenuation of the γ-ray background is difficult to evaluate using the normalization to the number of neutron in the neutron monitor because the reduction of the γ-rays in the C_6D_6 response is compensated by the reduction of neutron detections in the monitor. In the code evaluating the background at the bottom of black resonances, this effect has been considered by normalizing the attenuation of the count rate from the lead target with filters and without filters by the number of protons on target. As shown in figure 5.7 this can result in an overcorrection, if the γ-ray absorption in the filter is not taken into account. It has been verified that, using the proton normalization,

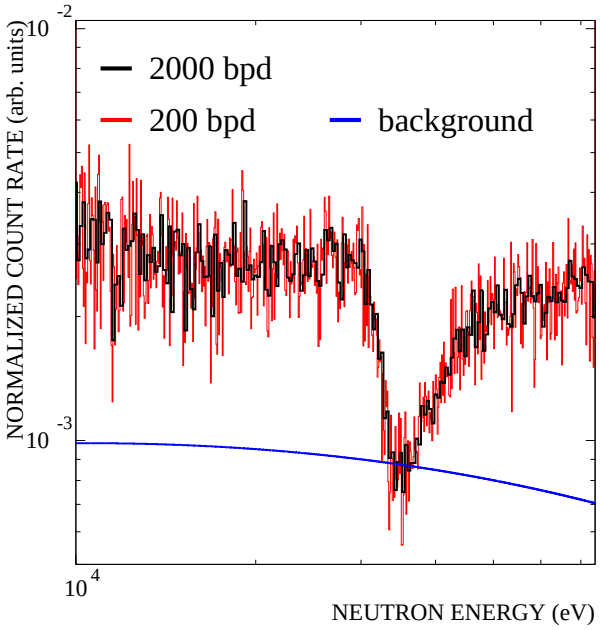

Figure 5.8: Different binning of the original TOF spectra have negligible effect on the level at the bottom of the black resonance at 34 keV. The solid line is the estimated level of background.

the background (calculated with the same procedure explained before) is matching the bottom of the black resonances, consistently to what has been found by normalizing to the silicon monitor. This check consists of two steps in evaluating the background level at the bottom of the black resonance:

1. rescaling the spectra of the osmium and gold samples with the filters in beam to match the count rate without filters (this means to correct for the overall reduction of the number of neutrons due to scattering in the filters),

2. rescaling the γ-ray background according to the γ-ray absorption in the filters (as in the analysis using the other normalization).

Since the spectra were taken with very fine binning, the analysis is normally performed by rebinning on a coarser grid to improve the statistics. However, if the binning is too coarse to maintain the full saturation of the black resonance, the inferred background level could be too high. In figure 5.8 the adopted background level for ^{188}Os with a binning of 200 channels per energy decade is compared with the spectrum plotted on a ten times finer grid. Within counting statistics, the different binning has no impact on the background level.

5.7.4 Inelastic scattering and deuteron recoil

Inelastic scattering channels are opening at 9.75 keV for ^{187}Os and around 137 keV and 155 keV for ^{186}Os and ^{188}Os. Because of the energy threshold of 200 keV on the scintillator signals, γ-rays from inelastic scattering can contribute to the background only in the neutron energy range above this threshold value. At high neutron energies also deuteron recoils give rise to small energy depositions. Both effects were studied by increasing the threshold to 300, 500, and 1000 keV. An optimal choice for the high energy region appears to be a threshold of 500 keV.

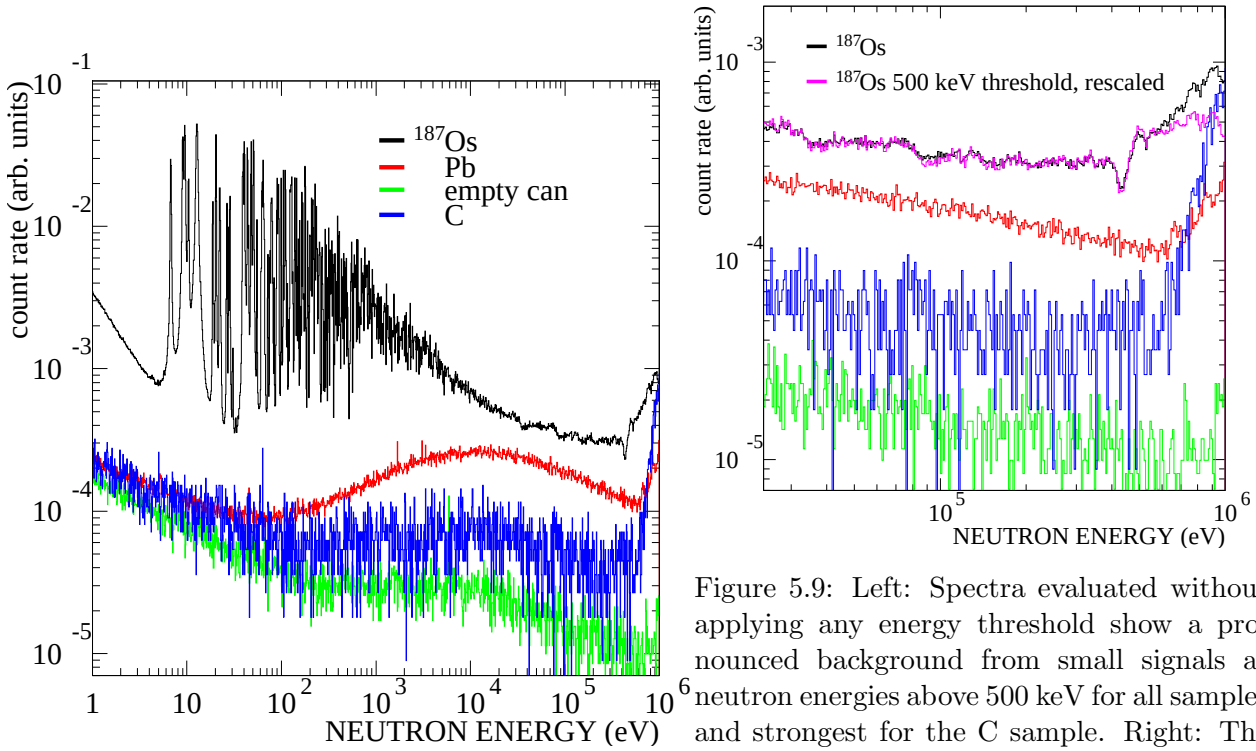

Figure 5.9: Left: Spectra evaluated without applying any energy threshold show a pronounced background from small signals at neutron energies above 500 keV for all samples and strongest for the C sample. Right: The threshold effect is emphasized by the zoom on the high energy part.

This is illustrated in figure 5.9 for the case of no threshold and the

choice for the high energy region of 500 keV. Note that the carbon spectrum is showing the strongest effect although there is no inelastic channel open (the first excited level is at 4.4 MeV for ^{12}C and 3.0 MeV for ^{13}C). This implies that most of those background events are due to deuteron recoil. This argument is supported by the fact that the carbon sample shows the largest scattering effect.

5.8 Absolute neutron flux

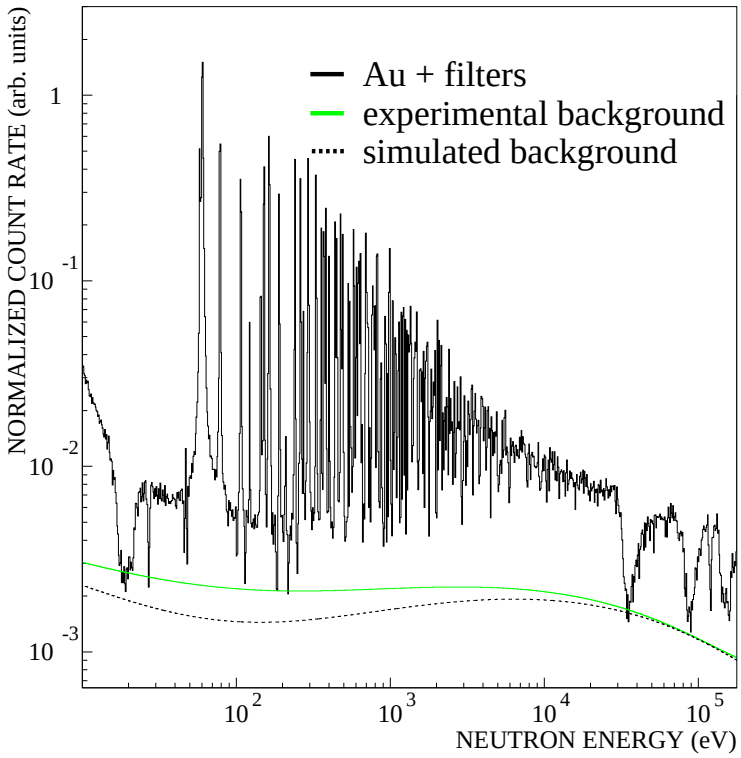

Figure 5.10: Comparison between the background level of the gold sample determined by simulations and by direct measurements. It has been found (see also the plot for ^{187}Os in figure 5.4) that the resonance at 18 eV is not completely black. In the experimental evaluation the neutron scattering component appears, therefore, overestimated.

The energy dependence of the neutron flux at n_TOF has been measured using different detectors during the commissioning of the facility. Additional data have been obtained by the ^{6}Li silicon monitor that is operated during the neutron capture campaigns and by the standard fission isotopes used in the fission campaigns. Using all this information, the energy spectrum of

the flux has been accurately defined [78, 79, 80]. The fraction of the flux that is actually impinging on the samples must be determined by the gold standard sample (of the same diameter and measured in the same position in the neutron beam as the osmium samples). Two gold standards have been used in this analysis:

1. The first gold resonance at 4.9 eV, which is especially suited to get the flux in the resolved resonance region. The absolute yield normalization is found by a fit with the R-matrix code SAMMY[90], keeping all parameters of this well known resonance fixed and using only the yield normalization factor as free parameter. The yield is defined by SAMMY as the fraction of the neutron beam that is interacting in the sample, for a saturated resonance, in which the capture channel is dominating, the yield value at the top of the resonance is close to one (see caption of figure 5.11). The background below the first gold resonance is usually negligible with respect to the capture signal.

2. The measurement of the MACS for gold at 25 keV by Ratynski and Käppeler [71] with 1.5% uncertainty is the most accurate gold cross section below the MeV region, and is often used as standard in nuclear astrophysics. In this case, the background subtraction is crucial.

The background in the gold measurement was evaluated in a similar way as for the osmium samples (see section 5.7.3). The spectra of all samples were weighted using the gold weighting function, the empty spectrum subtracted, the background from in-beam γ-rays determined by rescaling the corrected lead spectrum and the neutron scattering background by rescaling the corrected carbon spectrum. The normalization was performed via the simulations as explained before.

The reliability of the background was verified by means of the spectra taken with neutron filters as outlined in case of the osmium isotopes. Also for gold, good agreement has been obtained for the resonance at 34 keV and at 18 eV. At low neutron energies the evaluated background is in this case remarkably lower that the upper limit given by the 18 eV absorption resonance. This is due to the large capture yield from the first gold resonance at 4.9 keV that contributes to the background level at the 18 eV resonance.

A neutron flux normalization is obtained from the comparison between the experimental gold MACS at 25 keV [71] and the corresponding quasi-Maxwellian convoluted n_TOF gold spectrum. The experimental yield, renormalized in this way, shows an excellent agreement with the yield at 4.9 eV, calculated from resonance parameters in reference [74] (figure 5.11).

The absolute flux normalization was found in perfect agreement, a systematic uncertainty of 2% has been adopted for the energy dependence of the neutron flux by comparing the results from different measurements [91].

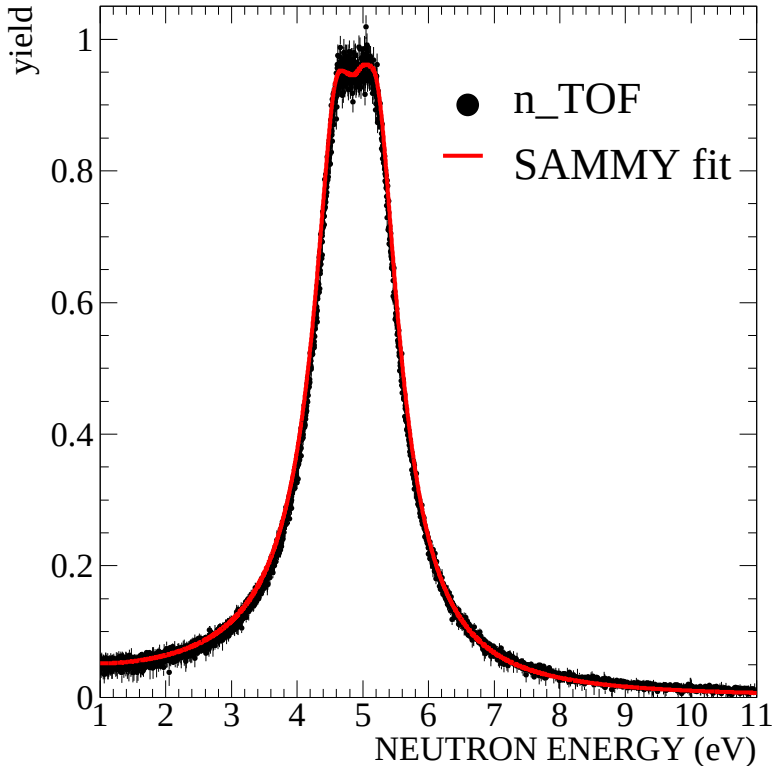

Figure 5.11: R-matrix fit of the background subtracted yield of the first resonance in ^{197}Au. The yield has been normalized to the MACS at 25 keV [71]. The expected yield at 4.9 eV of 0.973 ± 0.010 [86] using the resonance parameters of reference [74] is perfectly reproduced by the fit, which gives a yield of 0.971 ± 0.019.

5.9 Resonance analysis

Resonances in osmium were already analysed in previous experiments up to a few keV (3 keV for ^{186}Os, 2 keV for ^{187}Os, and 5 keV for ^{188}Os). The n_TOF resolution allows to enlarge the range towards higher energies and this analysis is still in progress at INFN Trieste [92]. The analysis of the resonances is fundamental in order to define the statistical average properties of the nuclei such as the level density and the transmission factors. In the present work, these results are important also for the isotopic correction, because so far the cross sections for the whole set of osmium isotopes are available only from 1 keV onward [15].

The analysis of the resonances has been performed using the R-matrix code SAMMY [90]. In order to study the effect of the background in the analysis of the resolved resonance region, the background was treated in two

different ways. On one hand, an analysis was made fitting the underlying background level at each resonance with SAMMY. On the other hand, the background evaluated as previously explained was subtracted before fitting. Both analyses were in good agreement, thus validating again the background subtraction implemented in the analysis. It is worth to be mentioned that in these two analysis the flux normalization was performed differently: for the data without background subtraction, the normalization was obtained by a fit of the first gold resonance (where the background is negligible), while the background subtracted data were normalized to the 25 keV averaged cross section of Ratynski and Käppeler [71]. The completely equivalence between the two flux evaluations was confirmed also in this analysis.

5.10 Other corrections and summary of the uncertainties

In the unresolved region, neutron multiple scattering and self shielding corrections in the sample have been determined using the code SESH [93]. This code is considered to be applicable from around 5 keV to 500 keV. In the resolved resonance region these corrections were included in the SAMMY analysis. The result form the continuum and the resonance analysis are converging already at 1.5 - 3 keV within uncertainties.

The isotopic corrections in the resolved resonance region were performed on the basis of the respective resonance assignments.

Source of uncertainty		uncertainty (%)
PHWT		2.0
Neutron flux		2.0
Background correction	^{186}Os/^{187}Os/^{188}Os	2.0/1.0/3.0
Isotopic correction	^{186}Os/^{187}Os/^{188}Os	1.5/0.7/0.7
Total	^{186}Os/^{187}Os/^{188}Os	3.7/3.1/4.2

Table 5.4: Summary of systematics uncertainties for the MACS.

In the unresolved region, isotopic corrections have to be applied by subtracting the contributions from the contaminants at all energies. Also the application of the PHWT has to be taken into account in the isotopic correction, as it is implying a wrong weighting for detection of the capture events of contaminants. This correction was determined by multiplication of the cross section of the contaminants with the ratio of the neutron separation energies of the main isotope and of the contaminants (details are reported in appendix). The code for isotopic corrections has been validated by tests with cross sections from a database, which were artificially contaminated with several impurities. For the osmium isotopes not measured at n_TOF,

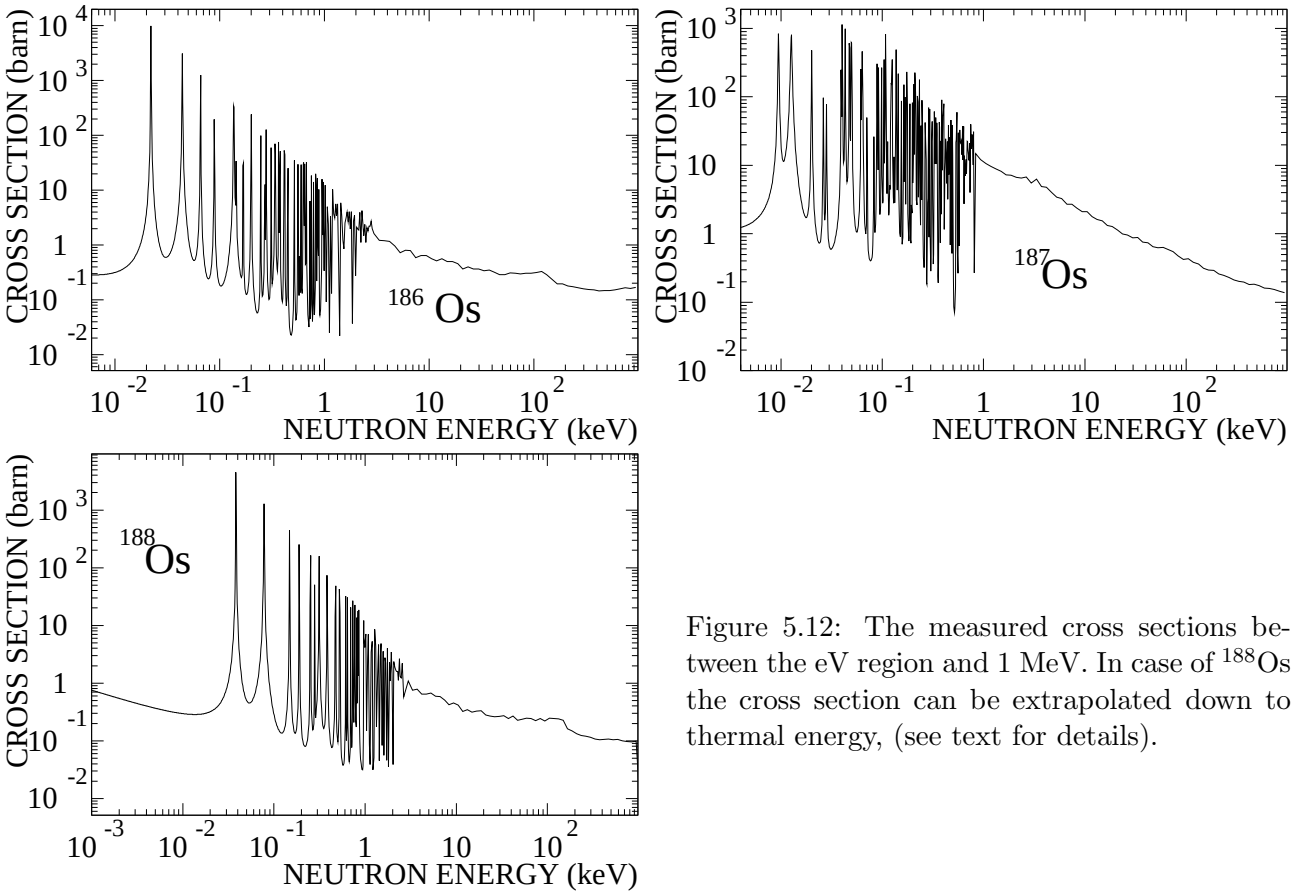

Figure 5.12: The measured cross sections between the eV region and 1 MeV. In case of ^{188}Os the cross section can be extrapolated down to thermal energy, (see text for details).

the results of Browne and Berman [15] were used as reference. These data were extrapolated beyond 135 keV using a $1/v$ trend. For ^{189}Os the cross section of Winters *at al.* [94] was used instead, as a recent measurement in a smaller range [95] resulted to be in agreement with the latter. The systematic uncertainties due to isotopic corrections have been estimated by varying the unmeasured cross section within uncertainties. Note that the cross sections of ^{190}Os and ^{192}Os are small and have, therefore, very little impact on the correction. In average, the isotopic corrections were 1.5%, 0.7%, and 0.7% for ^{186}Os, ^{187}Os, and ^{188}Os, respectively. The systematic uncertainties discussed in the previous sections are summarized in table 5.4.

5.11 Cross section results and Maxwellian averages

The cross sections have been determined in the energy range from a few eV to 1 MeV with the resolved resonance region ranging up to 3 keV, 2 keV,

and 5 keV for ^{186}Os, ^{187}Os, and ^{188}Os, respectively. The final cross sections

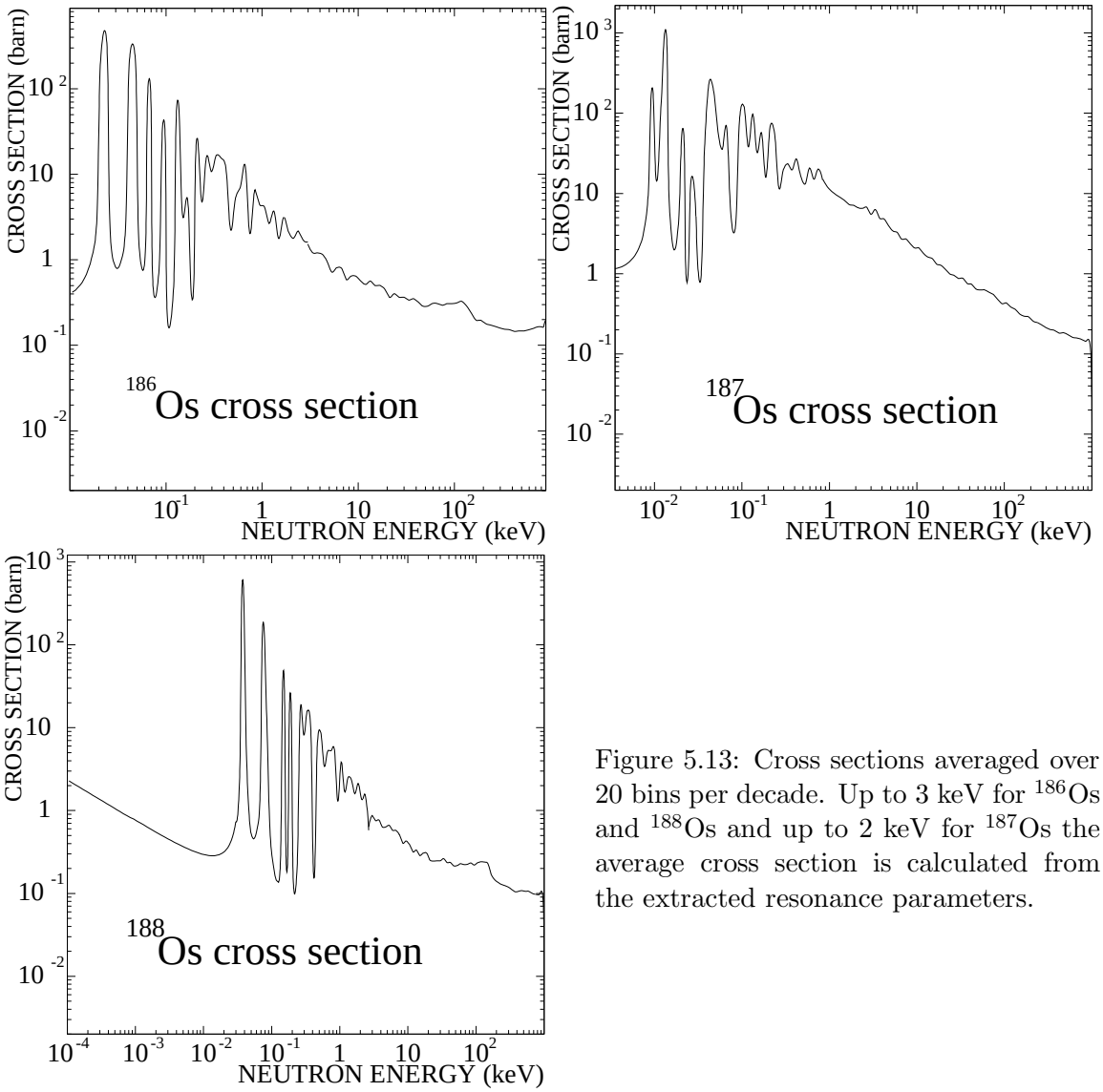

Figure 5.13: Cross sections averaged over 20 bins per decade. Up to 3 keV for ^{186}Os and ^{188}Os and up to 2 keV for ^{187}Os the average cross section is calculated from the extracted resonance parameters.

are defined over different ranges for the three osmium isotopes according to the different resonance behaviour and contaminants. In case of ^{188}Os, the absence of resonances below 0.7 eV, the energy limit of the present measurement, can be used to check the reliability of the resonance analysis. Extrapolation of the tails of the s-wave resonances down to thermal energy accounts for 56% of the thermal cross section. The remaining part is mainly due to direct capture and fits well our data with the proper $1/v$ behaviour. For ^{186}Os and ^{187}Os strong resonances in contaminants are limiting the cross section results to the region above 10 eV and 3.5 eV, respectively. The cross

sections over the entire range with full resolution are shown in figure 5.12. These data have been averaged over 20 bins per decade for the calculation of the MACS (figure 5.13 and table 5.5).

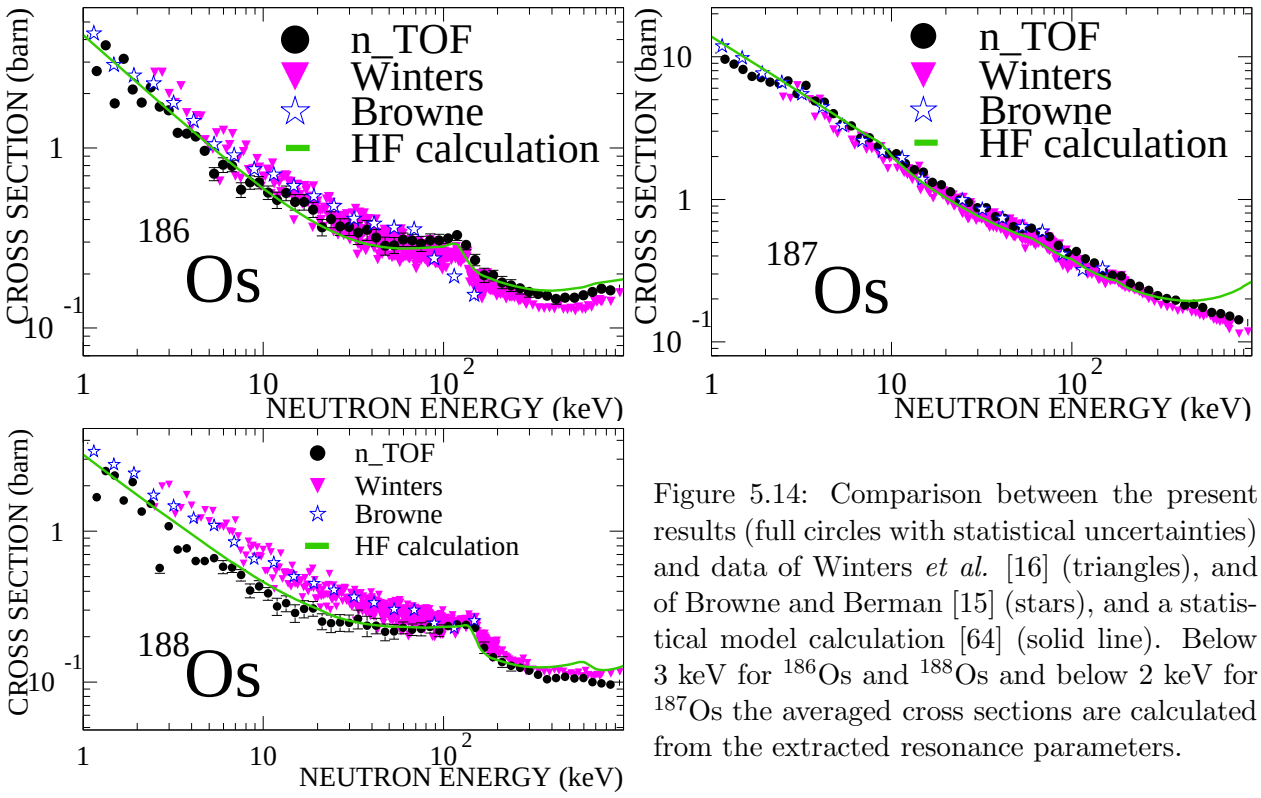

Figure 5.14: Comparison between the present results (full circles with statistical uncertainties) and data of Winters *et al.* [16] (triangles), and of Browne and Berman [15] (stars), and a statistical model calculation [64] (solid line). Below 3 keV for ^{186}Os and ^{188}Os and below 2 keV for ^{187}Os the averaged cross sections are calculated from the extracted resonance parameters.

For comparison with previous results [16, 15] and with the theoretical prediction performed on the basis of previous experimental data [64], the cross sections are shown from 1 keV to 1 MeV in figure 5.14. In general, there is good agreement with the theoretical predictions. In particular, the ^{186}Os and ^{188}Os cross sections exhibit a pronounced competition by the inelastic scattering channels at 137 and 155 keV, respectively. Compared to previous experiments, there is good agreement for ^{187}Os, which has the largest cross section, thus the results of these measurements appear to be particularly robust. The ^{188}Os cross section shows the largest discrepancies, probably because the WF used in the previous measurements assigned too much weight to the high energy part of the spectrum. This problem has been investigated in previous studies [96]. To reproduce the previous ^{188}Os cross section from our data would require to reduce the background in the keV region by 30%, far beyond any justifiable solution.

The MACSs have been calculated by means of equation 3.9 using averaged cross sections with a resolution of 20 bins per decade from the first resonances to 1 MeV (see figure 5.13). Below 3 keV for ^{186}Os and ^{188}Os and

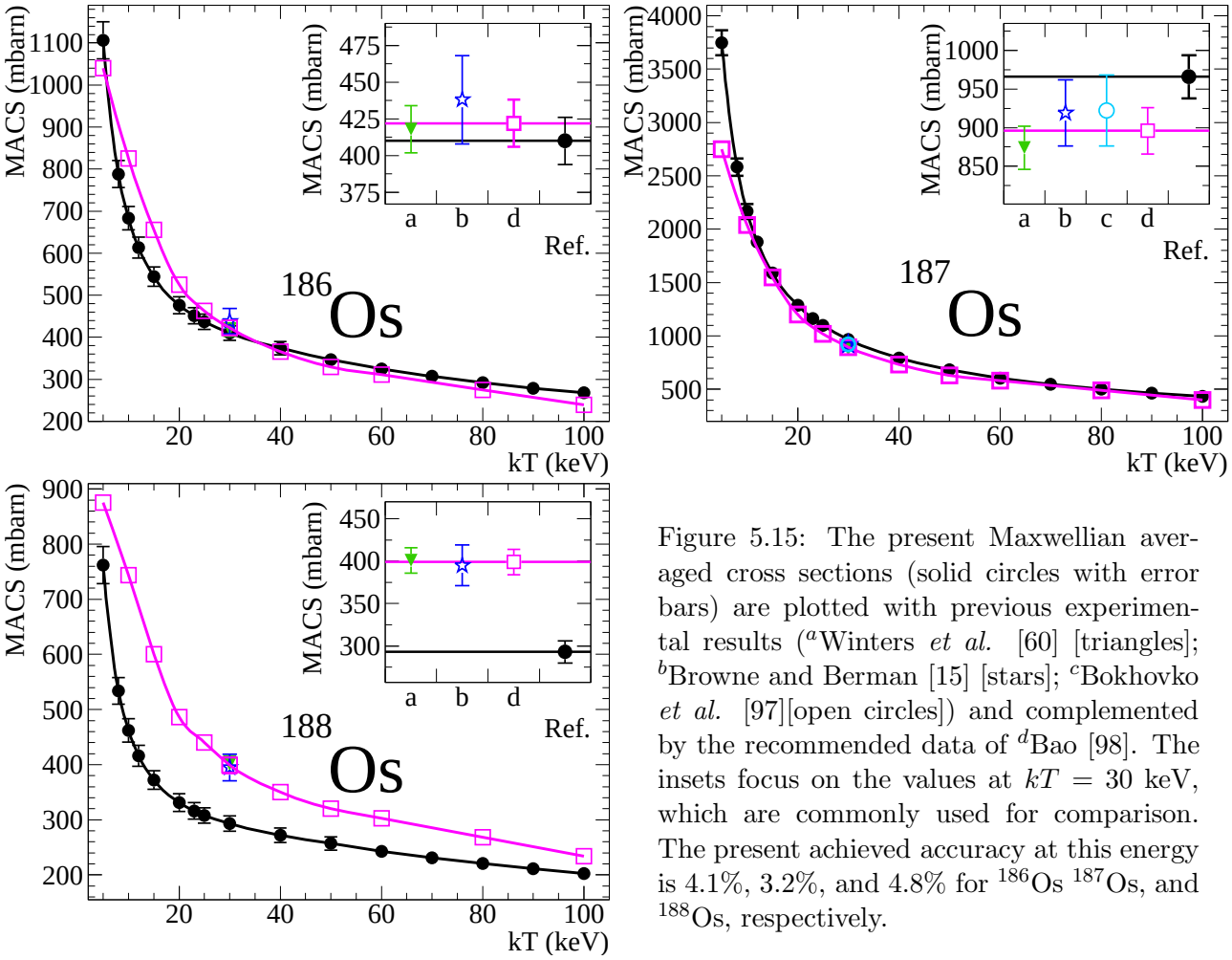

Figure 5.15: The present Maxwellian averaged cross sections (solid circles with error bars) are plotted with previous experimental results ([a]Winters *et al.* [60] [triangles]; [b]Browne and Berman [15] [stars]; [c]Bokhovko *et al.* [97][open circles]) and complemented by the recommended data of [d]Bao [98]. The insets focus on the values at $kT = 30$ keV, which are commonly used for comparison. The present achieved accuracy at this energy is 4.1%, 3.2%, and 4.8% for ^{186}Os ^{187}Os, and ^{188}Os, respectively.

2 keV for ^{187}Os the average cross sections are calculated from the extracted resonance parameters. The MACSs have been calculated for thermal energies from 5 to 100 keV (figure 5.15 and table 5.6), using for the first time a complete set of resonance parameters. The statistical uncertainties on the MACS are almost negligible, being the total uncertainty dominated by the systematic uncertainties (table 5.4).

The final uncertainties of the MACSs are between 4.0% and 4.3% for ^{186}Os, 3.1%, and 3.3% for ^{187}Os, 4.3% and 4.8 % for ^{188}Os. The MACSs for ^{186}Os and ^{188}Os deviate from previous recommended values [98], but at 30 keV the values for ^{186}Os and ^{187}Os are in agreement with previous measurements as illustrated in the insets of figure 5.15.

Energy (keV)	Range (keV)	Cross sections ^{186}Os (barn)	^{187}Os (barn)	^{188}Os (barn)
5.32	5.01-5.62	0.719±0.065	3.41±0.15	0.663±0.055
5.97	5.62-6.31	0.807±0.080	3.26±0.15	0.580±0.064
6.69	6.31-7.08	0.795±0.065	2.69±0.13	0.575±0.050
7.51	7.08-7.94	0.586±0.060	2.71±0.13	0.512±0.050
8.43	7.94-8.91	0.645±0.059	2.35±0.11	0.403±0.046
9.46	8.91-10.00	0.643±0.055	2.09±0.10	0.430±0.043
10.61	10.00-11.22	0.565±0.052	2.09±0.10	0.386±0.041
11.90	11.22-12.59	0.515±0.057	1.786±0.097	0.317±0.043
13.36	12.59-14.13	0.563±0.057	1.615±0.092	0.333±0.043
14.99	14.13-15.85	0.500±0.053	1.548±0.088	0.287±0.040
16.82	15.85-17.78	0.501±0.054	1.313±0.081	0.306±0.042
18.87	17.78-19.95	0.454±0.047	1.269±0.075	0.307±0.037
21.17	19.95-22.39	0.362±0.040	1.134±0.070	0.252±0.033
23.75	22.39-25.12	0.401±0.043	0.991±0.065	0.246±0.034
26.65	25.12-28.18	0.365±0.042	0.954±0.062	0.248±0.033
29.90	28.18-31.62	0.364±0.041	0.873±0.061	0.247±0.033
33.55	31.62-35.48	0.338±0.048	0.876±0.069	0.262±0.039
37.65	35.48-39.81	0.351±0.047	0.754±0.061	0.236±0.038
42.24	39.81-44.67	0.318±0.037	0.737±0.054	0.236±0.030
47.39	44.67-50.12	0.286±0.034	0.644±0.049	0.215±0.029
53.18	50.12-56.23	0.288±0.031	0.626±0.045	0.217±0.026
59.67	56.23-63.10	0.310±0.029	0.628±0.042	0.229±0.023
66.95	63.10-70.79	0.307±0.026	0.586±0.039	0.222±0.021
75.11	70.79-79.43	0.294±0.030	0.549±0.040	0.224±0.025
84.28	79.43-89.13	0.307±0.028	0.475±0.036	0.233±0.023
94.56	89.13-100.00	0.307±0.028	0.422±0.034	0.220±0.022
106.10	100.00-112.20	0.314±0.023	0.430±0.030	0.235±0.019
119.04	112.20-125.89	0.327±0.024	0.384±0.031	0.241±0.019
133.57	125.89-141.25	0.290±0.021	0.359±0.026	0.239±0.018
149.87	141.25-158.49	0.239±0.020	0.314±0.026	0.229±0.018
168.16	158.49-177.83	0.197±0.019	0.295±0.024	0.169±0.016
188.68	177.83-199.53	0.196±0.015	0.290±0.020	0.146±0.012
211.70	199.53-223.87	0.179±0.016	0.257±0.021	0.136±0.012
237.53	223.87-251.19	0.172±0.014	0.246±0.018	0.128±0.011
266.52	251.19-281.84	0.166±0.013	0.230±0.016	0.124±0.010
299.04	281.84-316.23	0.159±0.012	0.212±0.015	0.1191±0.0098
335.52	316.23-354.81	0.154±0.011	0.201±0.014	0.1119±0.0087
376.46	354.81-398.11	0.152±0.010	0.196±0.014	0.1046±0.0077
422.40	398.11-446.68	0.145±0.011	0.182±0.014	0.1060±0.0086
473.94	446.68-501.19	0.1476±0.0095	0.184±0.012	0.1083±0.0075
531.76	501.19-562.34	0.1473±0.0085	0.174±0.011	0.1057±0.0065
596.65	562.34-630.96	0.1523±0.0085	0.161±0.010	0.1061±0.0067
669.46	630.96-707.95	0.1582±0.0087	0.1582±0.0096	0.1001±0.0063
751.14	707.95-794.33	0.1651±0.0090	0.1524±0.0093	0.0978±0.0064
842.79	794.33-891.25	0.1615±0.0088	0.1435±0.0091	0.0962±0.0061
945.62	891.25-1000.00	0.1676±0.0088	0.1373±0.0092	0.0988±0.0061

Table 5.5: Cross sections in different energy bins form 5 keV (limit of SESH reliability). The quoted uncertainty includes the systematic error.

Thermal energy (keV)	MACS (mbarn) ^{186}Os	^{187}Os	^{188}Os
5	1106±44	3746±117	762±34
8	788±32	2582±81	534±24
10	683±28	2167±69	462±21
12	613±25	1882±60	416±19
15	544±23	1589±51	372±17
20	476±20	1286±41	331±16
23	451±19	1163±38	316±15
25	437±18	1097±36	308±14
30	410±17	966±31	293±14
40	374±16	793±26	272±13
50	347±14	683±22	257±12
60	325±13	605±20	243±11
70	307±13	546±18	231±10
80	292±12	501±17	221±10
90	279±11	465±15	211.0±9.5
100	268±11	435±14	202.6±9.1

Table 5.6: MACS for different thermal energies.

Part III

Inelastic scattering

Chapter 6

Inelastic scattering cross sections on ^{187}Os

Techniques and previous measurements

Three techniques are commonly used to measure neutron inelastic scattering cross sections, the direct detection of the inelastically scattered neutrons, the detection of the γ-rays from the de-excitation of the nucleus after the inelastic scattering (the so called $(n, n'\gamma)$ method), and by subtraction of the competing reaction channels from the total cross section. The third technique was applied once for determining the inelastic cross section for the first excited level of ^{187}Os [99], but the result is rather uncertain. The direct detection of the inelastic scattered neutrons requires monoenergetic neutron beams in the keV region, which are difficult to produce, while the second technique can be applied even with white spectra. This indirect technique appears very appealing as it has the advantage of the well established γ-detection method and allows one to measure over a wide neutron energy range [100]. This technique is limited by the excitation energy of the populated level. This is clearly the case for the 9.75 keV level in ^{187}Os because the γ-decay of this state is almost completely converted.

Consequently, the approach of detecting directly the inelastically scattered neutrons was employed for the present measurement of the inelastic scattering cross section of ^{187}Os to the first excited state at 9.75 keV.

6.1 Direct detection of inelastically scattered neutrons

This type of measurements must rely on the discrimination between elastically and inelastically scattered neutrons. For neutron energies in the keV region this is best achieved by means of the TOF technique, although neutron energy detection via proton recoils has been used as well [58, 99]. For ^{187}Os, the energy of the elastically scattered neutrons is that of the incoming beam, while inelastically scattered neutrons have lost an energy of 9.75 keV in the excitation of first level. Discrimination between neutrons with only 9.75 keV energy difference requires a narrow energy distribution for the incoming neutron beam to avoid overlap between the two neutron energy distributions.

6.2 Monoenergetic neutron beams

Monoenergetic neutron beams in the keV region can be obtained by neutron filters or by direct production of a suitable spectrum. At the astrophysically relevant energies around 20-30 keV, the ^{7}Li$(p,n)^{7}$Be reaction represents the most prolific neutron source, and is therefore to be preferred over other reactions.

6.2.1 Neutron filters

Monoenergetic neutron beams can be produced from white or thermal neutron beams by neutron filters with very deep interference minima in their total cross sections. In this way, very narrow spectra with a FWHM of a few keV can be achieved. Examples for the use of filtered beams are given in section 6.3 below.

6.2.2 ^{7}Li$(p,n)^{7}$Be reaction

The reaction kinematics of the ^{7}Li$(p,n)^{7}$Be reaction yields monoenergetic neutrons with an energy of 30 keV for proton energies directly at the 1.8811 MeV threshold of the reaction. In practice, a 30 keV neutron beam with a certain energy spread is produced because of the energy spread of the proton beam and also because the proton energy must be adjusted slightly above threshold in order to achieve sufficient neutron yield to perform the measurement. By increasing the proton energy slightly, the neutron energy distribution assumes a Gaussian-like form centered at 30 keV and the angular range of the emitted neutrons becomes larger. The neutron energy dependence on the emission angle θ and the proton energy E_p is

$$E_n(E_p,\theta) = \frac{M_p M_n}{(M_{^7\mathrm{Li}} + M_p)^2} \left\{ E_p^{\frac{1}{2}} \cos\theta \pm \left[\frac{M_{^7\mathrm{Be}} M_{^7\mathrm{Li}}}{M_p M_n}(E_p - E_{th}) - E_p \sin^2\theta \right]^{\frac{1}{2}} \right\}^2 . \quad (6.1)$$

This relation is found from the kinematics of the reaction [101]. The ± sign predicts that at every angle and proton energy two different energies are allowed for an emitted neutron. These two neutron distributions that are observed at the same angle at fixed proton energy are usually called neutron groups. Close to the reaction threshold, all neutrons are emitted in a cone with a maximum emission angle

$$\mid \theta \mid \leq \arcsin \sqrt{\frac{M_{^7\mathrm{Be}} M_{^7\mathrm{Li}}}{M_p M_n} \frac{E_p - E_{th}}{E_p}}, \quad (6.2)$$

where M are the masses of the nuclei involved in the reaction, E_p the proton energy, E_{th} the threshold energy, and θ the emission angle [101]. Although the $^7\mathrm{Li}(p,n)^7\mathrm{Be}$ reaction at threshold provides a quasi-monoenergetic 30 keV neutron beam, it was never used for measuring inelastic scattering cross sections, because of the difficulty to restrict the neutron spectrum to a FWHM smaller than 10 keV [17] and due to the small expected yield.

These two energy distributions can be separated increasing the proton energy, if the lithium target is sufficiently thin that the proton energy spread is restricted to less than a few keV and the detector subtends only few degrees. The possibility to use this feature for producing narrow energy spectra has been studied in reference [101]. However, thin lithium targets were found to be problematic because of proton energy straggling in the target, which causes an additional broadening of the spectra and prevent a clear separation of the two groups. Nevertheless, narrow neutron energy distributions have been observed above 50 keV neutron energy [17, 101, 102]. More details on the kinematics and cross sections of the $^7\mathrm{Li}(p,n)^7\mathrm{Be}$ reaction can be found in references [101, 103, 104].

6.3 Previous measurements

The inelastic scattering cross section for the first excited level of $^{187}\mathrm{Os}$ has previously been measured at different energies: A measurement by Macklin *et al.* at E_n=34 keV [56] was performed at the Oak Ridge National Laboratory using the moderated neutron source ORELA, which provides a pulsed white neutron beam [105]. The interference minimum in the total cross section of $^{56}\mathrm{Fe}$ at 24.4 keV was used as a neutron filter. The filter was coupled to the scattering detector in order to observe the 24.4 keV inelastically scattered neutrons, which were produced at the TOF corresponding

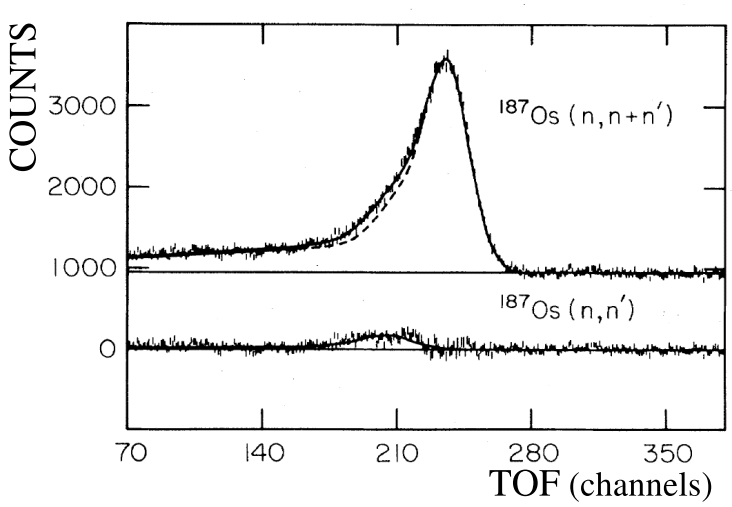

Figure 6.1: Example of a fit of the TOF spectra from a ^{187}Os sample by Hershberger *et al.* [17]. The dotted line describes the component due to elastic scattering. The lower panel shows the residual, corresponding to the inelastic component. The spectrum was obviously too broad to allow for a clear separation of the two components.

to a neutron energy of 34.4 keV. The background from elastically scattered 24.4 keV neutrons was discriminated by TOF spectra obtained with a sample of ^{188}Os in the beam, which accounts mostly for the elastic scattering component. The cross section ratio elastic/inelastic was found to be 8.3 ± 0.7, yielding an inelastic cross section of 1.5 ± 0.2 barn. Hershberger *et al.* [17] used the ^{7}Li$(p,n)^{7}$Be reaction to produce a monoenergetic beam of 60.5 keV. The energy of the neutrons was measured via TOF. A reference ^{188}Os sample was used to measure the shape of the elastic scattering and the separation between elastically and inelastically scattered neutrons was performed by fitting the TOF spectra with this reference shape and by describing the inelastic component by a Gaussian distribution (see figure 6.1). In this case, the cross section ratio elastic/inelastic was 9.4 ± 0.4 and the inelastic cross section 1.13 ± 0.2 barn.

Litvinsky [99] used a method based on a reactor generated neutron beam that was shaped with an iron filter to result in a monoenergetic neutron spectrum of 24.4 keV. Since the beam was continuous, neutron energies were determined by a proton-recoil detector. However, inelastic scattering events could not be identified due to the presence of a large γ-ray background. The inelastic scattering cross sections was therefore determined by subtraction,

$$\sigma_{inel} = \sigma_{tot} - \sigma_{el} - \sigma_{\gamma} \tag{6.3}$$

where the total cross section was measured by the transmission method and the capture cross section calculated by the evaluated parameters obtained from the total and elastic cross sections measured. The value given for the inelastic cross section was 1.04 ± 0.30 barn. In a second experiment, Litvinsky *et al.* [58] used the interference minimum of ^{52}Cr at 45 keV for filtering a continuous neutron beam from a reactor. At this higher energy, the elastic and inelastic components could be distinguished by the proton-recoil detector using the elastic response obtained in a parallel measurement of elastic scattering on lead. The resulting inelastic cross section was 1.51 ± 0.45 barn.

The uncertainties reported in these measurements are between 13% and 30%. The results of these four independent measurements are compared in figure 6.2 with a theoretical prediction based on the available information from the other reaction channels. The measurements reported in references [17, 56, 58] are in fair agreement with each other and with the calculated energy dependence, although not with the absolute value of the theoretical calculation. The result of reference [99] seems to deviate from this trend and agree better with the absolute value of the theoretical prediction. A

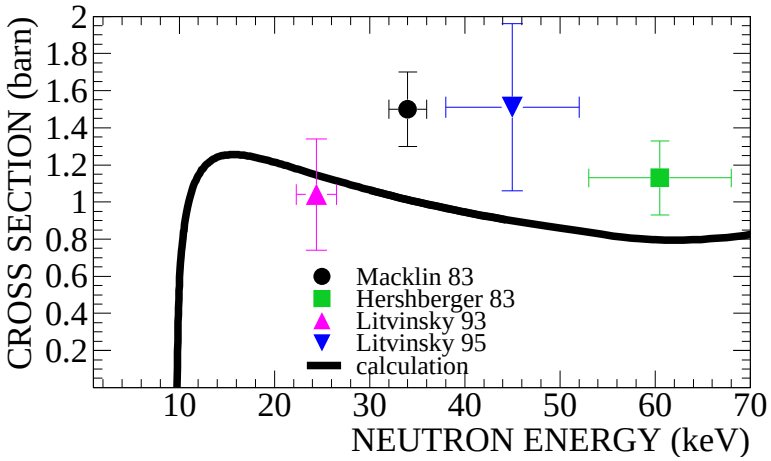

Figure 6.2: Measured inelastic scattering cross sections for the first excited state in ^{187}Os compared with a theoretical prediction [64]. Note that the energy dependence of the calculated cross section is significantly different from the trend of the experimental values.

new independent and accurate measurement would help to obtain a reliable normalization of the calculated curve. The new measurement should preferably be performed at an additional energy close to the relevant astrophysical range.

Chapter 7

Inelastic scattering cross section at 30 keV

Three previous measurements over four were performed using neutron filters. A new approach for the measurement of the inelastic channel was used in the present experiment, based on the production of a monoenergetic beam via the ^{7}Li$(p,n)^{7}$Be reaction. The measurement was performed at an energy close to the thermal energy of 23 keV, which is characteristic for the temperature in the He shell flashes in thermally pulsing AGB stars. This is the most relevant site, where the ratio ^{186}Os/^{187}Os is shaped.

The ^{7}Li$(p,n)^{7}$Be reaction as a source of monoenergetic neutrons was not completely exploited in the past because there was no attempt to make use of the properties of the reaction directly at the threshold energy. It has been shown, however, that a Gaussian-like energy distribution centered at 30 keV could be produced at the 3.7 MV Van de Graaff of Forschungszentrum Karlsruhe with a FWHM between 7 keV and 10 keV [101]. An example of such a spectrum is shown in figure 7.1. A beam with narrower neutron energy width could be produced as well, but the yield was too low to allow for a measurement with enough counting statistics. At higher energies, a spectrum centered at 52.7 keV and FWHM of 8.2 keV has been obtained (see also [106]). Similar to the beam of 60.5 keV neutrons used by Hershberger *at al.* [17], it presented a tail towards lower energies, which is inherently connected with the (p,n) reaction. Since this tail interferes with the spectrum of inelastically scattered neutrons, it presents an obstacle for accurate cross section measurements. For this reason, the neutron spectrum at 30 keV that was produced at the threshold of the ^{7}Li$(p,n)^{7}$Be reaction, was clearly preferable because it showed the best energy resolution and had the smallest neutron background at the energies, where the inelastic events are expected.

Further advantages of the 30 keV spectrum are that the energy distribution of the beam is independent of the emission angle and thus the sample can intercept all the beam. Furthermore, a Gaussian energy distribution

allows an easier fitting procedure to separate the elastic and inelastic component. The main drawback is the limited neutron yield due to the small cross section.

In the present measurement, the proton energy has been restricted to a value of 0.7 keV above threshold which represents the best compromise between the width of the neutron distribution and the neutron yield. This narrow limit of 0.7 keV above threshold is difficult to realize experimentally and requires an excellent stability of the accelerator.

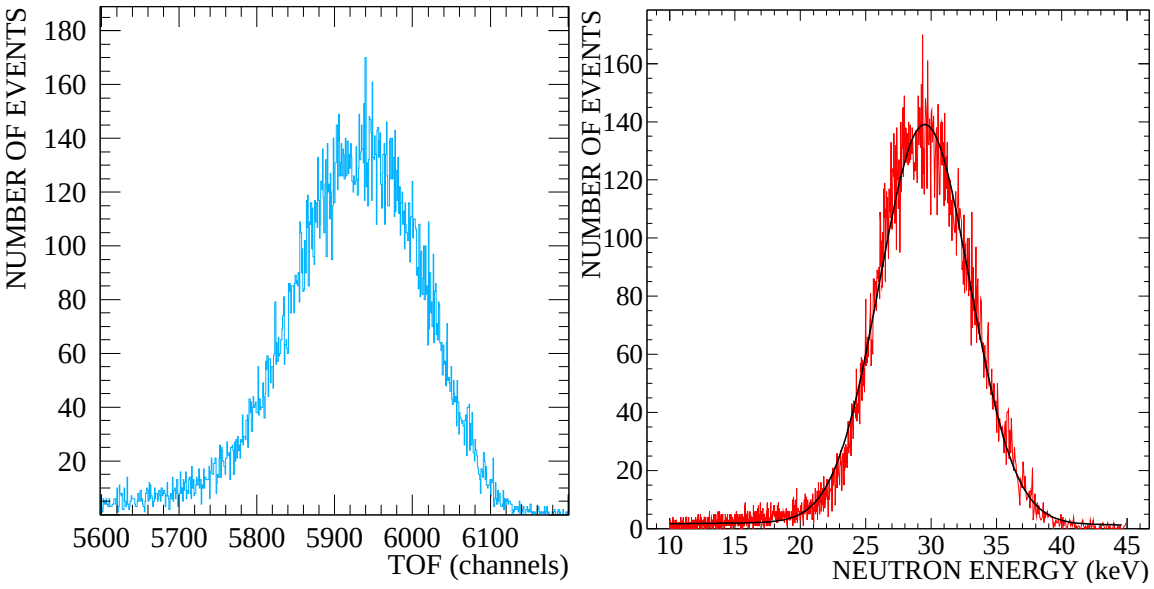

Figure 7.1: TOF spectrum (left) and the corresponding neutron energy spectrum (right) from the ^{7}Li$(p,n)^{7}$Be reaction at threshold. The energy spectrum is centered at 29.5 keV with a FWHM of 8 keV. The measurement was performed with a ^{6}Li glass detector at a flight path of 29 cm. The solid line represents a fit of the energy distribution by the superposition of two Gaussian shapes.

7.1 Neutron detectors

The choice of the neutron detector for this experiment was between a ^{6}Li loaded ZnS(Ag) scintillator that showed a very efficient n/γ-discrimination and ^{6}Li glass scintillator with a high neutron efficiency.

7.1.1 n/γ-discrimination

Standard neutron detectors for applications at keV energies are scintillators containing nuclei with large neutron cross sections such as ^{10}B and ^{6}Li.

The reaction $^6\mathrm{Li}(n,\alpha)^3\mathrm{H}$ is widely used for its large Q value of 4.8 MeV. This energy is shared between the α-particle and the triton, but the sum can be always detected in a macroscopic scintillator. In principle, the signals from neutron detection can be distinguished from those produced by γ-rays produced in (p,γ) reactions in the neutron target, which represent, in this type of measurements, the largest source of background. The background γ-rays show a wide spread of energies and usually make Compton interaction in the scintillator. As a consequence the pulses from γ-rays are shorter in time and cover a much wider pulse height interval. On the other hand, neutron induced signals should exhibit a common pulse height and a longer decay time, with respect to γ-rays induced signals.

Previous studies [101] show that the n/γ-discrimination is very efficient for ^{6}Li/ZnS(Ag) because it is rather insensitive to fast electrons. As a result of the granular texture of the scintillator, electrons can produce only small and short signals, which can be easily discriminated.

Instead, the homogeneity of the ^{6}Li glass scintillators gives rise to wide signals also for γ-ray detection, which are more difficult to distinguish from neutron induced events. Nevertheless, the fact that a neutron detection is connected with a large, constant, and localized energy deposition allows to identify a standard pulse for these events with a long decay time and similar integrated area. This feature can be used for a partial pulse shape discrimination. By recording the signals with fast digitizers (Acqiris FADC with a sampling rate of 1 ns/channels), the pulse shape discrimination was performed off-line by comparing the decay time and the integrated area of each signal.

7.1.2 ^{6}Li/ZnS(Ag) scintillators

This scintillator is available in form of compressed powder. The opacity of the material is large so that only a thickness of a fraction of a millimeter is sensitive for detection [108, 109]. In commercial detectors the volume is enlarged by folding the material and mounting it on a light guide. The Bicron detector BC702 is an example of this solution. For the present application it was found that the light guide was causing moderation, thus hampering the energy measurement via TOF. When the neutron TOF distribution from the $^7\mathrm{Li}(p,n)^7\mathrm{Be}$ reaction was compared with the one obtained from a 1 mm thick ^{6}Li glass scintillator, the distribution measured was always some keV wider for the formed detector [101]. The moderation can be avoided using the Bicron BC704 that is 1 mm thick and not folded on a light guide, but the efficiency was considerably smaller of a BC702, that was already smaller a 1 mm thick ^{6}Li glass scintillators. The problem of efficiency of the detector is crucial working with small neutron yield. Thus, the option of the large efficiency of the ^{6}Li glass scintillators was tested.

7.1.3 ^{6}Li glass scintillators

Because ^{6}Li glass scintillators are perfectly transparent, the efficiency increases with thickness. Commercially available scintillators are all enriched in ^{6}Li to 95%, but differ in the lithium concentration between 2.4% (GS2/NE902), 6.6% (GS20/NE905), and 7.5% (KG2/NE908).

The efficiency of the KG2 scintillators is much larger than that of a BC704. Therefore, this kind of detectors were chosen to perform the experiment. The scintillator thickness was limited to 3 mm in order to avoid a low energy tail in the neutron spectrum that was observed with thicker scintillators.

7.2 Beam stability

The energy stability of the Van de Graaff accelerator is typically 1 ‰. The experiment was performed at a dedicated beam line, where the object slit was located at the largest possible distance (3 m) from the analyzing magnet. In this way, the energy stability of the proton beam could be optimized without significant losses of the initial beam intensity of 2-6 μA. It was found that stable beam conditions could be maintained for several hours. Since the proton energy had to be kept within a range 0.7 keV above threshold, due to the energy spread of the proton beam a part of the beam was lost below the threshold.

The neutron energy distribution was constantly monitored and an alarm was triggered when the FWHM was exceeding the limit value of 10 keV. The FWHM of the energy distribution was measured every 2 min and was found to vary between 7.6 and 9.5 keV with stability of some hours. Furthermore, acquiring the data event by event, runs of comparable FWHM were sorted afterwards. This allowed a comprehensive analysis of the measured data.

7.3 Experimental setup

The accelerator was operated in pulsed mode with a repetition rate of 1 MHz and a pulse width of 10 ns [101]. The target consisted of a metallic layer of natural lithium 1 μm in thickness, which was evaporated onto silver backings to reduce the background from (p,γ) reactions [110]. At the reaction threshold, neutrons are emitted in a narrow cone in forward direction.

Under the conditions of the present measurements, the maximum emission angle was always below 14 deg. The monitor, which consisted of a NE908 ^{6}Li glass scintillator 3 cm in diameter and 3 mm in thickness, was placed at a distance of 1.11 m from the lithium target. Scattered neutrons were registered with three KG2 (NE908) ^{6}Li-glass detectors [111] 11 cm in

diameter and 3 mm in thickness. The scintillators, mounted on 9823QKA Thorn EMI photomultiplier tubes, were placed outside the neutron cone at a distance of 26.1 cm from the sample at angles of 90 (DET1), 120 (DET2), and 270 deg (DET4) with respect to the beam axis (see figure 7.2). The lithium target was surrounded by a lead shielding in order reduce the γ-background from the (p, γ) reactions in DET1 and DET4.

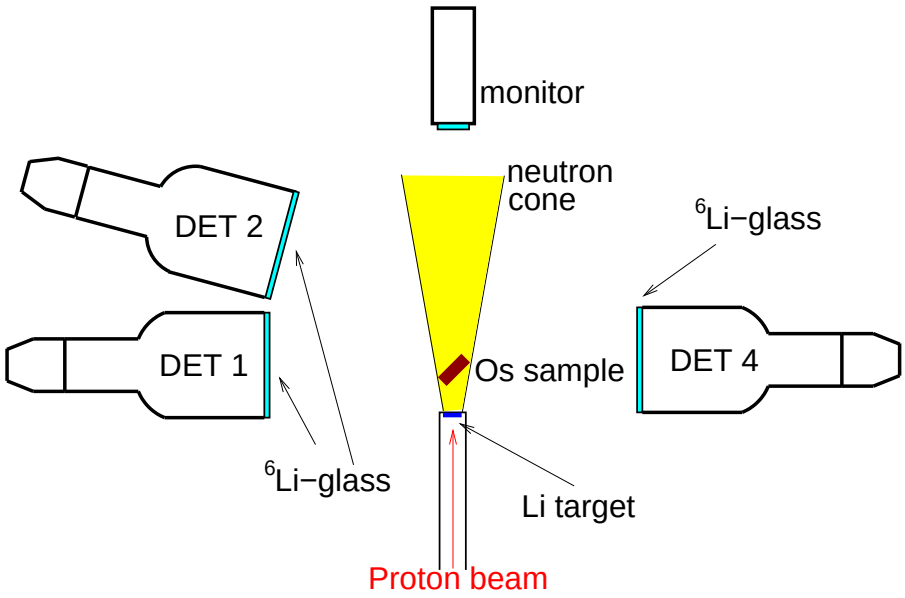

Figure 7.2: Sketch of the experimental setup (not to scale). The sample (15 mm in diameter and 1.6 mm in thickness) is mounted at a distance of 4 cm from the lithium target. The flight paths from the sample to the detectors are 26.1 cm and the neutron monitor is located 1.11 m from the target.

The ^{187}Os and ^{188}Os samples used in the experiment are the same used for the (n, γ) measurements at CERN (table 4.1). The samples were encapsulated in thin aluminum cans 15 mm in diameter and $\sim$ 1.6 mm in thickness and glued to a KAPTON© foil sustained by a carbon fiber frame, which was always outside the neutron cone. As indicated in figures 7.2 and 7.3, the samples were mounted 4 cm from the lithium target at an angle of 45 deg with respect to the proton beam. The ^{188}Os sample was measured in order to obtain the spectrum from elastic scattering. Additionally, the count rate generated by the empty can was also measured to determine the ambient background.

7.4 Data acquisition

The data acquisition system was based on FADCs to digitize the detector signals with a sampling rate of 1 ns/channel. In addition to the detector

Figure 7.3: View of the sample, which is glued onto a KAPTON© foil held by a carbon fiber frame. The lithium target is just visible inside the lead shielding. The diameter of the neutron beam at the position of the sample was 26 mm, significantly smaller than the opening in the carbon fiber frame (40 mm in diameter).

signal also the accelerator pick-up signal was recorded by the data acquisition system after conversion into a logical signal by a zero-crossing discriminator. The digitized signals were subjected to an on-line software analysis described in the next chapter.

The beam time for this measurement was slightly more than one month. The three samples (the empty can, ^{187}Os, and ^{188}Os) were alternatively measured on a one day basis in order to reduce systematic effects related with the accelerator conditions and the possible effects on the neutron beam.

Chapter 8

Analysis and results

Using an on-line analysis software, the FADC data were processed in order to determine the following information (i) the integral of the area of the signal, (ii) the n/γ discrimination parameter obtained as the ratio between the prompt and the delayed fraction of the signal, and (iii) the time between the pick-up signal from the accelerator and the registration of an event in the detector. From these data TOF spectra were produced after applying a n/γ discrimination method. The latter was adjusted for each detector by measuring its response to a neutron beam produced with a lithium target. The dependence of the discrimination parameter and integrated signal area versus the time of flight were used to optimized the discrimination thresholds. Applying these cuts, the γ-ray background was reduced by a factor of 50 (see figure 8.1).

8.1 Steps of the analysis

The inelastic cross section is determined experimentally from the ratio of the elastic to inelastic channels. In principle, the elastic component in the spectrum of ^{187}Os can be obtained from the measurement of the ^{188}Os sample, which shows only elastic scattering. Two different approaches have been applied in this work:

1. The energy dependence of the elastic scattering distribution has been considered to be identical (apart from sample related rescaling factors) for ^{187}Os and ^{188}Os. Thus, a fit of the measured scattering yield from the ^{188}Os sample can be used to describe the energy dependence of the elastic scattering for ^{187}Os. Then, the elastic and inelastic components in ^{187}Os can be separated by fitting the elastic component in the ^{187}Os spectrum [17]and in this way obtain the inelastic component by subtraction [56]. In the following this approach is labeled "comparative".

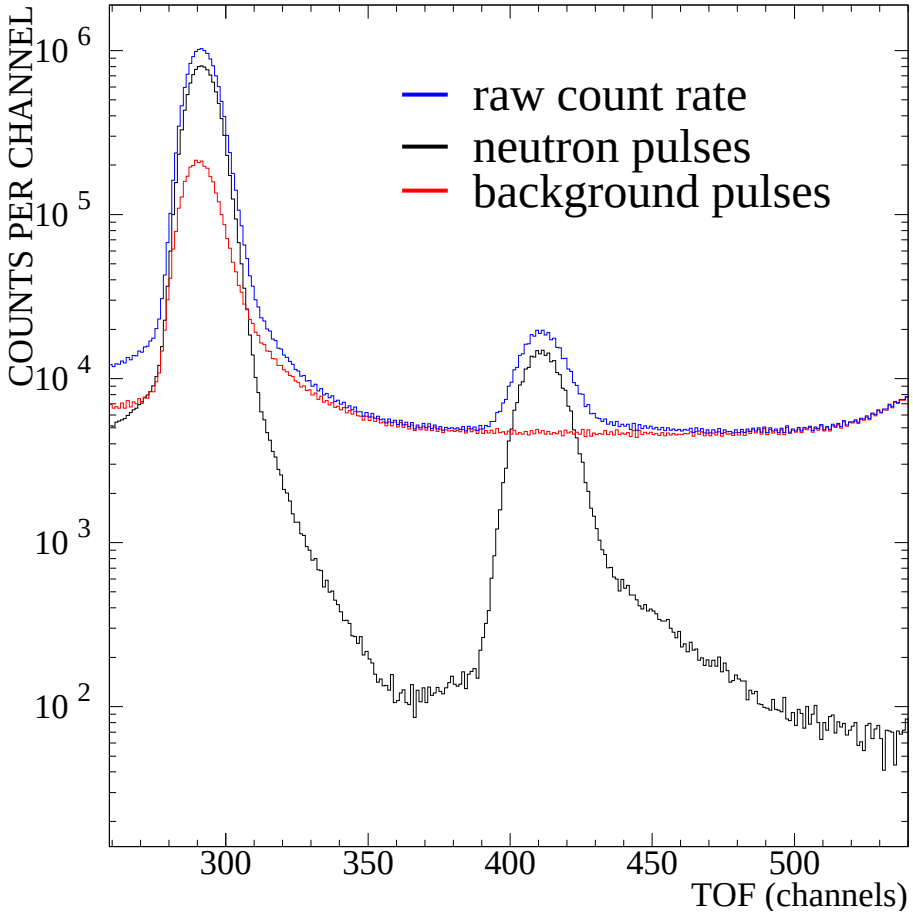

Figure 8.1: TOF spectra with and without the thresholds for pulse height and n/γ-discrimination. The peak on the left is the γ-flash, while the other peak is the neutron distribution.

2. The expected elastic scattering components from ^{187}Os and ^{188}Os are simulated with a Monte Carlo code for the complete geometry of the setup. Once the simulations have been verified to describe the measured scattering spectrum of ^{188}Os properly, the elastic component in the ^{187}Os spectrum can be determined using the same computer model of the setup and the same parameterization of the neutron beam. Moreover, the inelastic component can be treated by shifting the elastic part by the 9.75 keV of the scattering state. The ratio between the elastic and inelastic components are obtained by their relative intensities, which is considered as a free parameter in the fit. This procedure is labeled "Monte Carlo approach".

The comparison with a reference sample has been used in all previous measurements (sometimes even without fitting), but a full and detailed

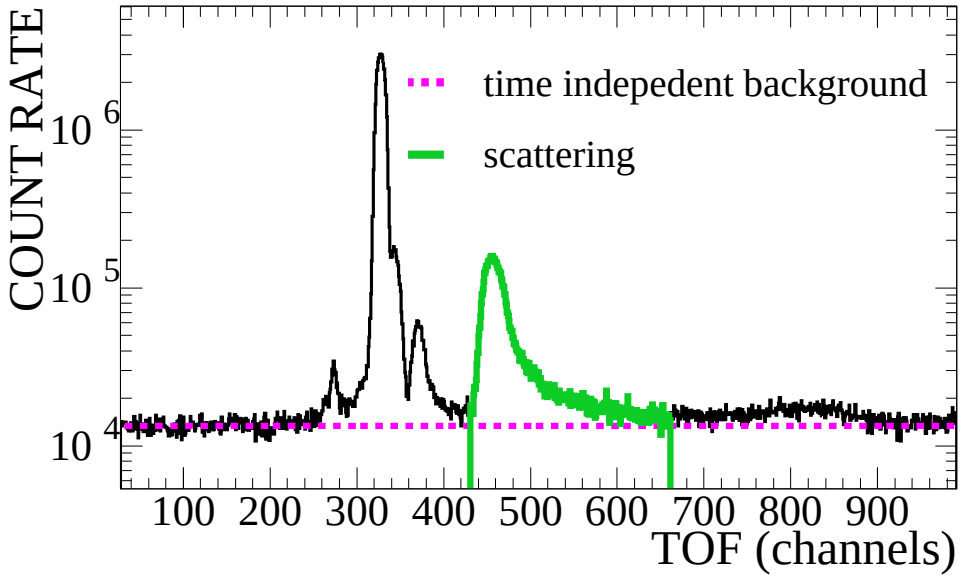

Figure 8.2: Raw TOF data of ^{187}Os taken with DET1. The linear fit of the count rate to the left of the peaks has been used to define the time-independent background. The first peak from the left is due to (p, γ) interactions in the slits of the analyzing magnet close to the lithium target. The second peak corresponds to the prompt γ flash produced when the proton pulse hits the target; this peak overlaps with γ rays from neutron captures in the sample. The next peak before the distribution produced by scattered neutrons stems from the 5.9 keV (n, γ) resonance in the aluminum of the sample can, and the feature at channel 800 is due to (n, γ) reactions in the monitor.

Monte Carlo simulation has been employed here by first time in oder to improve the uncertainties of the analysis.

The runs were sorted on the basis of the neutron beam width (FWHM) measured by the monitor detector in order to compare spectra recorded with similar resolution in neutron energy. It was found that runs with neutron energy distributions with a FWHM of 9.5 keV were available for all the three samples. Additionally, those runs were offering the best compromise between counting statistics and background discrimination. Therefore, these runs have been used for further analysis.

8.2 Background

After introducing the cuts in pulse height and in the n/γ discrimination parameter, the remaining background components in the TOF spectra are shown in figure 8.2: time independent background, (p, γ) in the slits, in the

lithium target (γ-flash), (n,γ) in the sample, and in the monitor. The time-independent background is affecting the scattering distribution the most and requires a correction of about 10%. The other background components can be discriminated by TOF or are derived from the measurement with the empty can. For example, the tail of the γ-rays from the 5.9 keV resonance of aluminum extends slightly into the scattering region. This correction has been determined by fitting this peak in the spectrum obtained with the empty can. The small bump due to neutron capture in the monitor can be subtracted in the same way.

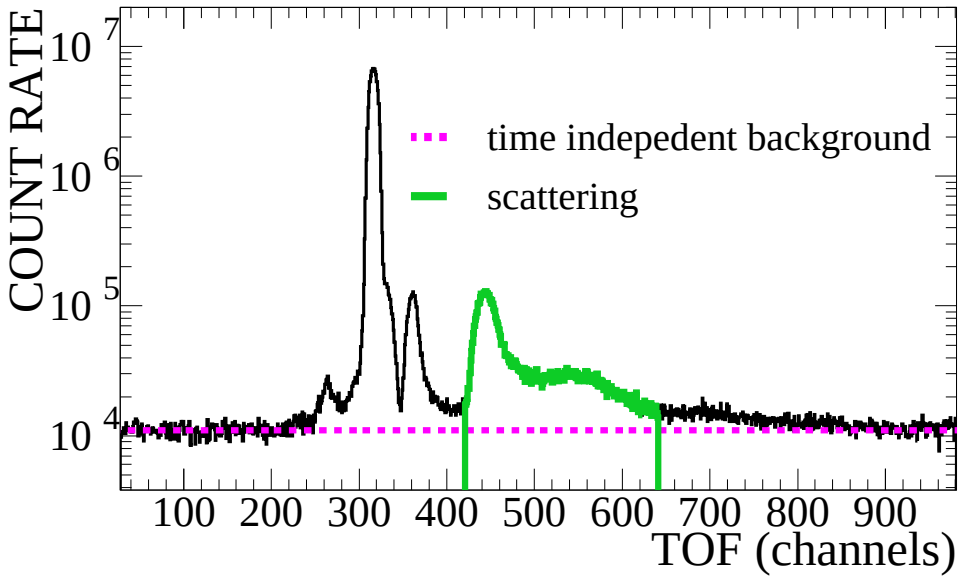

Figure 8.3: Raw TOF data of ^{187}Os taken with DET2. The broad feature on the tail of the neutron distribution is due to neutron scattering on the hydrogen contained in the glue for sealing the aluminum cans. Only DET2 shows this features for its angular position with respect to the sample. All other background components are the same as in figure 8.2. The γ-flash is larger by one order of magnitude with respect to DET1, because DET2 could not be shielded against the γ-ray emission from the target.

The comparison of the spectra of the osmium samples provides a clear indication for the inelastic part both for DET1 and DET4. However, the separation from the elastic peak is not clearly visible because of the energy resolution and large ratio of elastic to inelastic. The TOF spectrum of ^{187}Os measured with DET2 exhibits a large additional background superimposed with the inelastic component (figure 8.3). The absence of this effect in the other detectors and the fact that it was much weaker for the ^{188}Os sample indicated that this background is sample related. It has been identified to be caused by elastic scattering on hydrogen, an hypothesis that has been

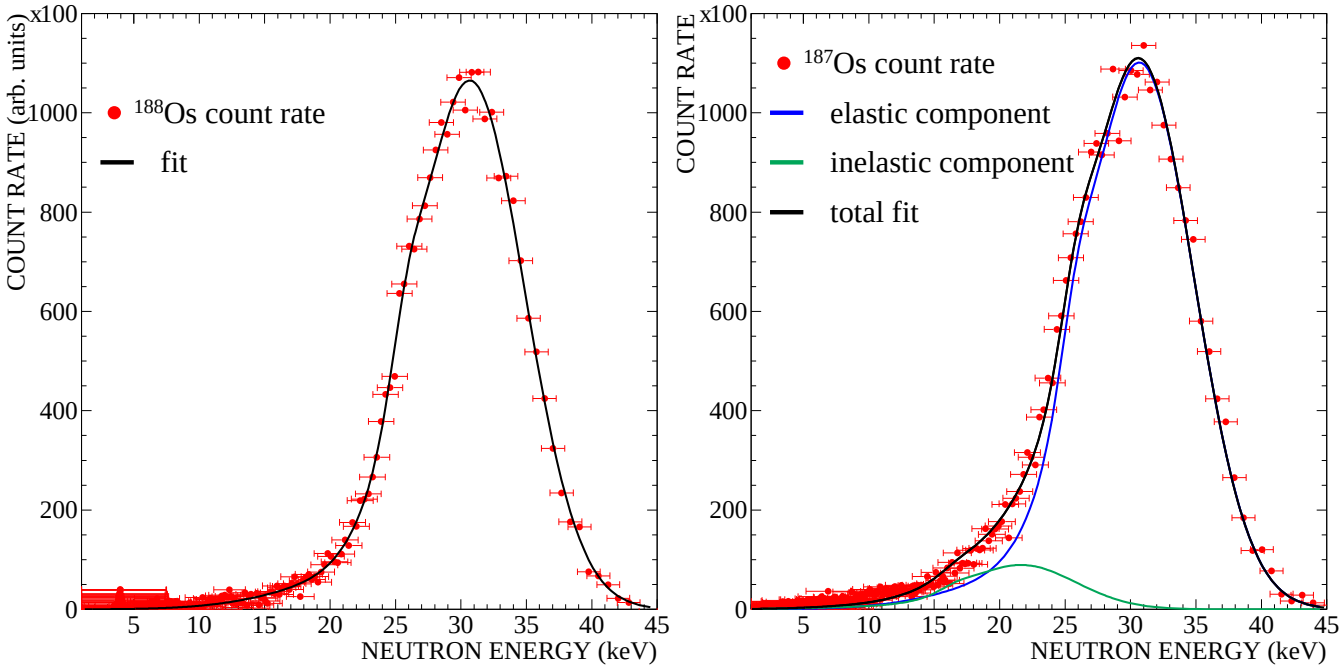

Figure 8.4: Energy spectra from DET4 for ^{188}Os and ^{187}Os. The ^{188}Os spectrum has been fitted by superposition of three Gaussian distributions to reproduce the shape of the elastic scattering yield. The shape of the inelastic distribution has been obtained by shifting the elastic component by 9.75 keV, which corresponds to the energy of the excited state. The fit of the ^{187}Os spectrum was performed by the superposition of the two distributions, assuming the respective normalization constants as the only free parameters in the fit. The shoulder around 25 keV is due to kinematics of the ^{7}Li$(p,n)^{7}$Be reaction as explained in section 8.4.

confirmed by Monte Carlo simulations (see next section). The hydrogen was present in the glue that was used to seal the aluminum cans and, according to the records from sample preparation, three times more glue was used for the ^{187}Os sample than for ^{188}Os. Since the elastic scattering cross section of hydrogen is strongly forward peaked, this background is absent in DET1 and DET4.

The uncertainty in the determination of the time independent background has been found by fitting the first part of the TOF histograms with different binnings and comparing the results. The contributions from the tail of the 5.9 keV resonance and from the (n,γ) events in the monitor have been also included. The moderation effect of the hydrogen in the glue has been estimated via Monte Carlo simulations of the experimental setup.

8.3 Comparative analysis

A first analysis was performed by using the fit of the elastic scattering in ^{188}Os for separating the inelastic component in ^{187}Os as shown in figure 8.4. In this preliminary analysis the background from the aluminum can was subtracted by rescaling the spectrum of the empty can to the 5.9 keV resonance of aluminum. The error bars shown in figure 8.4 are dominated by the uncertainty in the time to energy conversion caused by the width of the gamma flash and by the uncertainty of the flight path due to the dimensions of the detectors. The uncertainties due to background subtraction were not considered at this point. To facilitate the fit, the TOF spectra were transformed into energy spectra, where the peaks could be described by the superposition of Gaussian functions. A correction for the energy dependence of the detector efficiency due to the $^{6}\mathrm{Li}(n,\alpha)^{3}\mathrm{H}$ cross section has been implemented as well. The energy distribution of the inelastic scattering has the same shape as the elastic component, which is given by the ^{188}Os spectrum. The inelastic component is shifted by the 9.75 keV of the scattering state and corrected for the energy dependence of the inelastic scattering cross section (taken from the theoretical prediction in figure 6.2). The energy shift considered also a small correction for the neutron TOF between the lithium target and the sample. The only free parameters in the fit were the relative amplitudes of the elastic and inelastic components. While this comparative approach neglects any sample related effects, the comparison of the spectra taken with the three detectors confirmed that a further correction had to be included in the analysis of the data taken with DET 2.

The comparative analysis has been performed for DET4, providing a ratio of the elastic and inelastic components of 12.0 in the spectrum of ^{187}Os. After correcting for isotopic impurities, this translates into a cross

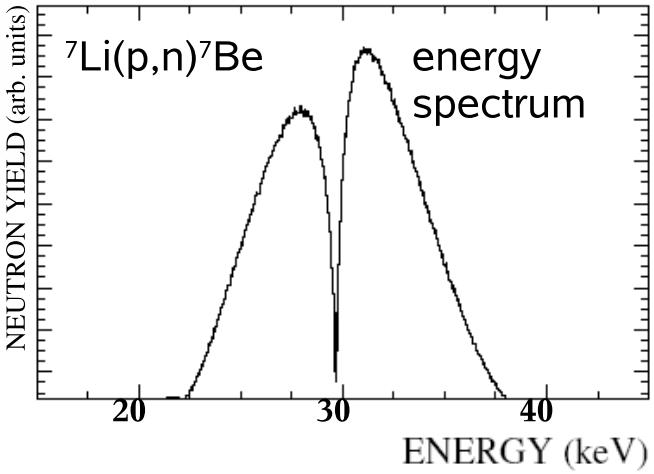

Figure 8.5: Simulated neutron energy spectrum from the $^{7}\mathrm{Li}(p,n)^{7}\mathrm{Be}$ reaction according equation 6.1. A realistic proton energy distribution was implemented, where only part of the proton beam is above threshold. The corresponding response of the ^{6}Li glass detectors to scattered neutrons is shown in figure 8.6.

section ratio for elastic and inelastic scattering of 8.4 ± 1.2.

8.4 Monte Carlo analysis

The previous analysis was based on the rather simple assumption that the final neutron energy distribution can be approximated by a combination of Gaussian distributions. However, a more realistic description of the experimental time distribution of the scattered neutrons can be obtained by means of a Monte Carlo simulations using the GEANT-MICAP simulation tool kit [112, 113, 114]. This new approach allows to account (quantitatively in the analysis) for several experimental effects, like the particular features of the samples.

The lithium target was simulated as the volume where the neutrons are generated, according to the kinematics of the $^{7}\mathrm{Li}(p,n)^{7}\mathrm{Be}$ reaction expressed by equation 6.1. The ratio between the first and second neutron energy distributions, which are centered at different energies due to the ± sign in equation 6.1, was used as a free parameter in the simulation of the spectrum of the ^{188}Os sample. The neutron distribution, that was obtained from equation 6.1 and with the assumption of a realistic proton energy distribution, is shown in figure 8.5. The simulated responses of the ^{6}Li glass detectors shown in figure 8.6 are broadened by TOF resolution.

The sample holder and the samples were simulated in all details. In particular, the amount of glue used for sealing the aluminum sample cans

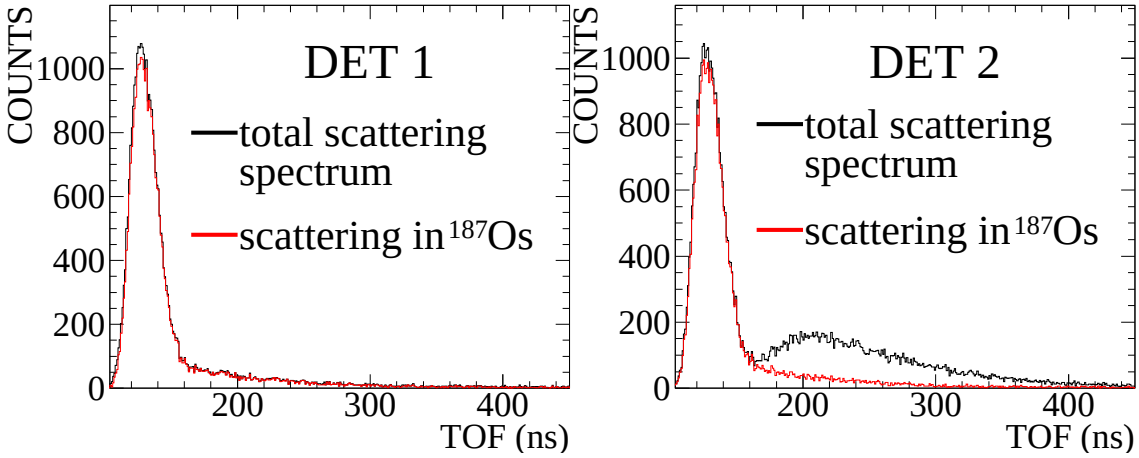

Figure 8.6: Simulated response of DET1 and DET2 to the scattered of neutrons using the neutron spectrum of figure 8.5 for the ^{187}Os sample. The background due to scattering on hydrogen (see section 8.2) is reproduced. The scattering on ^{187}Os has been separated from by the scattering on the material around the sample.

was carefully treated, since neutron scattering in the contained hydrogen is of relevance for an accurate description of the DET2 spectrum. The glue was assumed to have a composition corresponding to methyl-2-cyanoacrylate ($C_5H_5NO_2$). The isotopic composition of the osmium samples (table 4.1) and the respective total and elastic cross sections were implemented in the simulations. The detector efficiency was described via the $^6\mathrm{Li}(n,\alpha)^3\mathrm{H}$ cross section and the detector components, i.e. photomultiplier tubes, silicon oil for optical coupling, aluminum housing, and insulating tape were also modeled in detail. The simulations allow one to separate the scattering on the osmium sample from that on the materials surrounding the sample as shown in figure 8.6. In this way it was confirmed that the broad distribution in the ^{187}Os spectrum of DET2 is caused by scattering on the hydrogen contained in the relatively large amount of glue in that sample.

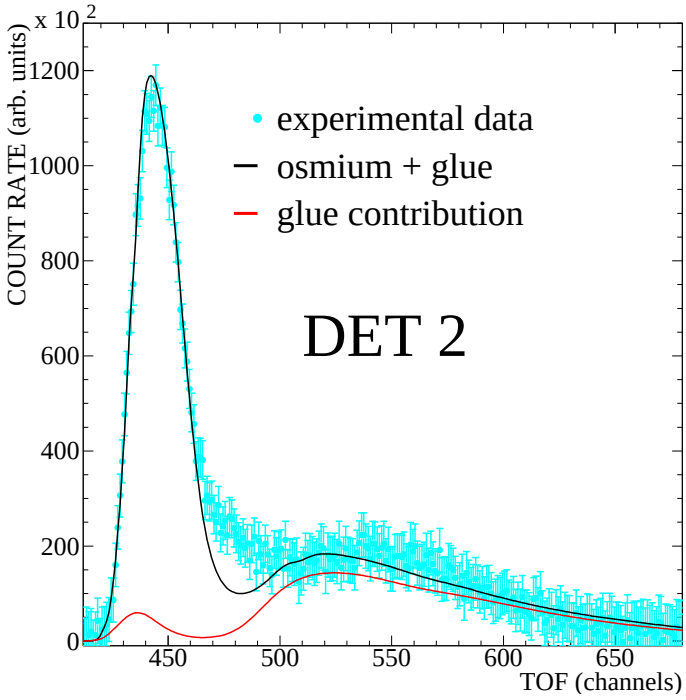

Figure 8.7: Scattering background caused by the glue for sealing the samples is shown for DET2 with 1 ns resolution for the ^{187}Os sample. The remaining differences between experiment and simulation are most likely due too the adopted composition of the glue.

Once realistic detector responses were available from the Monte Carlo study, the analysis of the measured data is similar to the procedure described in section 8.3. The first step in analyzing the data by means of the simulations was to fit the pure elastic component represented by the ^{188}Os spectrum after background subtraction. The uncertainties shown in figures 8.7, 8.8, and 8.9 are dominated by the systematic uncertainties of the background subtraction, especially due to scattering in the hydrogen and the sample holder. The uncertainties were obtained by comparison of simulations with slightly different glue distributions and different ways to evaluate the backgrounds. The best fit was obtained with a ratio of 1.25

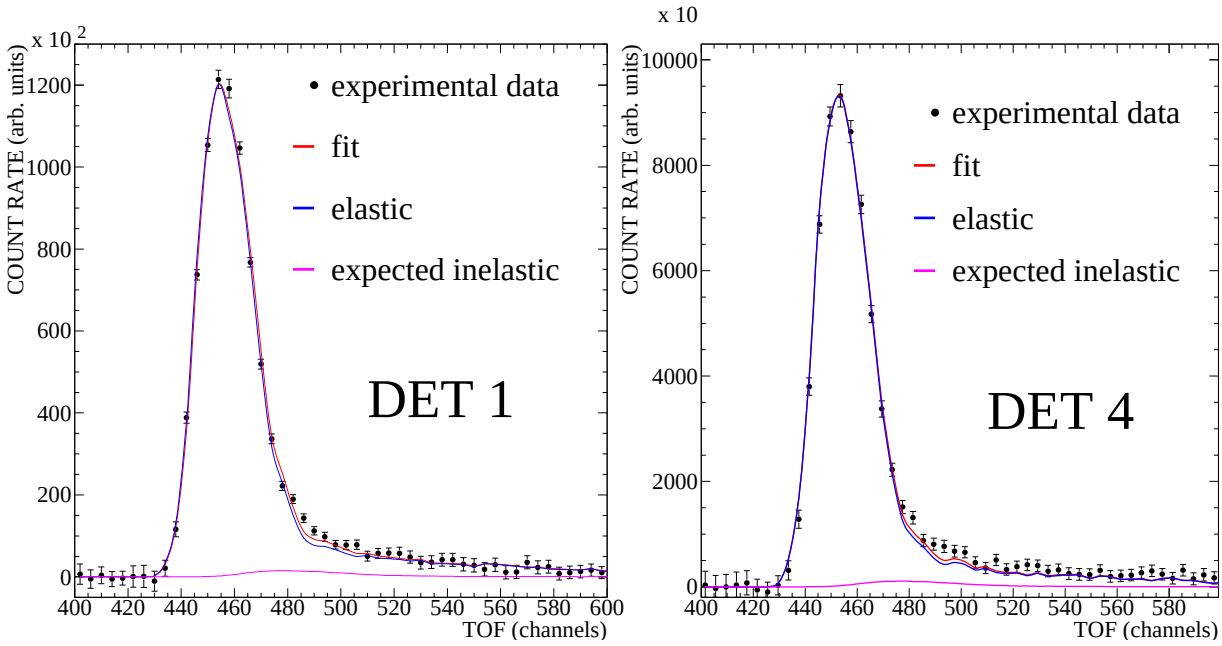

Figure 8.8: Fit of the elastic scattering distributions of ^{188}Os for DET1 and DET4 (4 ns resolution) with simulated TOF distributions. The reduced χ^2 is 1.3 for DET1 and 1.2 for DET4. The "expected inelastic" component corresponds to inelastic scattering on the ^{187}Os impurity.

for the two neutron groups of figure 8.5. The simulated spectra for elastic scattering were matching the measured ^{188}Os spectrum with a reduced χ^2 from 1.1 to 1.5, also for DET2, where a substantial correction for hydrogen background had to be considered. After fixing the parameters of the kinematics of the ^{7}Li$(p,n)^7$Be reaction, the only remaining free parameter is the normalization of the number of events in the TOF distribution.

Figure 8.7 shows the comparison between experiment and simulation for the spectrum taken with DET2 (1 ns resolution). Obviously the scattering background caused by the glue for sealing the samples is not perfectly reproduced, most likely because the real composition of the glue was different from the composition adopted for the simulations. Nevertheless, this background (that is negligible for the other detectors) is reproduced in its main features.

In view of the large background in DET2, the further analysis was restricted to the much cleaner spectra of DET1 and DET4. The simulation of the elastic peak from the ^{188}Os sample is illustrated in figure 8.8, together with the spectra measured with these two detectors. The quality of the simulated spectra is rather satisfactory and describes even the small effect of inelastic scattering on the ^{187}Os impurity in the ^{188}Os sample.

In order to analyze the inelastic component in the the ^{187}Os spectra, the elastic distribution by an energy of 9.75 keV corresponding to the scattering state. The two distributions were fixed in shape and position and the fits were performed with their relative normalization as the only free parameter. The results of the separation between the elastic and inelastic component are shown in figure 8.9. Although the inelastic contribution is considerably smaller than the elastic response, it is always producing a clear signature.

The cross section ratio for elastic and inelastic scattering of ^{187}Os has been determined to be 8.0 ± 0.1 and 8.1 ± 0.1 from the spectra taken with DET1 and DET4, respectively. These results are in perfect agreement with the ratio 8.4 ± 1.2 obtained in the comparative analysis described in section 8.3. The agreement between the two analyses confirms the validity of the

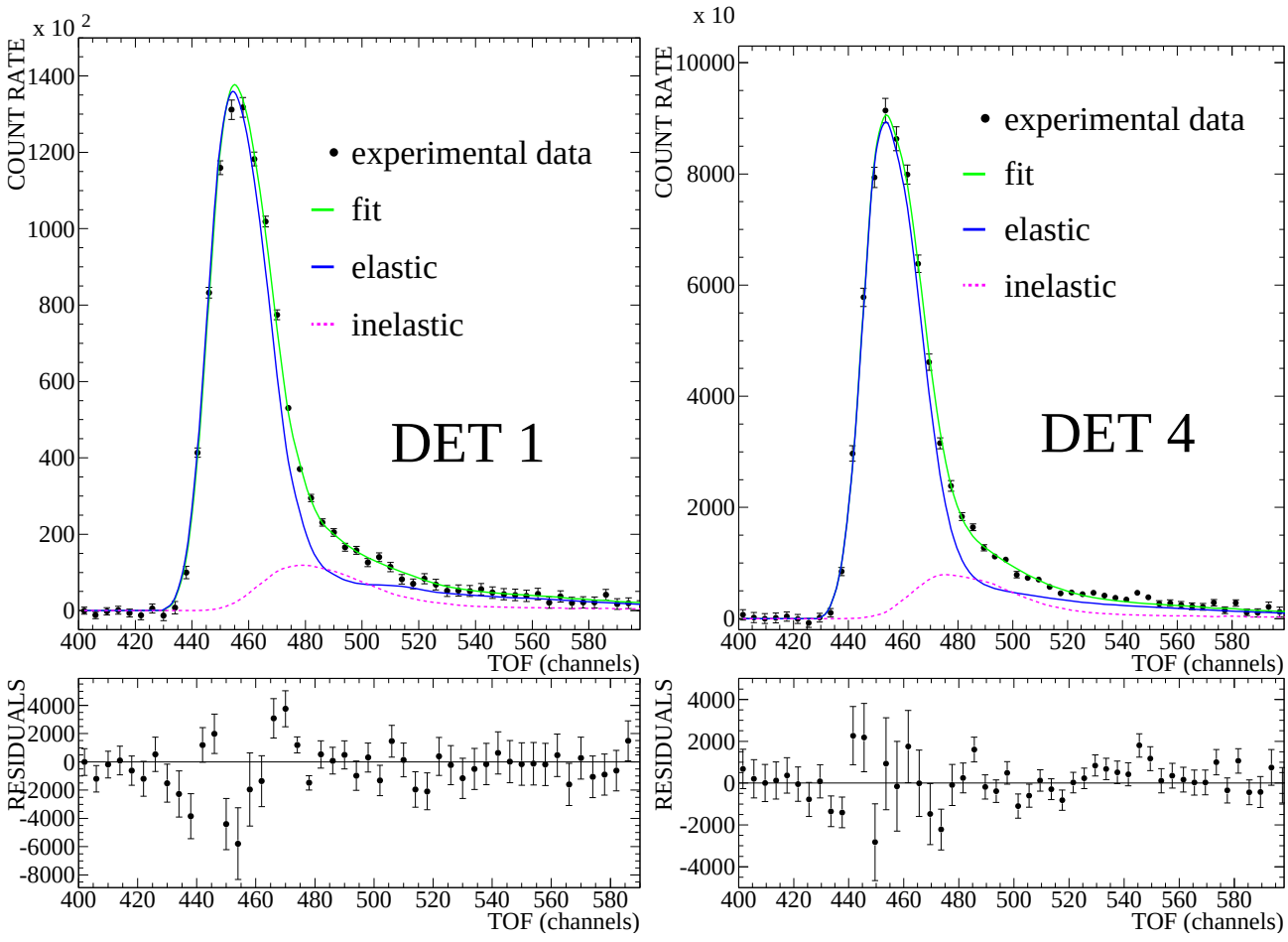

Figure 8.9: Top: The background subtracted TOF spectrum of ^{187}Os and a fit to the data (reduced $\chi^2 = 1.4$). Bottom: The residuals of the fit. The errors bars are mainly due to the systematic uncertainties resulting from background subtraction.

simulations and the negligible effect of the sample can in extracting the ratio in DET1 and DET4.

The systematic uncertainty has been obtained by comparing the results for the cross section ratio of the elastic and inelastic scattering components by varying the level of the background coming from the sample can and the KAPTON© foil of the sample holder. The background components identified in figure 8.2 are indeed small and well determined, while the background from neutrons scattered by the sample can and by the KAPTON© foil can not be observed directly, and therefore have been evaluated by a comparison of the simulated and measured spectra taken with the empty can. The corresponding uncertainty was estimated by comparing the extreme cases of i) neglecting the background from the sample can and KAPTON© foil completely and ii) increasing it by 50%. The resulting differences in the cross section ratio of the elastic and inelastic component are between 5 and 6%. An additional uncertainty of 1% was estimated for the fit procedure

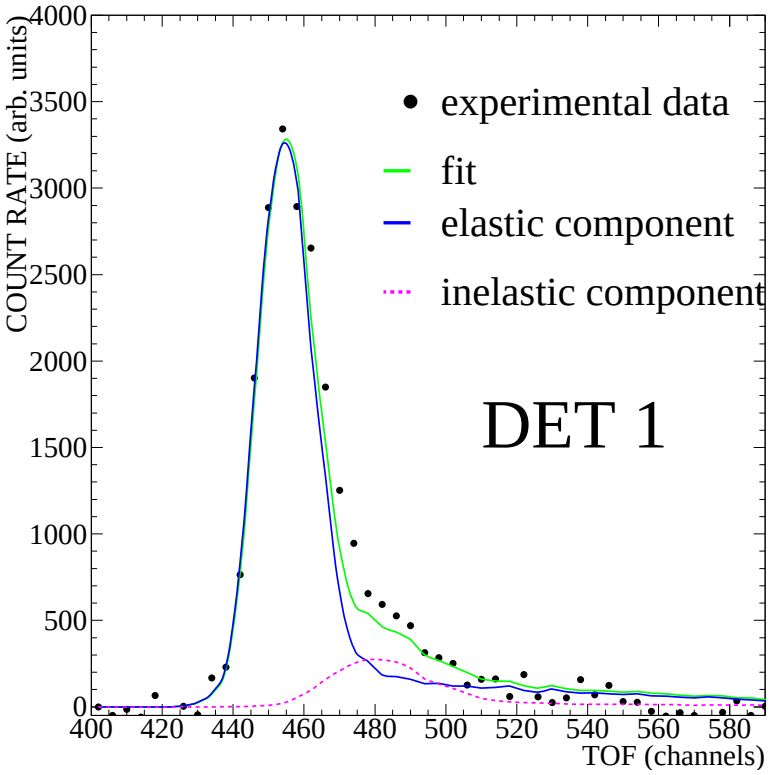

Figure 8.10: Preliminary fit of a spectrum taken with a FWHM of 7.6 keV (uncertainty not plotted for the impossibility to evaluate properly the dominant systematic contribution). The discrimination between the elastic and inelastic components is clearly improved, although a complete separation is not yet achieved.

from the difference of the results obtained with DET1 and DET4. The final ratio of the elastic and inelastic component is 8.1 ± 0.5.

8.5 Additional runs

In principle, the neutron energy spectra could be produced with FWHM as small as 7.5 keV. In the course of this experiment, neutron spectra with a sharper FWHM were also detected at the cost of lower statistics. An example is shown in figure 8.10, where the TOF spectrum of ^{187}Os was taken with a resolution of 7.6 keV FWHM. Unfortunately, this neutron energy distribution was not available for all the samples. Separation of the elastic components is clearly improved, but more difficult to analyze in view of the lack of reliable data for all the samples. The complete analysis of these spectra have been not done for this reason. Figure 8.10 has to be considered just as an example illustrating the potential of monoenergetic neutron beams from the ^{7}Li$(p,n)^{7}$Be reaction at threshold, if an improvement in the accelerator stability could be achieved. Therefore, the systematic uncertainties on the experimental points were not evaluated.

For future applications it is worth to consider the production of spectra with a FWHM smaller that 8 keV at the threshold of the ^{7}Li$(p,n)^{7}$Be reac-

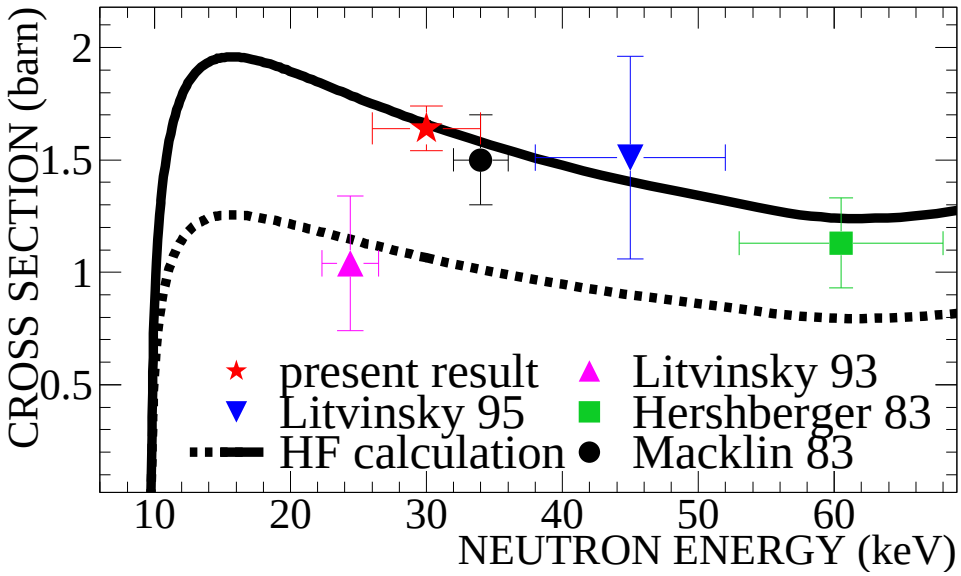

Figure 8.11: Inelastic scattering cross sections from references [17, 99, 56, 58] compared to the present result. The dotted line represents a Hauser Feshbach calculation performed without any experimental input for the inelastic parameters [64], the solid line is the same calculation rescaled to match the weighted average of all the experimental values.

tion to measure the inelastic scattering cross sections for low lying excited states in the actinide region.

8.6 Inelastic scattering cross section

The cross section ratio of the elastic and inelastic components has been determined with a neutron energy resolution of 9.5 keV FWHM and an uncertainty of 6%, in good agreement with the measurements reported in refs. [17, 56, 58]. From this ratio, the inelastic scattering cross section has been obtained by averaging previous elastic cross section data [99, 58], which yields an elastic cross section of $\sigma(n,n) = 13.27 \pm 0.30$ barns. In combination with the ratio measured in this work we find the inelastic cross section at 30 keV to be $\sigma(n,n') = 1.64 \pm 0.10$ barns.

With this value an ambiguity between the theoretically expected energy dependence and previous experimental data could be resolved as illustrated in figure 8.11, thus improving the nuclear physics input for statistical model calculations of the stellar enhancement factor for the MACS of ^{187}Os.

Distributions with a FWHM smaller than 8 keV could be achieved, which are promising with respect to further improvements, provided that these spectra can be produced with sufficient intensity. A better energy stability of the proton beam would be an important step in this direction.

Part IV

Astrophysical implications

Chapter 9

Astrophysical implications

These measurements have consequences both in the determination of the age of onset of the nucleosynthesis using the Re/Os clock and in the s-process abundance calculations. Indeed, the solar abundances of s-only nuclei as ^{186}Os must be reproduced by the models, but an overproduction of 20% is obtained also using the results from this work. The fact that these new cross sections are confirming the prediction obtained by previous results suggests that the solution of this discrepancy can not be found in the nuclear input of the models. Additionally, a recent analysis of presolar grains succeeded in reproducing the observed ratio of the abundances of ^{186}Os and ^{188}Os by using the neutron capture cross sections from this work [115].

9.1 Consequences for the clock

With the information from the (n,γ) and (n,n') measurements, a complete and consistent parameter set for the Hauser Feshbach statistical model calculations of the MACS has been established for the first time. A calculation of the stellar enhancement factor (SEF) on the basis of these data was performed and yields a SEF value of 1.25 for a thermal energy of kT= 30 keV with a conservative uncertainty of 4% [98]. With the SEF corrected stellar MACS for ^{186}Os and ^{187}Os and the isotopic abundances from [32] equation 2.10 yields

$$\frac{[^{187}\mathrm{Os}_c]}{[^{187}\mathrm{Re}]} = 0.1259 \pm 0.0091.$$

This ratio can then be used to estimate the galactic age using the schematic exponential supernova rate expressed by equation 2.11, where the ^{187}Re half life from [14] is used. In this approximation, the age of the Galaxy prior the formation of the solar system is

$$10.6 \pm 1.4 \text{ Gyr}.$$

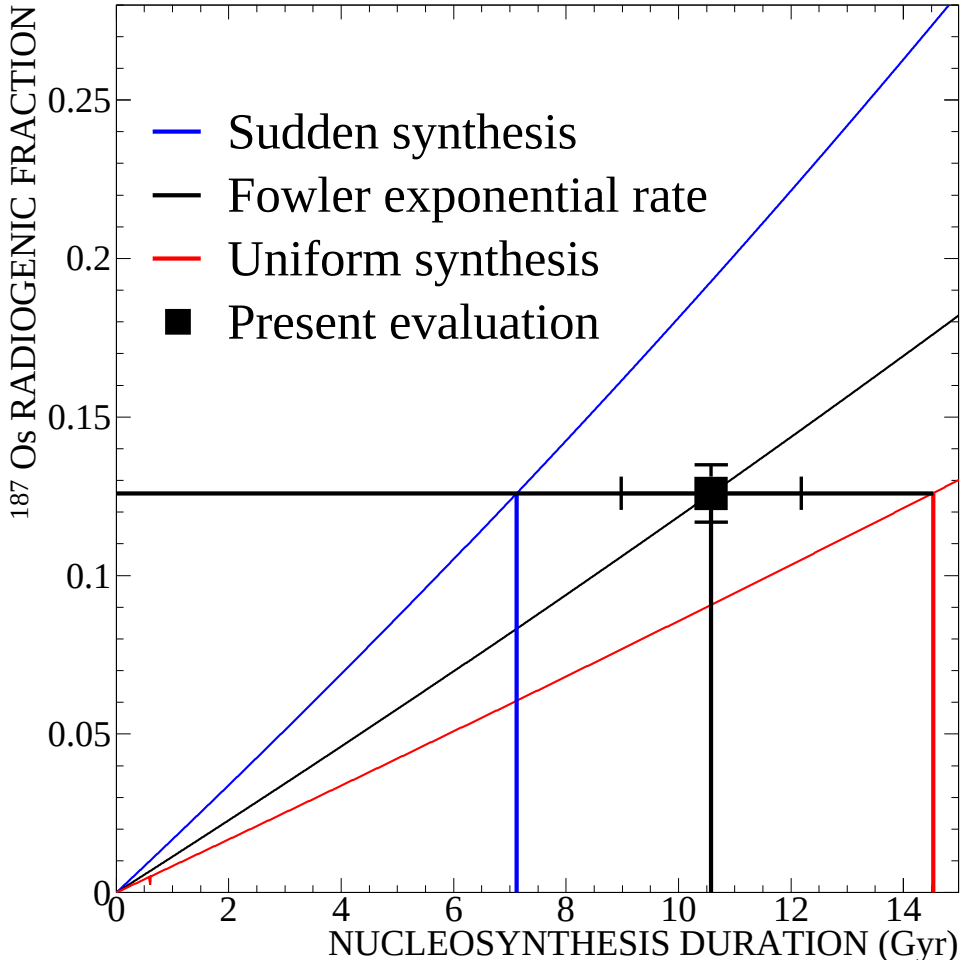

Figure 9.1: Relation between ^{187}Os radiogenic fraction and the age duration of the production of ^{187}Re according to equation 2.11. The time constant of the production rate Λ is $1/0.43t$ Gyr^{-1}, ∞, and 0, for exponential, sudden and uniform synthesis, respectively. The present $[^{187}\mathrm{Os}_c]/[^{187}\mathrm{Re}]$ has been applied to the exponential rate and the obtained result of 10.6 $\pm$ 1.4 Gyr is plotted in the picture. The sudden nucleosynthesis would lead a duration of 7.12 $\pm$ 0.87 Gyr and the uniform nucleosynthesis 14.5 $\pm$ 1.8 Gyr.

The propagation of the uncertainty on of the measurements leads to uncertainties of 0.8 Gyr, from which 0.2 Gyr can be attributed to the uncertainty on the calculation of the SEF. Since the Re/Os abundance ratio and the half life of ^{187}Re contribute to uncertainties of 1.0 and 0.6 Gyr, respectively, the uncertainties on the cross sections are no longer dominating the uncertainty on the final result of the age.

Allowing for a time interval of 0.5 Gyr between the Big Bang and the Galaxy formation and using the age of the solar system of 4.559 $\pm$ 0.004

Gyr we estimate an age of the universe of

$$15.6 \pm 1.4 \text{ Gyr}.$$

This schematic description does not yet include the effect of astration [116], which needs to be worked out in terms of Galactic evolution.

Compared to the alternative cosmic age, i.e. from the U/Th ratio ($14.5\ ^{+2.8}_{-2.2}$ [12]), from globular cluster analyses ($\geq$ 11.2 Gyr [21]), the age limit for white dwarfs ($\geq$ 12.1 Gyr [20]), via the Hubble constant (13.6 ± 1.5 Gyr [24]), and from analysis of the CMB (13.84 ± 0.28 Gyr or $13.8^{+2.3}_{-3.2}$ Gyr [28]), the present Re/Os age shows good agreement within the quoted uncertainties. An age closer to the WMAP age would require to assume a faster supernovae rate decrease during Galactic evolution than assumed by the schematic model of Fowler.

Appendix A

Appendix: Isotopic correction

The isotopic composition of the samples (table 4.1) requires proper correction. The use of the PHWT (section 3.1) introduces a deformation in the neutron capture events of the contaminants. This effect must be taken into account by the isotopic correction.

After the background subtraction and flux normalization the yield of the samples should be the sum of the product of the number of atoms of every isotope times the respective cross section,

$$Y(E) = \sum_i N_i \sigma_i(E).$$

The PHWT makes the efficiency of every γ-detection equal to 1, provided that the proper neutron separation energy is used. The use of the neutron separation energy of the main isotope prevents the capture cascades of the contaminants from being correctly treated. This distortion must be taken into account by the isotopic correction.

In the ideal case, the observed yield should be composed of contributions, where each isotope is weighted by its own neutron separation energy (s^j)

$$Y = \frac{\sum w_i^6}{s^6 + E_n} + \frac{\sum w_i^7}{s^7 + E_n} + \frac{\sum w_i^8}{s^8 + E_n} + \frac{\sum w_i^9}{s^9 + E_n} + \frac{\sum w_i^0}{s^0 + E_n} + \frac{\sum w_i^2}{s^2 + E_n}, \quad \text{(A.1)}$$

where w_i^j are the weighted events, 6, 7, 8, 9, 0, and 2 are the labels of the ^{186}Os, ^{187}Os, ^{188}Os, ^{189}Os, ^{190}Os, and ^{192}Os isotopes. This hypothetic identification of each contribution would lead to

$$Y = N_6\sigma_6(E_n) + N_7\sigma_7(E_n) + N_8\sigma_8(E_n) + N_9\sigma_9(E_n) + N_0\sigma_0(E_n) + N_2\sigma_2(E_n). \quad \text{(A.2)}$$

Where N_i are the numbers of nuclei of the isotopes in the sample. In practice, the responses S_i of the samples of ^{186}Os, ^{187}Os, and ^{188}Os are weighted for

the energy of the cascade of only one nucleus:

$$Y_6 = \frac{\sum w_i^6 + \sum w_i^7 + \sum w_i^8 + \sum w_i^9 + \sum w_i^0 + \sum w_i^2}{s^6 + E_n},$$

$$Y_7 = \frac{\sum w_i^6 + \sum w_i^7 + \sum w_i^8 + \sum w_i^9 + \sum w_i^0 + \sum w_i^2}{s^7 + E_n},$$

$$Y_8 = \frac{\sum w_i^6 + \sum w_i^7 + \sum w_i^8 + \sum w_i^9 + \sum w_i^0 + \sum w_i^2}{s^8 + E_n}.$$

By definition $N_j\sigma_j(E_n) = \frac{\sum_i w_i^j}{s^j + E_n}$, then

$$\frac{\sum_i w_i^j}{s^j + E_n} = \frac{\sum_i w_i^j}{s^k + E_n}\frac{s^k + E_n}{s^j + E_n} = N_j\sigma_j(E_n),$$

for instance

$$\frac{\sum_i w_i^7}{s^7 + E_n} = \frac{\sum_i w_i^7}{s^6 + E_n}\frac{s^6 + E_n}{s^7 + E_n} = N_7\sigma_7(E_n).$$

Thus,

$$\frac{\sum_i w_i^7}{s^6 + E_n} = N_7\sigma_7(E_n)\frac{s^7 + E_n}{s^6 + E_n} \tag{A.3}$$

leading to an energy dependent factor to be applied to the cross sections of the contaminants when used for isotopic correction.

For the yield from the ^{186}Os sample, for example,

$$Y_6 = \frac{\sum w_i^6 + \sum w_i^7 + \sum w_i^8 + \sum w_i^9 + \sum w_i^0 + \sum w_i^2}{s^6 + E_n} =$$

$$= N_6\sigma_6 + N_7\sigma_7\frac{s^7 + E_n}{s^6 + E_n} + N_8\sigma_8\frac{s^8 + E_n}{s^6 + E_n} + N_9\sigma_9\frac{s^9 + E_n}{s^6 + E_n} + N_0\sigma_0\frac{s^0 + E_n}{s^6 + E_n} + N_2\sigma_2\frac{s^2 + E_n}{s^6 + E_n}$$

Being $N = N_6 + N_7 + N_8 + N_9 + N_0 + N_2$, the equation above can be written in terms of atomic fractions.

$$\frac{Y_6}{N} = \frac{N_6}{N}\sigma_6 + \frac{N_7}{N}\sigma_7\frac{s^7 + E_n}{s^6 + E_n} + \frac{N_8}{N}\sigma_8\frac{s^8 + E_n}{s^6 + E_n} + \frac{N_9}{N}\sigma_9\frac{s^9 + E_n}{s^6 + E_n} + \frac{N_0}{N}\sigma_0\frac{s^0 + E_n}{s^6 + E_n} + \frac{N_2}{N}\sigma_2\frac{s^2 + E_n}{s^6 + E_n}$$

A system of three equation must be solved to get the isotopic corrected cross sections:

$$\begin{cases} \frac{Y_6}{N} - \frac{N_9}{N}\sigma_9\frac{s^9}{s^6} - \frac{N_0}{N}\sigma_0\frac{s^0}{s^6} - \frac{N_2}{N}\sigma_2\frac{s^2}{s^6} &= \frac{N_6}{N}\sigma_6 + \frac{N_7}{N}\sigma_7\frac{s^7}{s^6} + \frac{N_8}{N}\sigma_8\frac{s^8}{s^6} \\ \frac{Y_7}{N} - \frac{N_9}{N}\sigma_9\frac{s^9}{s^7} - \frac{N_0}{N}\sigma_0\frac{s^0}{s^7} - \frac{N_2}{N}\sigma_2\frac{s^2}{s^7} &= \frac{N_7}{N}\sigma_7 + \frac{N_6}{N}\sigma_6\frac{s^6}{s^7} + \frac{N_8}{N}\sigma_8\frac{s^8}{s^7} \\ \frac{Y_8}{N} - \frac{N_9}{N}\sigma_9\frac{s^9}{s^8} - \frac{N_0}{N}\sigma_0\frac{s^0}{s^8} - \frac{N_2}{N}\sigma_2\frac{s^2}{s^8} &= \frac{N_8}{N}\sigma_8 + \frac{N_6}{N}\sigma_6\frac{s^6}{s^8} + \frac{N_7}{N}\sigma_7\frac{s^8}{s^8} \end{cases} \tag{A.4}$$

The left part of the system is assembling the cross section from the isotope the are not measured at n_TOF and that are obtained by previous measurements. This is the known term of the equations (let one calls it yc_i). The cross sections in the right part are the measured ones and they must be isotopically corrected. Let us call the atomic fraction as X_{ij}, the system A.4 is then

$$\left\{ \begin{array}{lcl} yc_6 & = & X_{66}\sigma_6 + X_{67}\sigma_7\frac{s_7+en}{s_6+en} + X_{68}\sigma_8\frac{s_8+en}{s_6+en} \\ yc_7 & = & X_{76}\sigma_6\frac{s_6+en}{s_7+en} + X_{77}\sigma_7 + X_{78}\sigma_8\frac{s_8+en}{s_7+en} \\ yc_8 & = & X_{86}\sigma_6\frac{s_6+en}{s_8+en} + X_{87}\sigma_7\frac{s_7+en}{s_8+en} + X_{88}\sigma_8 \end{array} \right. \tag{A.5}$$

In matrix formalism

$$\vec{yc} = \begin{pmatrix} X_{66} & X_{67}\frac{s_7}{s_6} & X_{68}\frac{s_8}{s_6} \\ X_{76}\frac{s_6}{s_7} & X_{77} & X_{78}\frac{s_8}{s_7} \\ X_{86}\frac{s_6}{s_8} & X_{87}\frac{s_7}{s_8} & X_{88} \end{pmatrix} \vec{\sigma}$$

thus, the isotopic correction is given by

$$\vec{\sigma} = \begin{pmatrix} X_{66} & X_{67}\frac{s_7}{s_6} & X_{68}\frac{s_8}{s_6} \\ X_{76}\frac{s_6}{s_7} & X_{77} & X_{78}\frac{s_8}{s_7} \\ X_{86}\frac{s_6}{s_8} & X_{87}\frac{s_7}{s_8} & X_{88} \end{pmatrix}^{-1} \vec{yc}$$

The atomic fraction matrix is

$$\begin{pmatrix} X_{66} & X_{67} & X_{68} \\ X_{76} & X_{77} & X_{78} \\ X_{86} & X_{87} & X_{88} \end{pmatrix} = \begin{pmatrix} 0.7948 & 0.0091 & 0.0488 \\ 0.0106 & 0.7043 & 0.1273 \\ 0.00114 & 0.00117 & 0.94986 \end{pmatrix}$$

Applying the neutron separation energies from table 5.3 and considering negligible ($E_n \ll S_i$) the energy of the neutrons, the matrix of the system is

$$\begin{pmatrix} X_{66} & X_{67}\frac{s_7}{s_6} & X_{68}\frac{s_8}{s_6} \\ X_{76}\frac{s_6}{s_7} & X_{77} & X_{78}\frac{s_8}{s_7} \\ X_{86}\frac{s_6}{s_8} & X_{87}\frac{s_7}{s_8} & X_{88} \end{pmatrix} = \begin{pmatrix} 0.7948 & 0.0091\frac{7.9895615}{6.2900} & 0.0488\frac{5.92035}{6.2900} \\ 0.0106\frac{6.2900}{7.9895615} & 0.7043 & 0.1273\frac{5.92035}{7.9895615} \\ 0.00114\frac{6.2900}{5.92035} & 0.00117\frac{7.9895615}{5.92035} & 0.94986 \end{pmatrix} =$$

$$= \begin{pmatrix} 0.7948000 & 0.0115588 & 0.0459321 \\ 0.0083451 & 0.7043000 & 0.0943307 \\ 0.0012112 & 0.0015789 & 0.9498600 \end{pmatrix} = X_n$$

and its inverse

$$X_n^{-1} = \begin{pmatrix} 1.2584833 & -0.0205221 & -0.0588181 \\ -0.0146999 & 1.4204054 & -0.1403497 \\ -0.0015803 & -0.0023349 & 1.0530950 \end{pmatrix}$$

The uncertainty induced by neglecting the neutron energies has been measured as absent up to 30 keV and less than 0.2‰, 0.64‰, and 0.005‰ for ^{186}Os, ^{187}Os, and ^{188}Os, respectively. This uncertainty is completely negligible with respect to the systematic uncertainty reported in table 5.4 that are dominating the error calculations.

Bibliography

[1] Rutherford, E., *Journal of the Royal Astronomical Society of Canada*, **1**, 145 (1907).

[2] Rutherford, E., *Nature*, **123**, 313 (1929).

[3] Dalrymple, G. B., *The age of the earth*, Stanford Universtiy Press, 1991.

[4] Tilton, G. R., *Age of the solar system*, University of Arizona Press, Tucson, AZ, 1988, pp. 259–275.

[5] Frebel, A., Christlieb, N., Norris, J. E., Thom, C., Beers, T. C., and Rhee, J., *Ap. J.*, **660**, L117 (2007).

[6] Wanajo, S., Itoh, N., Ishimaru, Y., Nozawa, S., and Beers, T. C., *Ap. J.*, **577**, 853 – 865 (2002).

[7] Otsuki, K., Mathews, G. J., and Kajino, T., *N. Astron.*, **8**, 767 – 776 (2003).

[8] Cowan, J. J. *et al.*, *Ap. J.*, **572**, 861 (2002).

[9] Goriely, S., and Arould, M., *Astr. and Astrophys.*, **379**, 1113 (2001).

[10] Sneden, C., *et al.*, *Ap. J.*, **591**, 936 (2003).

[11] Schatz, H., Toenjes, R., Pfeiffer, B., B. Beers, T. C., Cowan, J. J., Hill, V., and Kratz, K. L., *Ap. J.*, **579**, 626 (2002).

[12] Dauphas, N., *Nature*, **435/30**, 1203 (2005).

[13] Dauphas, N., Rauscher, T., Marty, B., and Reisberg, L., *Nucl. Phys. A*, **719**, 287c–295c (2003).

[14] Galeazzi, M., Fontanelli, F., Gatti, F., and Vitale, S., *Phys. Rev. C*, **63**, 014302 (2000).

[15] Browne, J. C., and Berman, B. L., *Phys. Rev. C*, **23**, 1434 (1981).

[16] Winters, R. R., and Macklin, R. L., *Phys. Rev. C*, **25/1**, 25 (1982).

[17] Hershberger, R., Macklin, R., Balakrishnan, M., Hill, N., and McEllistrem, M., *Phys. Rev. C*, **28**, 2249 – 2258 (1983).

[18] Kienle, P., "Bound state beta-decay and its astrophysical relevance," in *Proceedings of the conference: Bologna 2000 structure of the nucleus at the dawn of the century*, edited by G. C. Bonsignori, M. Bruno, A. Ventura, and D. Vretenar, World Scientific, London, 2000, pp. 328–337.

[19] Ota, K., Iye, M., Kashikawa, N., Shimasaku, K., Kobayashi, M. A. R., Totani, T., Nagashima, M., Morokuma, T., Furusawa, H., Hattori, T., Matsuda, Y., Hashimoto, T., and Ouchi, M., pp. arXiv:astro–ph/0707.1561v1.

[20] Hansen, B. M. S., Richer, H. B., Fahlman, G. G., Stetson, P. B., Brewer, J., Currie, T., Gibson, B. K., Ibata, R., Rich, M. R., and Shara, M. M., *ApJS*, **155**, 551 (2004).

[21] Krauss, L., and Chaboyer, B., *Science*, **299**, 65 (2003).

[22] Freedman, W. L., *et al.*, *Ap. J.*, **553**, 47 (2001).

[23] Bennett, C. L., *et al.*, *Ap. J. Suppl.*, **148**, 1 (2003).

[24] Toery, J. L., Schmidt, B. P., Barris, B., Candia, P., Challis, P., Clocchiatti, A., Coil, A. L., Filippenko, A. V., P., Garnavich, and Hogan, C., *Ap. J.*, **594**, 1–24 (2003).

[25] Hinshaw, G., Spergel, D. N., Verde, L., Hill, R. S., Meyer, S. S., Barnes, C., Bennett, C. L., Halperin, M., Jarosik, N., Kogut, A., Komatsu, E., Limon, M., Page, L., Tucker, G. S., Weiland, J. L., Wollack, E., and Wright, E. L., *Ap. J. Suppl.*, **148**, 135 – 159 (2003).

[26] Knox, L., Chrisensen, N., and Skordis, C., *Ap. J.*, **563**, L95–L98 (2001).

[27] Page, L., Nolta, M. R., Barnes, C., Bennett, C. L., Halperin, M., Hinshaw, G., Jarosik, N., Kogut, A., Limon, M., Meyer, S. S., Peiris, H. V., Spergel, D. N., Tucker, G. S., Wollack, E., and L., W. E., *Ap. J. Suppl.*, **148**, 233 – 241 (2003).

[28] De Bernardis, F., Melchiorri, A., Verde, L., and Jimenez, R., *arXiv:0707.4170v1 [astro-ph]* (2007).

[29] Clayton, D., *Ap. J.*, **139**, 637 – 663 (1964).

[30] Lugaro, M., *Stardust from meteorites*, World Scientific, 2005.

[31] Anders, E., and Grevesse, N., *Geochim. Cosmochim. Acta*, **53**, 197 (1989).

[32] Faestermann, T., Takahashi, T., Kienle, P., and Bosch, F., "Re/Os cosmochronometry," in *Nuclear Astrophysics*, edited by M. Buballa, W. Nörenberg, and A. Wambach, J. Wirzba, GSI, Darmstadt, 1998, pp. 417 – 422.

[33] Castellani, V., *Astrofisica stellare*, Zanichelli., Bologna, 1985, in Italian.

[34] Burbidge, E., Burbidge, G., Fowler, W., and Hoyle, F., *Rev. Mod. Phys.*, **29**, 547 (1957).

[35] Kratz, K.-L., Farouqi, K., and Pfeiffer, B., *Prog. Part. Nucl. Phys.*, **59**, 147 (2007).

[36] Arnould, M., and Goriely, S., *Phys. Pep.*, **384**, 1 (2003).

[37] Merrill, P., *Science*, **115**, 484 (1952).

[38] Busso, M., Gallino, R., and Wasserburg, G., *Ann. Rev. Astron. Astrophys.*, **37**, 239 (1999).

[39] Raiteri, C., Gallino, R., Busso, M., Neuberger, D., and Käppeler, F., *Ap. J.*, **419**, 207 – 223 (1993).

[40] Limongi, M., Straniero, O., and Chieffi, A., *Ap. J. Suppl.*, **129**, 625 (2000).

[41] Clayton, D., Fowler, W., Hull, T., and Zimmerman, B., *Ann. Phys.*, **12**, 331 (1961).

[42] Clayton, D. D., *Principles of Stellar Evolution and Nucleosynthesis*, McGraw-Hill, New York, 1968.

[43] Rolfs, C. E., and S., R. W., *Cauldrons in the Cosmos. Nuclear Astrophysics*, The University of Chicago Press, Chicago, 1988.

[44] Freiburghaus, C., Rosswog, S., and Thielemann, F. K., *Ap. J.*, **516**, 381 (1999).

[45] Argast, D., Samland, M., Thielemann, F. K., and Qian, Y. Z., *Astron. Astrophys.*, **416**, 997 (2004).

[46] Arlandini, C., Käppeler, F., Wisshak, K., Gallino, R., Lugaro, M., Busso, M., and Straniero, O., *Ap. J.*, **525**, 886 – 900 (1999).

[47] Arnould, M., Takahashi, K., and Yokoi, K., *Astron. Astrophys.*, **137**, 51–57 (1984).

[48] Sonnabend, K., Mohr, P., Vogt, K., Zilges, A., Mengoni, A., Rauscher, T., Beer, H., Käppeler, F., and Gallino, R., *Ap. J.*, **583**, 506–513 (2003).

[49] Hayakawa, T., Shizuma, T., Kajino, T., Chiba, S., Shinohara, N., Nakagawa, T., and Arima, T., *Ap. J.*, **628**, 533 – 540 (2005).

[50] Woosley, S. E., and Fowler, W. A., *Ap. J.*, **233**, 411–417 (1979).

[51] Hauser, W., and Feshbach, H., *Phys. Rev.*, **78**, 366 (1952).

[52] Moldauer, P. A., *Phys. Rev C*, **11**, 426 (1975).

[53] Bosch, F., Faestermann, T., Friese, J., Heine, F., Kienle, P., Wefers, E., Zeitelhack, K., Beckert, K., Franzke, B., Klepper, O., Kozhuharov, C., Menzel, G., Moshammer, R., Nolden, F., Reich, H., Schlitt, B., Steck, M., Stöhlker, T., Winkler, T., and Takahashi, K., *Phys. Rev. Lett.*, **77**, 5190 – 5193 (1996).

[54] Takahashi, K., "The ^{187}Re - ^{187}Os cosmochronometry – the latest developments," in *Tours Symposium on Nuclear Physics III*, edited by M. Arnould, M. Lewitowicz, Y. Oganessian, M. Ohta, H. Utsunomiya, and T. Wada, AIP, New York, 1998, pp. 616 – 625.

[55] Travaglio, C., Galli, D., Gallino, R., Busso, M., Ferrini, F., and Straniero, O., *Ap. J.*, **521**, 691 (1999).

[56] Macklin, R., Winters, R., Hill, N., and Harvey, J., *Ap. J.*, **274**, 408 (1983).

[57] Litvinsky, L. L., Murzin, A. V., and Shkarupa, A. M., *Phys. At. Nucl. (translation of Yad. Fiz.)*, **56(9)**, 1161 – 1166 (1993).

[58] Litvinsky, L. L., Zhigalov, Y. A., Libman, V. A., Murzin, A. V., and Shkarupa, A. M., *Phys. At. Nucl. (translation of Yad. Fiz.)*, **58(2)**, 164 – 165 (1995).

[59] Browne, J. C., and Berman, B. L., *Nature*, **262**, 197–199 (1976).

[60] Winters, R. R., Macklin, R. L., and Halperin, J., *Phys. Rev. C*, **21**, 563–573 (1980).

[61] Mengoni, M., and Käppeler, "The Re/Os clock: open questions regarding the neutron cross sections," in *Tours symposium in nuclear physics IV*, edited by L. M. Arnould, M., AIP conference proceedings 561, 2000, pp. 72–75.

[62] Andriamonje, S. and the n_TOF collaboration, Proposal: The Re/Os clock revisited, Tech. Rep. Report CERN/INTC 2000-040, INTC/P125, CERN, Geneva, Switzerland (2000), available on: http://pceet075.cern.ch/.

[63] Rauscher, T., and Thielemann, F.-K., *Atomic Data Nucl. Data Tables*, **75**, 1 (2000).

[64] Mengoni, A. (2000), private communication.

[65] Goriely, S., "A coherent set of reaction rates for astrophysical applications based on a microscopic model of nuclear level densities," in *Nuclear Data for Science and Technology*, edited by G. Reffo, A. Ventura, and C. Grandi, Italian Physical Society, Trieste, 1997, p. 811.

[66] Firestone, R., *Table of Isotopes*, Wiley, New York, 1996.

[67] Käppeler, F., and Mengoni, A., *Nucl. Phys. A*, **777**, 291–310 (2006).

[68] Macklin, R., and Gibbons, J., *Phys. Rev.*, **159**, 1007 – 1012 (1967), includes H. Maier-Leibnitz, priv. comm. and Rau63.

[69] Abbondanno, U., and the n_TOF collaboration, *Nucl. Instr. Meth. A*, **521**, 454–467 (2004).

[70] Tain, J. L., Gunsing, F., Cano-Ott, D., Colonna, N., Domingo-Pardo, C., Gonzalez, E., Heil, M., Käppeler, F., Marrone, S., Mastinu, P., Milazzo, P. M., Papaevangelou, T., Pavlopoulos, P., Plag, R., Reifarth, R., Tagliente, G., Wisshak, K., and The n_TOF collabotation, "Accuracy of the Pulse Height Weighting Technique for capture cross section measusrements," in *Journal of nuclear science and technology/Proceedings of the international conference on nuclear data for science and technology*, edited by L. Shibata and M. Igashira, Tsukuba, Ibaraki, Japan, 2002, p. 689.

[71] Ratynski, W., and Käppeler, F., *Phys. Rev. C*, **37**, 595 – 604 (1988).

[72] National Nuclear Data Center, data available on the web page: http://www.nndc.bnl.gov/.

[73] Macklin, R., and Halperin, J., *Phys. Rev. C*, **14**, 1389 (1976).

[74] Mughabghab, S., *Atlas of Neutron Resonances*, Elsevier, New York, 2006.

[75] Mughabghab, S., *Neutron Cross Sections, Vol. 1, Part B*, Academic Press, New York, 1984.

[76] Lorusso, G., Colonna, N., Marrone, S., and the n_TOF collaboration, *Nucl. Inst. and Meth. A*, **532**, 622 – 630 (2004).

[77] Abbondanno, U. and the n_TOF collaboration, Cern n_tof facility: Performance report, Tech. rep., CERN, Geneva, Switzerland (2003), report CERN/INTC 2002-037.

[78] Borcea, C., *et al.*, *Nucl. Instr. Meth. A*, **513**, 524 (2003).

[79] Marrone, S., Mastinu, P., and the n_TOF collaboration, *Nucl. Instr. Meth. A*, **517**, 389 (2004).

[80] Gunsing, F., Private communication (2004).

[81] Plag, R., Heil, M., Käppeler, F., Pavlopoulos, P., Reifarth, R., and Wisshak, K., *Nucl. Instr. Meth. A*, **496**, 425 – 436 (2003).

[82] Marrone, S., Coincidence contribution in the (n, γ) cross section at n_TOF, Tech. rep., Università degli studi di Bari, Italy (2003), internal note Ba04/2003.

[83] Marrone, S., Private communication (2006).

[84] Aerts, G., Berthoumiex, E., Gunsing, F., and Perrot, L., Weighting functions for the neutron capture measurements performed at n_tof-cern in 2002-2003, Tech. rep., CEA/Saclay, France (2004), dAPNIA-04-106.

[85] Terlizzi, R., Private communication (2003).

[86] Domingo Pardo, C., Private communication (2007).

[87] Marrone, S. and the n_TOF collaboration, *Phys.Rev C*, **73**, 164 – 165 (2006).

[88] Terlizzi, R., and the n_TOF collaboration, *Phys. Rev. C (in press).*

[89] Abbondanno, U., and the n_TOF collaboration, Cern n_TOF facility: Thechnical report, Tech. rep., CERN, Geneva, Switzerland (2000), report CERN/INTC 2000-018.

[90] Larson, N., *Updated users' guide for SAMMY* (2003), oRNL/TM-9179/R6.

[91] Domingo Pardo, C., *New radiative neutron capture measurements of* ^{207}*Pb and* ^{209}*Bi*, Ph.D. thesis, Universidad de Valencia, 2004.

[92] Fujii, K., and the n_TOF collaboration, "Capture cross section measurements at n_TOF, the resolved resonace region," in *in press*, edited by nd2007, Nice, 2007.

[93] Fröhner, F., Report kfk–2145, Tech. rep., Kernforschungszentrum Karlsruhe (1977).

[94] Winters, R., Macklin, R., and Hershberger, R., *Astron. Astrophys.*, **171**, 9 – 15 (1987).

[95] Segawa, M., Masaki, T., Nagai, Y., Temma, Y., Shima, T., Mishima, K., Igashira, M., Goriely, S., Koning, A., and Hilaire, S., *Phys. Rev. C*, **76**, 022802–1 (2007).

[96] Sowerby, M., and Corvi, F., "Matters related to the NEANDC task froce on ^{238}U and ^{56}Fe resonances," in *Nuclear Data for Science and Technology*, IAEA, Mito, Japan, 1988, p. 37.

[97] Bokhovko, M., Kononov, V., Poletaev, E., Rabotnov, N., and Timokhov, V., in *Nuclear Data for Science and Technology*, edited by S. Qaim, Springer, Berlin, 1992, Research Reports in Physics, p. 62.

[98] Bao, Z., Beer, H., Käppeler, F., Voss, F., Wisshak, K., and Rauscher, T., *Atomic Data Nucl. Data Tables*, **76**, 70 – 154 (2000).

[99] Litvinsky, L. L., *Phys. At. Nucl. (translation of Yad. Fiz.)*, **56(1)**, 17 – 23 (1993).

[100] Mihailescu, L. C., Oláh, L., and Plompen, J. M., *Nucl. Inst. Meth. A.*, **531**, 375 (2004).

[101] Mosconi, M., *Re/Os cosmochronometer: neutron scattering in ^{187}Os at stellar energies*, Master's thesis, Università degli Studi di Torino (2002).

[102] McEllistrem, M., Winters, R., Hershberger, R., Cao, Z., Macklin, R., and Hill, N., *Phys. Rev. C*, **40**, 591 (1989).

[103] Monahan, J., "Kinematics of Neutron-Producing Reactions," in *Fast Neutron Physics, part I*, edited by J. B. Marion and F. J. L., Interscinece Publishers Inc., New York, 1960, p. 49.

[104] Gibbons, J. H., and Newson, H. W., "The ^{7}Li(p,n)^{7}Be Reaction," in *Fast Neutron Physics, part I*, edited by J. B. Marion and F. J. L., Interscinece Publishers Inc., New York, 1960, p. 133.

[105] Koehler, P., *Nucl. Instr. Meth. A*, **460**, 325 (2001).

[106] Mosconi, M., Plag, R., Heil, M., Käppeler, F., and Mengoni, A., "Quasi-monoenergetic neutron beams at E_n=30 keV," in *Eighth International Topical Meeting on Nuclear Applications and Utilization of Accelerators*, in press, 2007.

[107] Stedman, R., *Rev. Sci. Instr.*, **31**, 1156 (1960).

[108] Spowart, A. R., *Brit. J. Non-Destructive Testing*, **11**, 2–11 (1969).

[109] Spowart, A. R., *Nucl. Instr. Meth.*, **75**, 35–42 (1969).

[110] Walter, S., Private communication (2005).

[111] Saint Gobain, *Li glass scintillator* (2006), available from Saint Gobain web site: http://www.detectors.saint-gobain.com/.

[112] CERN, *GEANT. Detector Description and Simulation Tool* (1993), available from CERN web site: http://wwwinfo.cern.ch/asdoc/geant/geantall.html.

[113] Johnson, J., and Gabriel, T. A., A user's guide to micap: A monte carlo ionization chamber analysis package, Tech. rep., ORNL: Oak Ridge National Laboratory, Oak Ridge, Tennessee (1988).

[114] Zeitnitz, C., and Gabriel, T. A., ORNL: Oak Ridge National Laboratory.

[115] Reisberg, L., Dauphas, A., N.and Luguet, Pearson, D., and Gallino, R., "Large *s*-process and mirror osmium isotopic anomalies within the Murchison meteorite," in *38th Lunar and Planetary Science Conference*, League City, Texas, 2007, p. 1177.

[116] Takahashi, K., *Nucl. Phys. A*, **718**, 325c–332c (2003).

Acknowledgments

I would like to thank Prof. Dr. Johannes Blümer to have made possible my work in the Nuclear Astrophysics group and Dr. Franz Käppeler for the continuous support and help throughout these years. I profited enormously of the advice, comments and precious answers of Dr. Alberto Mengoni, who was always eager to hear any advance in the analysis. I'm grateful to Prof. Roberto Gallino for having always worked out immediately the consequences for the s-process models and to have explained his simulations in details. The explanations and guidance of Dr. Michael Heil and the constant assistance of Dr. Ralf Plag during the inelastic scattering measurement have been fundamental. I have also to mention the many discussions with Dr. Cesar Domingo Pardo about the resonance analysis and his willingness to advise me in any occasion. I want also to thank my friend Kaori Fujii for her work in analyzing the osmium resonances and for fruitful discussions. I must also remember how fast and careful Dr. Gaelle Aerts and Dr. Rita Terlizzi were in calculating the weighting functions for osmium. I'm also grateful to D. Roller, E. P. Knaetsch, and W. Seith for providing continuous support at the 3.7 MV Van de Graaff accelerator and the student operators who could not rest during the nights when the inelastic scattering experiment was running. I have also to thank all members of the n_TOF Collaboration to have been always so nice with me.